Measuring the W boson mass at LEP using the OPAL detector

David Eatough

THE UNIVERSITY
of MANCHESTER

Particle Physics Group
Department of Physics and Astronomy

November 22, 1998

A thesis submitted to The University of Manchester for the degree of
Doctor of Philosophy in the Faculty of Science and Engineering

Contents

List of Figures

List of Tables

Abstract

The W boson mass has been measured using the data taken by the OPAL detector in 1997 at $\sqrt{s}$=183 GeV. The convolution method, which constructs a likelihood as a function of M_{W} for each event, was used. This likelihood is formed by convoluting the W boson production spectrum with the experimental resolution function for each kinematic fit. The measured W boson mass for the $\mathrm{W^+W^-} \rightarrow \mathrm{q\bar{q}q\bar{q}}$ and the $\mathrm{W^+W^-} \rightarrow \mathrm{q\bar{q}}l\nu$ channels combined was determined to be

$$M_{\mathrm{W}} = 80.30 \pm 0.14 \pm 0.08 \text{ GeV}$$

where the first error is statistical and the second systematic.

Declaration

No portion of the work referred to in this thesis has been submitted in support of an application for another degree or qualification of this or any other university or other institute of learning.

The Author

The author was educated at Bingley Grammar School and the University of Durham, before joining the Department of Physics and Astronomy at the University of Manchester. The work presented here was undertaken at Manchester and CERN, Geneva.

Acknowledgements

I would like to thank my supervisor Fred Loebinger for his help, encouragement and advice over the last three years, and all those who have answered my questions and pointed me in the right direction. This includes, in no particular order, Tara Shears, Jo Pater, Mark Thomson, Nigel Watson, Terry Wyatt, Vakhtang Kartvelishvili, Roger Barlow and George Lafferty. The convolution method was inspired by the work of Niels Kjaer and Martin Mulders and guided by the thesis of Chris Parkes.

Thank you PPARC for the money. Thanks also to all the friends I made in Manchester and Geneva, you know who you are, who made it all worth while. A special thank you to Lucy for putting up with me, and finally thanks Mum for proof reading it.

Chapter 1

Introduction

1.1 General introduction

The Standard Model of particle physics has proved to be very successful in predicting and explaining the nature of all the known elementary particles. These can be divided into two groups: fermions and gauge bosons. Tables 2.1 and 2.2 show all these particles. The fermions are the constituents of matter (i.e. quarks make up protons and neutrons, and together with electrons they make up atoms) and the gauge bosons are the force carriers which allow the fermions to interact.

The Standard Model has two distinct parts, Electro-weak Theory and Quantum Chromodynamics (QCD), the former is the main concern of this thesis. Electro-weak theory is the unification of Quantum Electrodynamics (QED) and the theory of weak interactions. It was originally developed by Glashow [1], Weinberg [2], and Salam [3]. QED was developed by Feynman and describes the interaction of the photon with electrically charged particles, it has been experimentally tested to very high precision.

The photon, which is massless, is the gauge boson that carries the electro-magnetic force. The carriers of the weak force are the W and Z bosons, which unlike the photon

are massive. The aim of this thesis is to make a precise measurement of the W boson mass. In the Standard Model of particle physics the mass of the W and the Z bosons are very important parameters. A precise measurement of the W boson will constrain the Standard Model, and along with a measurement of the top quark mass [4], will restrict the possible mass of the Higgs boson, the only particle in the Standard Model not to have been observed.

It is because of the large mass of the W and Z bosons that weak interactions are not as obvious as electro-magnetic interactions in everyday life. Weak interaction are very important however, for instance the fusion of two protons in the sun is a weak process, and weak interactions are responsible for beta decay of radioactive elements.

1.1.1 The LEP accelerator

In order to directly measure the mass of the W boson, real W bosons must be produced. Particle accelerators are used to produce the very high energies needed to create these real W bosons. This analysis uses Ws produced at LEP , the Large Electron Positron collider, at CERN. The electrons and positrons can interact in many ways, one possible interaction is $e^+e^- \rightarrow Z^0$, this has been used to produce tens of millions of Z bosons at LEP between 1991 and 1995. These events have been used to measure the Z boson mass to great accuracy (M_Z =91.187$\pm$0.002 GeV [5]) [1]. The LEP beam energy has been steadily increased since 1996 and the production of W^+W^-pairs became possible in 1997 via the interaction $e^+e^- \rightarrow W^+W^-$.

A particle detector is needed to measure the energy and momentum of the W bosons, or more accurately, the decay products of the W bosons. There are four particle detectors on the LEP ring: ALEPH, DELPHI, L3, and OPAL. The electrons and positrons are made to collide at the centre of each of these detectors.

[1]Mass and momentum are given in units of GeV following the convention in [15]

The data analysed in this thesis was taken by OPAL in 1997 at a beam energy of 91.35±0.025 GeV [6] [7].

1.1.2 The history of W boson mass measurements

In 1981 lowest order electro-weak theory was used to predict that the mass of the W boson was 78.3±2.4 GeV [8]. In 1983 the first real W bosons were observed at CERN using the UA1 [9] and UA2 [10] detectors [2] which were on the $Sp\bar{p}S$ accelerator. These W bosons were produced by the process $\bar{\mathrm{p}} + \mathrm{p} \rightarrow \mathrm{W}^{+}\mathrm{X}^{-}$and its charge conjugate reaction, where X is some unspecified hadronic system. The UA1 and UA2 detectors measured the mass to be $M_{\mathrm{W}} = 82.7 \pm 1.0 \pm 2.7$ GeV and $M_{\mathrm{W}} = 80.2 \pm 0.6 \pm 1.4$ GeV respectively, which is in good agreement with the earlier prediction. Since then the W boson mass has been measured more accurately at D0 [11] and CDF [12] and in 1996 at LEP II [13]. The world average value for M_{W} in the summer of 1996 using direct measurements was M_{W} =80.33±0.15 GeV [14].

1.2 Thesis outline

Chapter two contains a very brief introduction to electro-weak theory, which discusses how symmetries in the Lagrangian density introduce gauge fields, and how spontaneous symmetry breaking allows these fields to become massive. W boson production and details relevant to the mass measurement are also mentioned. In chapter three there is a description of the sub-detectors, the trigger, the data acquisition, and the event reconstruction, of the OPAL detector. Jet reconstruction algorithms and

[2] The 1984 Nobel prize for physics was awarded to Carlo Rubbia, the head of UA1, and Simon Van Der Meer, who worked on the $Sp\bar{p}S$ accelerator, for their decisive contributions to the discovery of the W and Z bosons. The 1979 Nobel prize for physics was awarded to Sheldon Glashow, Abdus Salam, and Steven Weinberg for their contributions to electro-weak theory.

the basic stages in Monte Carlo event simulation and detector simulation are also discussed.

Chapter four describes the event selections for $W^+W^- \rightarrow q\bar{q}q\bar{q}$, $W^+W^- \rightarrow q\bar{q}e\nu$, $W^+W^- \rightarrow q\bar{q}\mu\nu$ and $W^+W^- \rightarrow q\bar{q}\tau\nu$ events. In chapter five a simple method of measuring the W boson mass is proposed in order to explain some of the problems and concepts involved. The kinematic fit that is used in practice and two realistic mass measurement methods are also discussed. Chapter six contains the main analysis of this thesis, the convolution method of W boson mass measurement. The concept, the implementation, and the systematic checks are described. Chapters seven and eight contain the results and conclusions respectively.

Chapter 2

Electro-weak theory and W boson production

2.1 Introduction

A general knowledge of the Standard Model of particle physics is assumed throughout this thesis. In this chapter a brief outline of electro-weak theory will be given and the topics relevant to this analysis will be discussed.

2.2 The Standard Model

The Standard Model describes the properties and interactions of all the elementary particles known at present. It has proved to be extremely useful and accurate. The Standard Model describes the electro-magnetic, weak and strong interactions. It does not describe gravity, but at the energies and scales involved in particle physics the effects of gravity are negligible. The fundamental particles of the Standard Model are either spin 1/2 fermions or integer spin bosons. Tables 2.1 and 2.2 list these particles and some of their properties. The Standard Model provides a mechanism for the

generation of masses for these particles. This mechanism involves the Higgs boson which is the only elementary particle present in the Standard Model that has not yet been experimentally observed.

fermions		fermion generations			quantum numbers			
		1	2	3	q	t	t_3	Y/2
leptons	left handed	ν_e	ν_μ	ν_τ	0	$\frac{1}{2}$	$\frac{1}{2}$	$-\frac{1}{2}$
		e	μ	τ	-1	$\frac{1}{2}$	$-\frac{1}{2}$	$-\frac{1}{2}$
	right handed	e	μ	τ	-1	0	0	-1
quarks	left handed	u	c	t	$\frac{2}{3}$	$\frac{1}{2}$	$\frac{1}{2}$	$-\frac{1}{6}$
		d	s	b	$-\frac{1}{3}$	$\frac{1}{2}$	$-\frac{1}{2}$	$-\frac{1}{6}$
	right handed	u	c	t	$\frac{2}{3}$	0	0	$\frac{2}{3}$
		d	s	b	$-\frac{1}{3}$	0	0	$-\frac{1}{3}$

Table 2.1: The Standard Model fermions and their quantum numbers. q is the electric charge, t is the weak isospin, t_3 is the third component of weak isospin and Y is the weak hypercharge ($q = Y/2 + t_3$).

The gauge group of the Standard Model is $SU(3) \otimes SU(2)_L \otimes U(1)$. The $SU(3)$ corresponds to the strong interactions and the $SU(2)_L \otimes U(1)$ corresponds to the electro-weak interactions. This analysis is primarily concerned with the electro-weak interaction.

bosons		quantum numbers				mass (GeV)
		q	t	t_3	Y/2	
vector bosons	W^+	+1	1	+1	0	80.427±0.075
	W^-	-1	1	-1	0	80.427±0.075
	Z^0	0	1	0	0	91.187±0.002
	γ	0	0	0	0	0
	g	0	0	0	0	0
scalar bosons	H	0	$\frac{1}{2}$	$-\frac{1}{2}$	$\frac{1}{2}$	77< M_H <287

Table 2.2: The Standard Model bosons and their quantum numbers. The masses and 95 % confidence level mass limits are taken from the 1998 Review of Particle Physics [15], which contains the data analysed in this thesis.

2.3 Electro-Weak theory

2.3.1 Symmetries of the Lagrangian density

In the quantum field theories like the Standard Model [1] the propagation and interaction of fields is described by their Lagrangian density and their equations of motion, the Euler-Lagrange equations.

$$\partial_\mu\left(\frac{\partial\mathcal{L}}{\partial(\partial_\mu\psi_i)}\right) = \frac{\partial\mathcal{L}}{\partial\psi_i} \tag{2.1}$$

Here ψ are the fields and $\mathcal{L}$ is the Lagrangian density. The free lepton Lagrangian density for massless leptons [2] is

$$\mathcal{L}_0 = i[\overline{\psi_l}(x)\,\partial\!\!\!/\,\psi_l(x) + \overline{\psi_{\nu_l}}(x)\,\partial\!\!\!/\,\psi_{\nu_l}(x)] \tag{2.2}$$

[1] The books [17], [16], and [18] were used extensively in this section

[2] Massive leptons will be discussed in the next section

where as normal $\not{\partial} = \gamma_\mu \partial^\mu$, ψ_l are the charged lepton fields (electron, muon, and tau), ψ_{ν_l} are the neutral lepton fields (the neutrinos), and x is the four dimensional coordinate x^μ. The left-handed and right-handed helicity states of the lepton fields interact differently and so it is sensible to separate them in the Lagrangian density.

$$\psi^L(x) = \tfrac{1}{2}(1 - \gamma_5)\psi(x) \tag{2.3}$$

$$\psi^R(x) = \tfrac{1}{2}(1 + \gamma_5)\psi(x) \tag{2.4}$$

It is convenient notation, as we shall see later, to combine the two left handed fields into a two component field.

$$\Psi_l^L(x) = \begin{pmatrix} \psi_{\nu_l}^L(x) \\ \psi_l^L(x) \end{pmatrix} \tag{2.5}$$

The free lepton Lagrangian density for massless fermions is now

$$\mathcal{L}_0 = i[\overline{\Psi_l^L}(x)\not{\partial}\Psi_l^L(x) + \overline{\psi_l^R}(x)\not{\partial}\psi_l^R(x) + \overline{\psi_{\nu_l}^R}(x)\not{\partial}\psi_{\nu_l}^R(x)] \tag{2.6}$$

A consequence of making the Lagrangian density symmetric under phase transformations is to introduce extra gauge fields and conserved currents into the theory. How this happens will be outlined. Consider the $U(1)$ local phase transformation

$$\psi(x) \rightarrow \psi'(x) = \exp[ig'f(x)Y/2]\psi(x) \tag{2.7}$$

Here ψ is any one of the four lepton fields (ψ_l^L, $\psi_{\nu_l}^L$, ψ_l^R, or $\psi_{\nu_l}^R$), g' is a real number called the coupling constant, $f(x)$ is an arbitrary real differentiable function, and Y is the weak hypercharge associated with the field. In order for the Lagrangian density to remain invariant under this transformation the ordinary derivative must be replaced by the covariant derivative:

$$\partial^\mu\psi(x) \rightarrow D^\mu\psi(x) = [\partial^\mu + ig'B^\mu(x)Y/2]\psi(x) \tag{2.8}$$

where $B^{\mu}(x)$ is a 'gauge field' which transforms like

$$B^{\mu}(x) \rightarrow B^{\mu\prime}(x) = B^{\mu}(x) - \partial^{\mu} f(x) \tag{2.9}$$

The associated conserved current is

$$J^{\mu}_{B}(x) = \overline{\psi}(x)\gamma^{\mu}\psi(x)Y/2 \tag{2.10}$$

So the B^{μ} field couples charged right handed leptons to charged right handed leptons, charged left handed leptons to charged left handed leptons, and neutral left handed leptons to neutral left handed leptons. Neutral right handed leptons would have Y/2 equal to zero and so would not interact with the B^{μ} field.

Now consider the $SU(2)$ local phase transformation

$$\psi(x) \rightarrow \psi'(x) = \exp[ig\tau_j\omega_j(x)t]\psi(x) \tag{2.11}$$

where ψ is any one of the four lepton fields, j is 1, 2 or 3, $\omega_j(x)$ are real arbitrary functions, g is the coupling constant, t is the weak isospin, and τ_j are the Pauli spin matrices.

$$\tau_1 = \begin{pmatrix} 0 & 1 \\ 1 & 0 \end{pmatrix} \quad \tau_2 = \begin{pmatrix} 0 & -i \\ i & 0 \end{pmatrix} \quad \tau_3 = \begin{pmatrix} 1 & 0 \\ 0 & -1 \end{pmatrix} \tag{2.12}$$

Since t=1/2 for the left handed fields and t=0 for the right handed fields, equation 2.11 can be rewritten as

$$\begin{gathered} \Psi^{L}_{l}(x) \rightarrow \Psi^{L\prime}_{l}(x) = \exp[ig\tau_j\omega_j(x)/2]\Psi^{L}_{l}(x) \\ \psi^{R}_{l}(x) \rightarrow \psi^{R\prime}_{l}(x) = \psi^{R}_{l}(x) \qquad \psi^{R}_{\nu_l}(x) \rightarrow \psi^{R\prime}_{\nu_l}(x) = \psi^{R}_{\nu_l}(x) \end{gathered} \tag{2.13}$$

The right handed fields transform onto themselves and so no interaction terms arise. For the Lagrangian density to remain invariant for the left handed fields the ordinary derivative must be replaced by the covariant derivative.

$$\partial^{\mu}\Psi^{L}_{l}(x) \rightarrow D^{\mu}\Psi^{L}_{l}(x) = [\partial^{\mu} + ig\tau_i W^{\mu}_{i}(x)/2]\Psi^{L}_{l}(x) \tag{2.14}$$

where the $W_j^\mu(x)$ are 'gauge fields' which transform like

$$W_i^\mu(x) \rightarrow W_i^{\mu\prime}(x) = W_i^\mu(x) - \partial^\mu\omega_i(x) - g\varepsilon_{ijk}\omega_j(x)W_k^\mu(x) \tag{2.15}$$

if $\omega_j(x)$ are small. The associated conserved currents are

$$J_i^\mu(x) = \tfrac{1}{2}\overline{\Psi_l^L}(x)\gamma^\mu\tau_i\Psi_l^L(x) \qquad i = 1,2,3 \tag{2.16}$$

The τ_i matrices mean that the W_1^μ and W_2^μ fields couple a charged lepton to a neutral lepton. The observed boson fields ($W^{\pm\mu}$) that couple charged leptons to neutral leptons are actually the linear combinations

$$W^{\pm\mu} = \frac{1}{\sqrt{2}}[W_1^\mu \mp W_2^\mu] \tag{2.17}$$

The W_3^μ field couples either two charged leptons or two neutral leptons. The observed boson fields A^μ and Z^μ are the linear combination

$$A^\mu = \sin\theta_W W_3^\mu + \cos\theta_W B^\mu \tag{2.18}$$

$$Z^\mu = \cos\theta_W W_3^\mu - \sin\theta_W B^\mu \tag{2.19}$$

where θ_W is the weak mixing angle. If the A^μ field is to be identified as the photon (i.e. to couple through the term $-e\overline{\psi}_l(x)\gamma^\mu\psi_l(x)A^\mu(x)$ in the Lagrangian density as it is known to do from QED) the coupling constants must be set to

$$g\sin\theta_W = g'\cos\theta_W = e \tag{2.20}$$

So far only the free leptons and their interactions with the gauge fields have been considered. The Lagrangian density must also contain terms which describe the gauge bosons when no leptons are present. For the B^μ field this term is

$$-\frac{1}{4}B_{\mu\nu}(x)B^{\mu\nu}(x) \tag{2.21}$$

where

$$B^{\mu\nu}(x) \equiv \partial^\nu B^\mu(x) - \partial^\mu B^\nu(x) \tag{2.22}$$

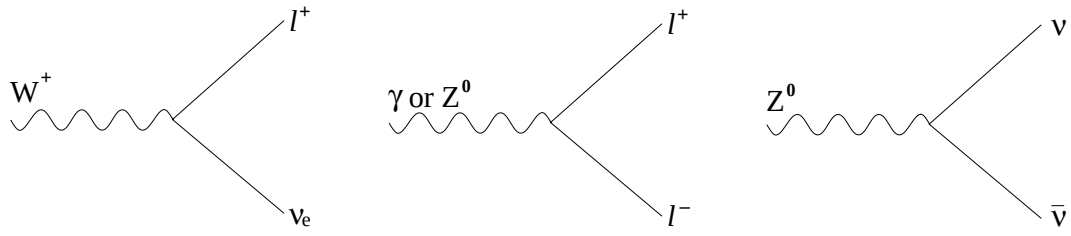

Figure 2.1: Electro-Weak gauge bosons coupling to lepton pairs.

For the W^μ fields extra interaction terms have to be introduced once more in order to keep the Lagrangian density invariant under the transformations in 2.13. These new interactions are among the gauge bosons themselves. The term describing the W^μ fields when no leptons are present is

$$-\frac{1}{4}G_{i\mu\nu}(x)G_i^{\mu\nu}(x) \tag{2.23}$$

where

$$G_i^{\mu\nu}(x) \equiv \partial^\nu W_i^\mu(x) - \partial^\mu W_i^\nu(x) + g\epsilon_{ijk}W_j^\mu(x)W_k^\nu(x) \tag{2.24}$$

Some examples of the possible interactions are shown in figure 2.2. The first of these has particular importance to this analysis as it contributes to the process $e^+e^- \rightarrow W^+W^-$.

2.3.2 Gauge boson masses

So far only massless leptons and gauge bosons have been considered. Mass terms can easily be put in the Lagrangian density, for instance the mass of the $W^\pm$ bosons could be included by

$$m_W^2 W_\mu^\dagger(x)W^\mu(x) \tag{2.25}$$

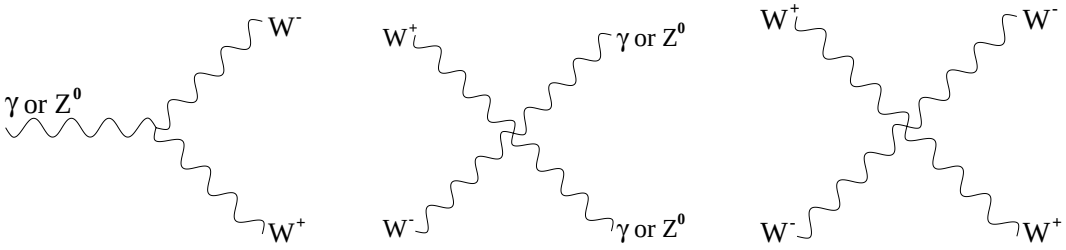

Figure 2.2: Some possible gauge boson self-interactions

Unfortunately terms like this would result in a Lagrangian density which was not invariant under the local phase transformations 2.7 and 2.13. One could use such a theory, in lowest order perturbation theory this may give reasonable results but this theory in not renormalisable and can not predict anything above first order. A better way of including the masses of the fermions and gauge bosons is needed. Spontaneous symmetry breaking is the way in which masses will be included.

Consider the ground state of a system whose Lagrangian density possesses some symmetry. If the ground state of this system is non-degenerate the corresponding energy eigenstate is unique and will be invariant under the symmetries of the Lagrangian. If the ground state is degenerate there is no unique corresponding eigenstate. These degenerate states will transform amongst themselves under the symmetries of the Lagrangian. If one of these degenerate states is arbitrarily chosen as the ground state then the ground state no longer shares the symmetries of the Lagrangian. This choosing of an arbitrary ground state is know as spontaneous symmetry breaking. The asymmetry is not due to the addition of non-invariant terms to the Lagrangian but rather to this arbitrary choice of ground state. How this spontaneous symmetry breaking introduces masses to the gauge bosons is called the Higgs mechanism.

The Higgs mechanism

A weak isospin doublet ϕ of complex scalar fields is introduced into the theory.

$$\phi(x) = \frac{1}{\sqrt{2}} \begin{pmatrix} \phi_1 + i\phi_2 \\ \phi_3 + i\phi_4 \end{pmatrix} \tag{2.26}$$

This is the minimal choice required to generate the masses of the gauge bosons. The Lagrangian density will now contain new kinematic and potential energy terms. The potential term is

$$V(\phi) = \mu^2 \mid \phi \mid^2 + \lambda^2 \mid \phi \mid^4 \tag{2.27}$$

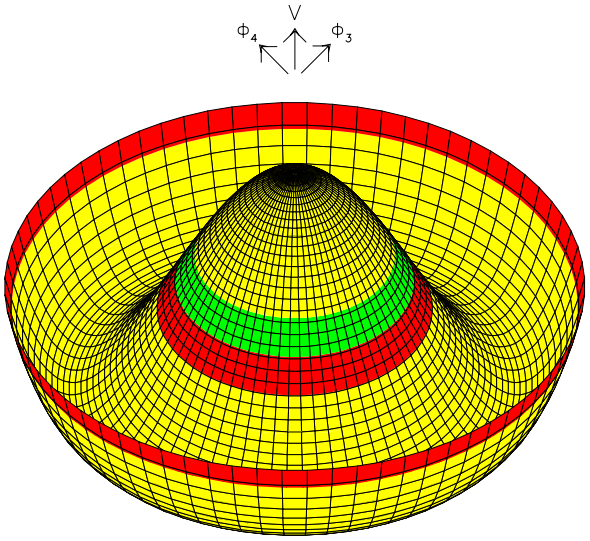

Figure 2.3: The Higgs potential in two dimensions.

Where $\lambda^2 > 0$ and $\mu^2 < 0$. The shape of this function (just considering the ϕ_3 and ϕ_4 dimensions) is shown in figure 2.3. The ground state will be the minimum of this function. The minimum is not unique, it is a 4 dimensional hyper-sphere given by

$$| \phi |^2 = \frac{-\mu^2}{2\lambda} \tag{2.28}$$

On figure 2.3 this corresponds the circle of lowest potential. If a point on this circle is arbitrarily chosen as the ground state the symmetry will be spontaneously broken. The point chosen here will be

$$\phi_1 = \phi_2 = \phi_3 = 0 \qquad \phi_4^2 = -\frac{\mu^2}{\lambda} = \nu^2 \tag{2.29}$$

When one expands $\phi(x)$ about this point it is convenient to replace the four ϕ fields with four new fields.

$$\phi(x) = \frac{1}{\sqrt{2}} \begin{pmatrix} \theta_1 + i\theta_2 \\ \nu + h + i\theta_3 \end{pmatrix} \tag{2.30}$$

There are three massless Goldstone bosons fields (θ_i) which correspond to perturbations around the minimum of the potential and one massive gauge boson field (h) that corresponds to perturbations perpendicular to this minimum. By choosing a suitable gauge (the unitary gauge) the three unphysical massless Goldstone bosons are absorbed as an extra degree of freedom by the three weak gauge bosons, the Z^0 and $W^{\pm}$, and gives them masses. Since the photon has zero weak isospin it remains massless. This leaves the massless photon, three massive weak gauge bosons, and the massive h field, called the Higgs field. The details of how this happens can be seen by considering the Lagrangian density. The masses given to the weak gauge bosons are

$$M_W = \tfrac{1}{2} g\nu \qquad M_Z = \frac{g\nu}{2\cos\theta_W} = \frac{M_W}{\cos\theta_W} \tag{2.31}$$

The vacuum expectation value ν can be expressed in terms of the Fermi coupling constant G which can be measured in muon decays, and g can be expressed in terms of the fine structure constant α which is also experimentally known. This gives

$$M_W = (\frac{\alpha\pi}{G\sqrt{2}})^{\frac{1}{2}} \frac{1}{\sin\theta_W} \qquad M_Z = (\frac{\alpha\pi}{G\sqrt{2}})^{\frac{1}{2}} \frac{2}{\sin 2\theta_W} \tag{2.32}$$

Using the value of θ_W obtained from neutrino scattering the values of $M_{\rm W}$ and $M_{\rm Z}$ were predicted in 1981 to be [8]

$$M_W = 78.3 \pm 2.4 GeV \qquad M_Z = 89.0 \pm 2.0 GeV \tag{2.33}$$

The subsequent discovery of the $W^{\pm}$ and Z^0 bosons with masses in agreement with these predictions was a great success for the unified electro-weak theory.

The mass of the Higgs is not predicted by electro-weak theory. There is a lower limit on the Higgs mass from direct searches and an upper limit from fits to electro-weak data [15], these give 77$<$ M_{higgs} $<$287 GeV at the 95 % confidence level.

The fermion masses

The leptons and quarks acquire mass by the same Higgs mechanism. Arbitrary coupling constants between the fermion and the Higgs field must be introduced. So the masses of the quarks and leptons are not predicted by the theory.

2.4 W boson production

The UA1 [9] and UA2 [10] experiments first observed W bosons in 1983. These detectors were both on the $Sp\bar{p}S$ collider at CERN. W bosons have also been observed at the D0 [11] and CDF [12] experiments which are on the TEVATRON collider. Both of these colliders are $\bar{p}p$ machines. An up-like quark in one proton will interact with a

down-like quark in an anti-proton to produce a single W by the reaction $u\bar{d} \rightarrow W^+$and its charge conjugate reaction.

At LEP II W boson pairs are produced by the reaction $e^+e^- \rightarrow W^+W^-$. The Ws then decay into either a quark and an anti-quark or to a charged lepton and a neutrino. These quarks will separate and form jets of colourless hadrons. If the charged lepton is a tau it will decay in the detector into either an electron or muon and a neutrino or it will decay to some hadrons and a neutrino.

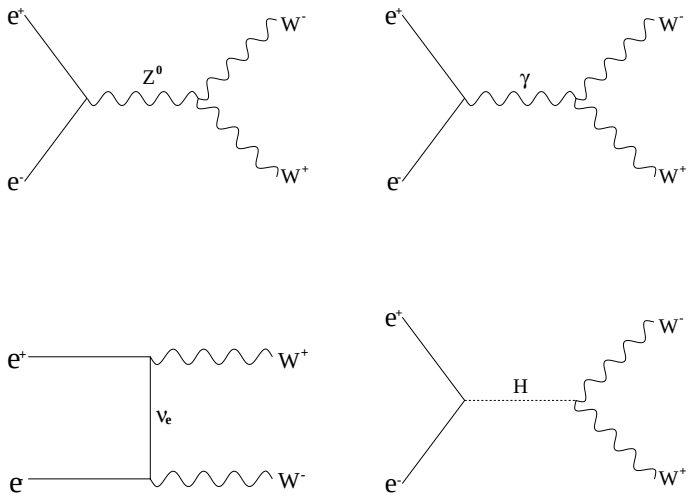

Figure 2.4: The four possible $e^+e^- \rightarrow W^+W^-$ diagrams.

The reaction $e^+e^- \rightarrow W^+W^-$can proceed by four processes. These are shown in figure 2.4. The fourth of these reactions $e^+e^- \rightarrow H^0 \rightarrow W^+W^-$has a negligible cross section at LEP II because the coupling between the Higgs and the light electrons is very small. At threshold ($\sqrt{s} \sim 161$ GeV) the dominant process is the third one, neutrino exchange. The cross section for this diagram alone continues to rise as the centre of mass energy ($\sqrt{s}$) increases. Above threshold the other two diagrams

become more important. They interfere destructively with the neutrino exchange diagram and reduce the total cross section for $e^+e^- \rightarrow W^+W^-$. Figure 2.5 shows the total cross section for $e^+e^- \rightarrow W^+W^-$.

2.5 Corrections

So far only the Born level approximation for W boson production has been considered (i.e. zeroth order Feynman diagrams with zero width Ws). This is a reasonable approximation but there are several corrections to this that need to be taken into account for a precision measurement of M_W to be made.

2.5.1 Finite width

The W boson production spectrum is a relativistic Breit Wigner with width $\Gamma_W = 2.06 \pm 0.06$ GeV [15]. The probability of a W being produced with mass m given M_W and Γ_W and ignoring phase space and other effects is

$$\rho(m \mid M_W, \Gamma_W) = \frac{\Gamma_W}{\pi M_W} \frac{m^2}{(m^2 - M_W{}^2)^2 + m^4(\Gamma_W / M_W)^2} \tag{2.34}$$

Ideally the width Γ_W should be energy dependent [19]. Putting $\sqrt{s} = m$

$$\Gamma_W(s) = \frac{s}{M_W{}^2} \Gamma_W(M_W{}^2) \tag{2.35}$$

The finite width of the W boson has a large effect on the cross section close to threshold. The abrupt turn on of the cross section at a centre of mass energy of twice the W mass is smeared out as shown in figure 2.5. Treating the width of the W properly is important for the convolution method of mass reconstruction as we shall see in chapter 6. The Monte Carlo programs used to simulate the signal treat the width accurately.

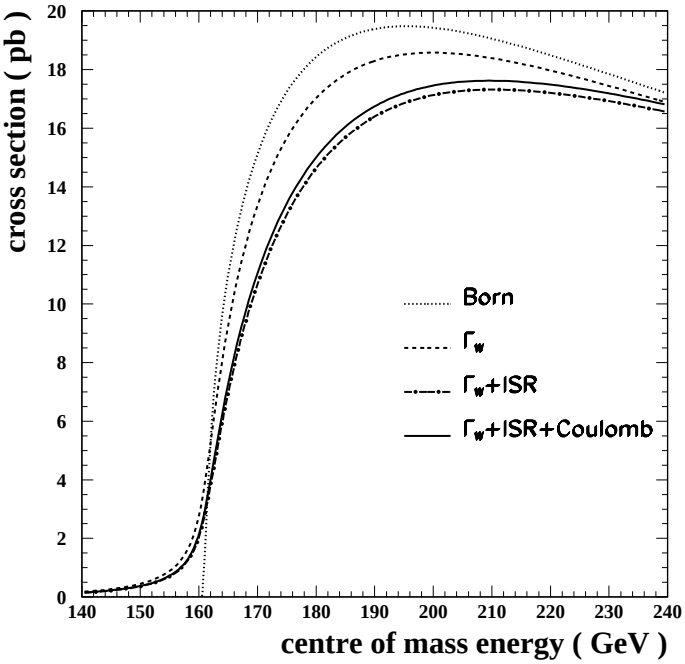

Figure 2.5: The total $e^+e^- \rightarrow W^+W^-$ cross section as a function of $\sqrt{s}$ predicted by GENTLE [20]. Various approximations are shown: the Born approximation, Born approximation with finite W width, plus ISR effects, and plus Coulomb effects.

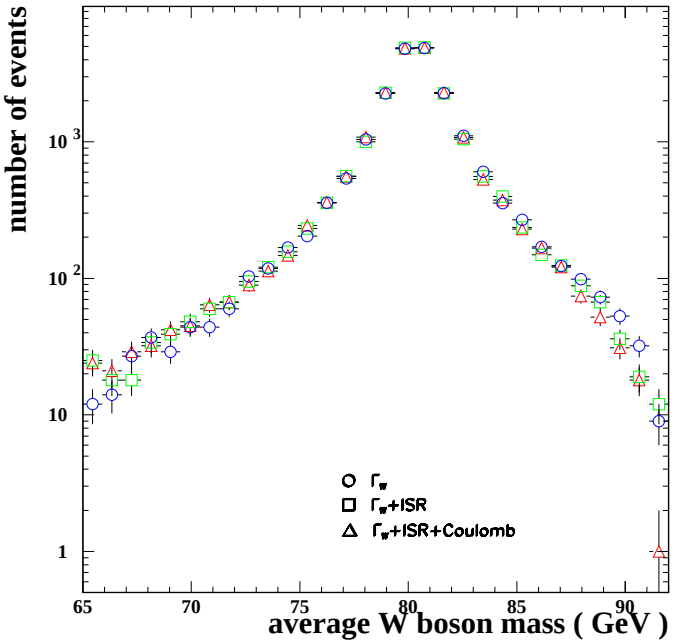

Figure 2.6: The KORALW generated average W boson mass spectrum. The circles are the KORALW prediction without any ISR or Coulomb effects (essentially just a relativistic Breit Wigner times phase space). The squares are the prediction with ISR and the triangles are the prediction with Coulomb effects and ISR.

2.5.2 Radiative corrections

Initial State Radiation

Initial State Radiation (ISR) is very important at LEP II. The electrons in the beam can emit a photon before they interact reducing the effective $\sqrt{s}$ and thus the $e^+e^- \rightarrow W^+W^-$ cross section. The average energy carried off by ISR in $e^+e^- \rightarrow W^+W^-$ events at $\sqrt{s}$=183 GeV is 1.8 GeV. The produced W boson mass spectrum is only slightly affected by ISR as shown in figure 2.6. The reconstructed mass spectrum will be affected by ISR if a kinematic fit, which forces the total energy in the event to be $\sqrt{s}$, is used. This means that the energy of the jets and leptons will be overestimated and the fitted mass will be too large. The default Monte Carlo program (MC) used is KORALW (v1.33) which tries to simulate ISR correctly up to $\mathcal{O}(\alpha^2)$.

Loop corrections

Corrections for loop diagrams like those shown in figure 2.7 need to be made. These corrections alter the Standard Model prediction for the value of M_W . These corrections are theoretically well understood to an accuracy higher than is required for this analysis [21]. The interesting loop corrections involve the top quark or the Higgs boson since these are the least well measured. These make the predicted M_W dependent on the top mass squared and the logarithm of the Higgs mass. The effect of these dependences can be seen in figure 8.2.

2.5.3 Four fermion corrections

The $q\bar{q}q\bar{q}$ and $q\bar{q}l\nu$ final states can be produced by processes that do not involve W boson pair production. These processes can interfere with the signal processes shown in figure 2.4. These interference effects can be simulated by the MC but since the

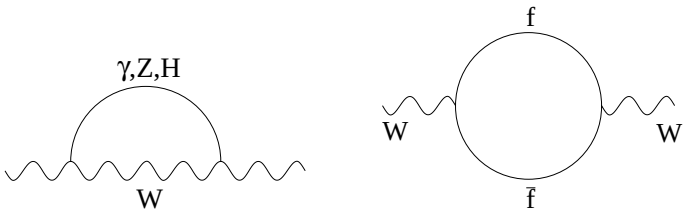

Figure 2.7: Some of the loop corrections to the W propagator. f is some fermion.

effects are small it is more convenient to use MC samples without any four fermion interference and then assess the systematic error due to this omission at a later stage.

2.5.4 Coulomb effect

The W bosons or their decay products may interact with each other. This means that the separate identity of the two Ws may be obscured.

The Coulomb effect is essentially the exchange of a photon between the two Ws before they decay [22]. This effect is most pronounced when the two Ws have little momentum (i.e. when the average W boson mass is close to the beam energy). Figure 2.6 shows the KORALW average mass spectrum with and without the Coulomb effects simulated. These affects are theoretically well understood and are modelled by KORALW (v1.33).

2.5.5 Colour reconnection

This only affects the $q\bar{q}q\bar{q}$ events. The large width of the W means that the two Ws will decay less than 0.1 fm apart. The typical hadronization distance is $\sim$1 fm. So the quarks from one W could interact with the quarks in the other W via a low

energy gluon. The effects of colour reconnection on the reconstructed M_{W} are not easy to calculate. One must rely on MC models of the non-perturbative fragmentation phase. Various different models of colour reconnection have been proposed and implemented into MC simulations [23]. The predicted shift in M_{W} for each model depends on the reconstruction method. Even for sensible reconstruction methods the different models predict different mass shifts, some as large as 100 MeV. Some of these models predict a reduction in the charged track multiplicity of each $\mathrm{q\overline{q}}$ system in $\mathrm{W^+W^-} \rightarrow \mathrm{q\overline{q}q\overline{q}}$ events compared to $\mathrm{W^+W^-} \rightarrow \mathrm{q\overline{q}}l\nu$ events. With increasing LEP II statistics these predictions can be tested and hopefully some limits placed on the allowed models .

2.5.6 Bose-Einstein correlations

In $\mathrm{q\overline{q}q\overline{q}}$ events many pions are produced. Pions are integer spin particles (bosons) and so must obey Bose statistics. This will produce an enhancement of the number of pions with small momentum differences [24]. The Bose-Einstein Correlation (BEC) radius has been measured at LEP I to be $\sim$1 fm [25]. Since the two W decay vertices will be less than 0.1 fm apart there may be BEC between pions from both Ws. The exact effect that BEC might have on the reconstructed M_{W} is not clear. Various models have been proposed and implemented in MCs. These fall into two categories: those which re-weight the events to account for BEC [27], and those which shift the momentum of pairs of identical bosons to account for BEC [26]. The shift in the reconstructed M_{W} predicted by these models varies. Most of these models predict a shift of tens of MeV in the reconstructed M_{W} .

Given high statistics the effects of BEC should be visible in the data. The momentum distribution of low momentum charged tracks should be affected. Attempts have been made to measure these effects in the data already recorded at LEP II [28]

[29] [30]. No sign of BEC between different Ws has been seen but the statistics are not yet high enough to discriminate between the various models.

Chapter 3

The OPAL detector

3.1 The LEP accelerator

The LEP (Large Electron Positron) accelerator is at CERN (the European Laboratory for Particle Physics). The LEP tunnel is 26.7km in circumference and 100m underground. It lies across the French/Swiss border between Geneva and the Jura mountains. It was designed in the late 1970s and built in the 1980s. The construction of the tunnel and the accelerator inside it was a major engineering accomplishment. LEP accelerates beams of electrons and positrons to very high energy and then collides them. The electrons are produced by thermionic emission and then some of these electrons are made to collide with a tungsten target to produce positrons. The PS and SPS storage rings accelerate these electrons and positrons to 22 GeV before injecting them into LEP.

It was planned to operate LEP in two stages. The first stage (LEP I) accelerated beams of electrons up to 45 GeV so that $e^+e^- \rightarrow Z^0$ events could be produced. LEP operated at this beam energy from 1989 to 1995. During the second stage (LEP II) the beam energy was increased to above 80 GeV so that $e^+e^- \rightarrow W^+W^-$ events could be produced. In 1996 LEP was run at two centre of mass energies, $\sqrt{s}$=161 GeV and

$\sqrt{s}$=172 GeV. In 1997 LEP was run at $\sqrt{s}$=183 GeV. It is hoped that LEP II will continue to run until 2000 and may reach a centre of mass energy close to $\sqrt{s}$=200 GeV. The data recorded in 1997 by the OPAL detector will be analyzed in this thesis. The OPAL detector is similar in overall design to the other three detectors on the LEP ring.

3.2 The OPAL detector

The OPAL (Omni-Purpose Apparatus at LEP) detector is a general purpose detector designed to reconstruct all types of events produced by the e^+e^- collisions. It is made up of many subdetectors which can be broadly grouped as: central tracking detectors, calorimeters, muon detectors and luminosity detectors. Figure 3.2 shows a cut away diagram of the OPAL detector. The OPAL detector is approximately 10 m in diameter and 12 m in length. A detailed description can be found in [32] and [31]. The coordinate system used in OPAL is as follows. The origin is at the nominal interaction region. The z axis is along the electron beam direction. The x axis is horizontal and directed towards the centre of the LEP ring. The y axis is pointing upwards. Polar angles (r, θ, ϕ) are also used where appropriate. The two coordinate systems have the usual relations $r = \sqrt{x^2 + y^2 + z^2}$, $\theta = \cos^{-1}(z/r)$, and $\phi = \tan^{-1}(y/x) \pm \pi$.

3.2.1 Central tracking system

The central tracking system consists of 4 main parts. In order of increasing radius these are the silicon microvertex detector, the vertex detector, the jet chamber, and the Z-chambers. These are all enclosed within a pressure vessel which maintains a 4 bar gas pressure. Surrounding the pressure vessel is the solenoid which provides a uniform magnetic field of 0.435 T. The purpose of the Central Tracking System

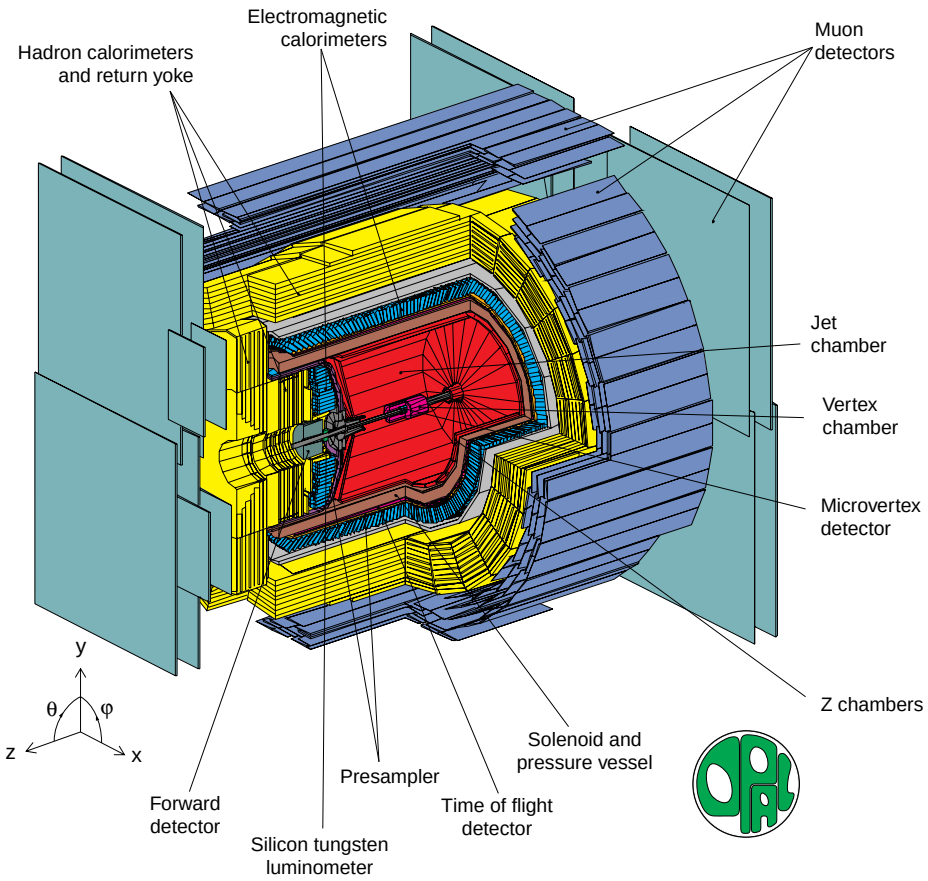

Figure 3.1: A cut away diagram of the OPAL detector

is to reconstruct the tracks of charged particles over almost the entire solid angle. The vertex detectors measure the production point of the particles and the jet and Z-chambers measure the direction and curvature and hence the momentum of the tracks.

Silicon microvertex detector

Particle detectors made from silicon are essentially reverse biased pn diodes used as solid state ionization chambers. When a charged particle passes through the diode it ionizes the silicon and forms electron-hole pairs which are swept to the electrodes by the applied electric field. This small current is used to detected the passage of a charged particle. The pn diodes can be arranged into closely spaced strips and so the position of the particle can be accurately measured.

The silicon microvertex detector [33] is the closest subdetector to the interaction point. It consists of two barrels of silicon microstrip detectors at radii of 6 cm and 7.5 cm. The inner layer has 12 ladders running parallel to the beam axis and the outer layer has 15 ladders. Each ladder is made up of 5 pairs of silicon wafers 6 cm long and 3 cm wide. Each pair of wafers consists of one single-sided wafer with read out strips running parallel to the beam axis every 50 μm and one single-sided wafer with read out strips perpendicular to the beam axis every 100 μm.

Vertex detector

The essential parts of a drift chamber are a vessel containing a mixture of gas (argon, methane and isobutane in this case) and anode wires that are held at a high voltage. The gas is ionized by a charged particle passing through it. Ionized electrons are accelerated towards the wire by the high potential. Close to the wire the electric field is strong enough to accelerate the electrons fast enough so that they ionize other gas atoms and cause an avalanche effect. This current is detected at either end of the

wire.

The vertex detector is a high precision cylindrical drift chamber. It is 1 m long with a inner radius 8.8 cm and an outer radius of 23.5 cm. It is divided into two layers each with 36 sectors. The inner (axial) sectors have 12 sense wires parallel to the beam axis and the outer stereo sectors have 6 wires inclined at 4° to beam axis. The drift time of gas ions to the axial wires allows the $r - \phi$ position of tracks to be calculated with a resolution of 55 μm. The time difference between the signals at either end of the wire gives a rough z estimate that is used in the trigger. The combination of axial and stereo drift times allows an accurate measurement ($\sigma_z \approx 700\mu$m) of the z coordinate to be made offline.

During data taking in 1997 a stereo wire broke and shorted out several stereo sectors. Luckily information about the z position of tracks is available from the silicon microvertex detector. The resolution of the central tracker has not been badly affected by this failure.

Jet chamber

The jet chamber is a large cylindrical drift chamber of length 4 m with an inner radius of 25 cm and outer radius of 185 cm. It is divided into 24 sectors. Each sector contains 159 signal wires strung parallel to the beam axis with all wire planes radial. The coordinates (r, ϕ, z) are measured for each hit using the wire position, the drift time and a charge division technique. The sum of the charge at each end of the wire is used to calculate the energy loss (dE/dx). The average $r - \phi$ resolution is 135 μm, the average z resolution is 6 cm and the momentum resolution σ_p/p^2 is better than 2×10^{-3} GeV^{-1}

Z-chambers

The Z-chambers form a set of 24 planar drift chambers each 4 m long which are mounted around the jet chamber. Each chamber is 50cm wide and 59 mm thick and consists of eight 50 cm $\times$ 50 cm cells. Each cell has 6 signal wires strung perpendicular to the beam axis. They are designed to make a precise measurement of the z coordinate of tracks as they leave the jet chamber and so improve the polar angle measurement, the momentum and hence the invariant mass resolution. The z coordinate resolution is approximately 300 μm and the $r-\phi$ resolution is approximately 1.5 cm.

3.2.2 Calorimeters

The calorimeters are split into two regions, the barrel and the end caps. The two most important subdetectors in each region are the electromagnetic calorimeter (ECAL) and the hadron calorimeter (HCAL). The presence of approximately two radiation lengths of material in front of the ECAL (mostly due to the pressure vessel and the coil) means that most electromagnetic showers start before reaching it. So presamplers are installed in front of the ECAL to improve the spatial and energy resolution. Time of flight detectors are also installed in front of the ECAL.

Time of flight counters

The barrel time of flight detector consists of 160 scintillation counters at a radius of 236 cm surrounding the coil and covering a polar angle of $|\ cos\theta\ | < 0.82$. It provides fast trigger information, allows charged particle identification in the range 0.6 to 2.5 GeV and an effective rejection of cosmic rays. In 1996 the Tile Endcap system [34] was added. It is designed to enhance the trigger information in the forward region and identify which electron bunch the e^+e^-collision was from. It is installed between

the endcap presamplers and the endcap ECAL.

Electromagnetic presampler

The barrel presampler is a double layer of limited streamer drift tubes. The anode wires run parallel to the beam axis and there are 1 cm wide cathode strips on both sides of each layer angled at 45° to the anode wire. The z position is reconstructed from these strips and from measurement of the charge at each end of the anode wire. The hit multiplicity gives an estimate of the energy deposited in the material in front of the presampler. Each endcap presampler is an umbrella shaped arrangement of 32 multiwire chambers covering the angle $0.83 < |\, cos\theta \,| < 0.95$.

Electromagnetic calorimeter

The dominant energy loss of a high energy electron in matter is due to bremsstrahlung. For high energy photons the dominant absorption process is electron pair production. So high energy electrons or photons entering the lead glass of the electromagnetic calorimeter will start a shower of other electrons and photons, which will in turn produce more electrons and photons. This showering will stop when the energy of these daughter electrons is below some critical value E_c where the energy losses due to ionization are greater than that due to bremsstrahlung. The value of E_c is about 600 MeV. The total number of electrons in a shower is proportional to the energy of the incident particle. The Cerenkov radiation from these electrons is collected by a photo-multiplier tube at the base of each block. The amount of this Cerenkov radiation gives an accurate estimate of the energy of the incident electron or photon.

The barrel ECAL consists of a cylindrical array of 9440 lead glass blocks. Each block is 10cm $\times$ 10cm in area and 37 cm deep (24.6 radiation lengths). They are angled to point approximately at the interaction region. Each endcap ECAL consists of a dome shaped array of 1132 lead glass blocks similar to those in the barrel. These

blocks are aligned with the beam axis and follow the contours of the pressure bell. They come in three depths: 38, 42 and 52 cm. Due to the high magnetic field in the endcap region vacuum photo triodes are used instead of photo-multiplier tubes.

Hadron calorimeter

Hadronic showers are similar to electromagnetic showers except that hadrons have a longer interaction length than electrons or photons. This means that hadron calorimeters must be much thicker than electromagnetic calorimeters. Another difference between electromagnetic and hadronic showers is that hadronic shower development is more complex as there are many more processes that can occur. This means that the estimate of the initial hadron energy is less accurate than the estimate of the electron or photon energy. In OPAL the iron magnet return yoke is used as part of the HCAL. Showering occurs in the iron and the number of particles produced is measured by limited streamer tubes.

The barrel HCAL contains 9 layers of chambers sandwiched between 8 layers of 10 cm thick magnetic return yoke iron. The endcap HCAL consists of 8 layers of chambers sandwiched between 7 plates of iron. The chambers are limited streamer tubes with anode wires 1 cm apart. The chamber signals result from charge induced on the pads and strips on the outer and inner surfaces. The layers of pads are grouped together to form towers in 48 bins of ϕ and 21 bins in θ.

Complementing the barrel and endcap regions are the pole-tip detectors which extend the HCAL coverage from $\mid cos\theta \mid = 0.91$ to 0.99. In this region the gaps between the iron plates in the return yoke are reduced to 10 mm so 7 mm thick multiwire proportional chambers are used. There are 10 detector layers with the anode wires 2 mm apart. Again the signal is read off from pads and strips on the surfaces of the chambers.

3.2.3 Muon detector

The muon detectors are positioned outside the magnetic return yoke and so particles that reach them have traversed on average the equivalent of 1.3 m of iron. This reduces the probability of a pion not interacting to less than 0.001.

The muon barrel detector consists of 110 drift chambers covering $\mid cos\theta \mid < 0.68$ for 4 layers and $\mid cos\theta \mid < 0.72$ for at least one layer. The chambers are 1.2 m wide and 90 mm deep. There are three different lengths (10.4 m, 8.4 m and 6.0 m) to accommodate the magnet support legs and cabling. Each chamber is split into two cells containing an anode wire which runs the length of the cell parallel to the beam axis. There are diamond shaped pads opposite the anode wire from which the z position can be calculated to an accuracy of 2 mm. The $r-\phi$ coordinate is calculated from the drift time and has an accuracy of 1.5 mm.

The muon endcaps consist of two layers of limited streamer tube chambers. All the tubes are perpendicular to the beam axis, one layer has its wires vertical and the other horizontal. Each chamber has two planes of 8 mm wide aluminium strips, one parallel to the tubes and the other perpendicular. The position of the streamer can be found on the strips parallel to the tubes with an accuracy of 3 mm and on the strips perpendicular to the tubes with an accuracy of 1 mm.

3.2.4 Luminosity detectors

The luminosity is calculated from the number of Bhabba events recorded as the cross section for this process is well known. Bhabba events are $e^+e^- \rightarrow e^+e^-$ events. The scattering angle of the electrons is generally small and so the luminosity detectors are close to the beam pipe. There are two subdetectors used to measure the Bhabba events, the forward detector and the silicon tungsten detector.

The forward detector consists of 4 parts: calorimeter, tube chambers, gamma

catcher and far-forward monitor. It covers the angle 47 mrad $< \theta <$ 120 mrad. The calorimeter consists of 35 layers of lead-scintillator sandwich divided into a presampler and main calorimeter giving a total of 24 radiation lengths. The tube chambers are positioned between the presampler and the main calorimeter and give the position of the shower accurately. The gamma catcher is a ring of lead-scintillator sandwich which fills the hole in θ between the edge of the ECAL endcap and the start of the forward detector main calorimeter. The far forward monitors are small lead-scintillator calorimeter modules mounted either side of the beam pipe 7.85 m from the interaction point.

The silicon tungsten detectors are $\pm$ 234 cm from the interaction point and cover the angle 25 mrad $< \theta <$ 59 mrad. Each calorimeter consists of 19 layers of silicon and 18 layers of tungsten giving a total of 22 radiation lengths of material. Each silicon layer consists of 16 wedges in ϕ with each wedge subdivided into 64 pads.

3.2.5 Trigger and pretrigger

The bunches of electrons and positrons in the beam cross 45 thousand times a second. Most of these crossings produce no interactions. It would be impractical to store the data from each subdetector for every bunch crossing. The trigger and pretrigger decide when an interesting event has happened and when the data from the subdetectors should be read out and stored. The conditions used to decide can be of two types, 'stand alone' signals such as large track multiplicity or large energy sums, or from groups of lower threshold signals from separate subdetectors binned in θ and ϕ. This analysis is concerned with $W^+W^- \rightarrow q\bar{q}q\bar{q}$ and $W^+W^- \rightarrow q\bar{q}l\nu$ events, all of which should have a large number of tracks and large energy deposits in the calorimeters.

3.2.6 Data acquisition

If an event is selected by the trigger each subdetector's data is read out and assembled by the event builder. The events are then passed to the filter which removes any obviously bad events. The remaining events are then passed to a piece of software called ROPE (Reconstruction of OPAL Events) [35]. This takes the data from each individual subdetector and reconstructs the charged tracks and calorimeter clusters. The output from ROPE is stored as Data Summary Tables (DSTs). When better estimates are available for the calibration of each subdetector the events can be reROPEd to obtain a more accurate description of the tracks and clusters. Most analyses use the DSTs to get information about each track and cluster in an event. ROPE tries to assign calorimeter clusters to charged tracks and any unassociated clusters are identified as coming from neutral particles. The events can be viewed graphically using a piece of software called GROPE (Graphical Reconstruction of OPAL Events) [36]. This runs on the DSTs produced by ROPE. Figure 3.2 shows an event selected as a $W^+W^- \rightarrow q\overline{q}q\overline{q}$ candidate.

3.3 Jet reconstruction

The decay $W \rightarrow q\overline{q}$ is of importance to this analysis. The two quarks produced by the decay of the W will each have a momentum of roughly 40 GeV in roughly opposite directions. Quarks are never directly observed. Because of the non-abelian nature of QCD the force between a pair of oppositely coloured quarks grows as the distance between them grows. At some point as the distance between quarks increases there is enough energy to create a new quark pair. These new quarks will separate and in turn produce more quark pairs. Eventually the momentum difference between pairs and groups of quarks will be small enough for them to bind and form mesons and baryons. These hadrons will all be traveling in roughly the same direction as the

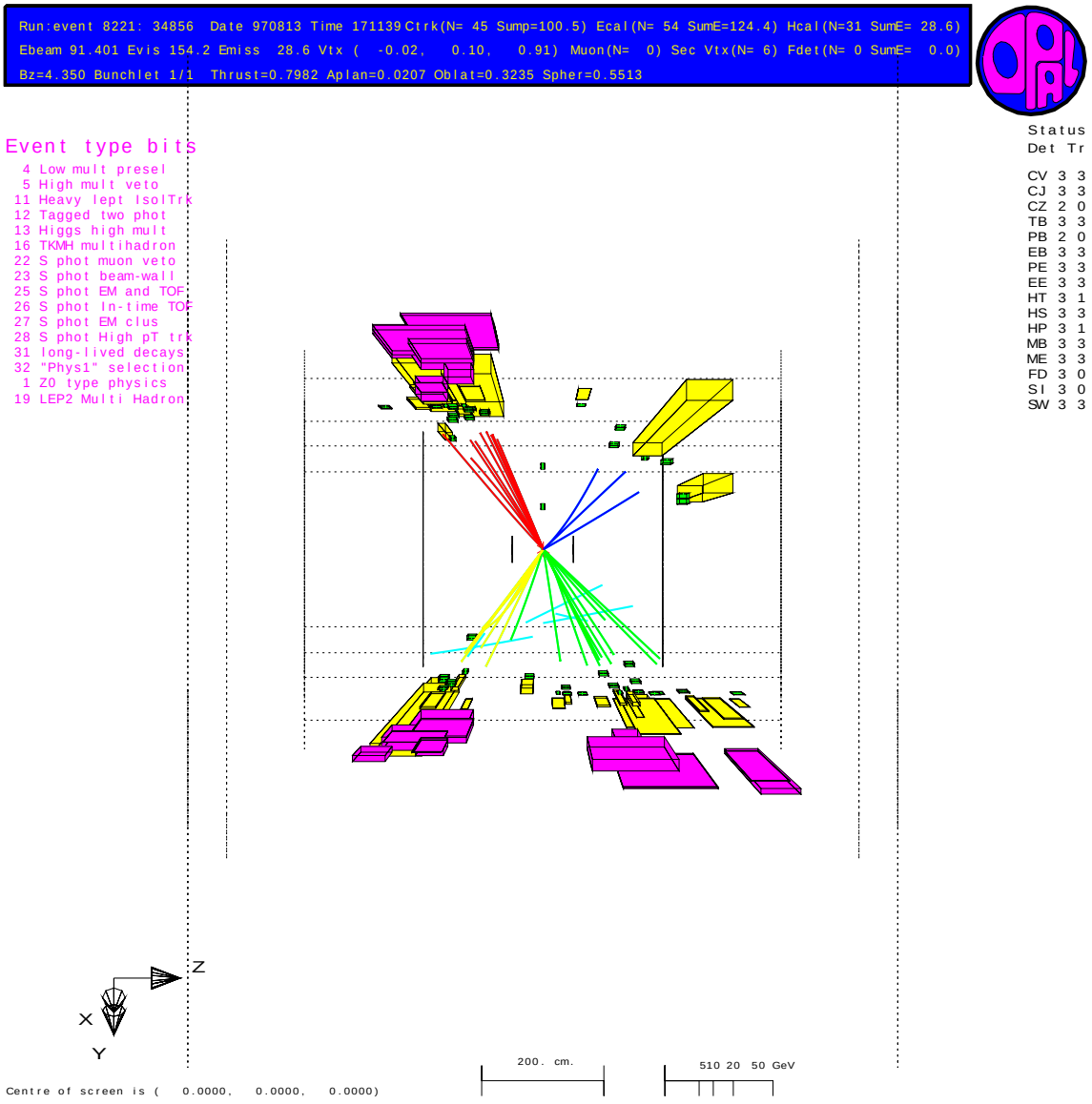

Figure 3.2: This a graphical representation of an event recorded by OPAL using GROPE [36]. For this event the relative likelihood value from the $W^+W^- \rightarrow q\bar{q}q\bar{q}$ selection was 0.98. The four jets have been coloured individually. The size of the yellow (light grey) boxes represent the amount of energy in each ECAL cluster. The size of the magenta (dark grey) boxes represent the energy in the HCAL clusters.

parent quark but will share different fractions of its momentum.

So, although the quarks from the W decay are not observed directly, a 'jet' of hadrons is seen in the detector. If the momentum and energy of all the hadrons in the jet can be measured the momentum of the initial quark can be estimated. In the $W^+W^- \rightarrow q\bar{q}q\bar{q}$ events there are four primary quarks and so four jets of hadrons. Assigning all the reconstructed tracks and clusters to the right primary quark is no trivial task.

There are several algorithms that try to group tracks into jets. The one that is used in this analysis is the Durham algorithm [37]. This works by initially assigning each particle as a jet by itself. The quantity y_{ij} is then calculated for each pair of jets.

$$y_{ij} = \frac{2min(E_i^2, E_j^2)(1 - cos\theta_{ij})}{E_{vis}^2} \tag{3.1}$$

E_{vis} is the visible energy in the event (i.e. the sum of the measured particle energies), E_i is the energy of jet i, and θ_{ij} is the angle between the jets i and j. The pair of jets with the smallest y_{ij} are combined into a single jet (i.e. the energy and momentum from each jet are both added together). There are two ways of continuing: to not specify the number of jets, and to specify the number of jets. In the first way the process of combining the jets with the lowest y_{ij} is repeated until all jet pairs have y_{ij} above a certain value y_{cut}. This may result in there being any number of jets. The second way is to require a certain number of jets and repeat the process of combining the jets with the lowest y_{ij} values until the required number of jets is achieved. The second way is used in this analysis. In the $W^+W^- \rightarrow q\bar{q}q\bar{q}$ selection the required number of jets is four. A measure of how 'four jet-like' the event is can be achieved by looking at y_{34}. The value of y_{34} is the lowest value of y_{ij} for all the pairs of combinations of the four jets. This is the value of y_{cut} where the event would have changed from a three jet event to a four jet had the first way of jet find been used. In

the $W^+W^- \rightarrow q\overline{q}l\nu$ selection the lepton candidate is removed from the process and two jets are required.

3.4 Event simulation

Accurately simulated events are very important for this analysis. The term Monte Carlo (MC) is used in this thesis to mean event simulation. There are two basic stages in the event simulation: the event generation, and the detector simulation.

3.4.1 Event generation

The four vectors of the particles in the event are generated in this stage. This is in itself a multistage process. Firstly the e^+e^-collision and the production of the primary partons is simulated. In an $e^+e^- \rightarrow W^+W^-$event the electrons, the initial state radiation (ISR), the W bosons, and W decay partons are all generated at this stage. The next stage is the parton shower where the quarks may radiate hard gluons. Then there is the hadronization stage. The W decay quarks separate and hadronize into jets. This is a non-perturbative process and a phenomenological model must be used. Generally the hadrons produced by the hadronization will be unstable and in the final stage they decay into stable hadrons. Experimentally measured branching ratios are used for these decays.

There are various MC programs used in this analysis. The $e^+e^- \rightarrow W^+W^-$ events are generated by KORALW [38]. KORALW uses JETSET [39] to do the hadronization and decay of unstable hadrons. The $Z^0/\gamma \rightarrow q\overline{q}$ events are generated by PYTHIA [40] which again uses JETSET to do the hadronization. KORALW was designed specifically to generate $e^+e^- \rightarrow W^+W^-$events at LEP II. It treats ISR to $\mathcal{O}(\alpha^2)$. It allows multiple ISR photons with finite transverse momentum. The decay of the heavy polarized taus and Final State Radiation (FSR) is also well modelled.

JETSET is widely used for LEP simulations. It has been tuned to match the LEP I data and reproduces the data accurately. JETSET uses the Lund string fragmentation model [41]. Other MC programs are used for the four fermion backgrounds or for systematic checks. These include grc4f [42], EXCALIBUR [43], and HERWIG [44].

These MC programs are not perfect. They have all been tuned to match the large amounts of data recorded at LEP I. Care was taken to compare the MC predictions with the data whenever possible.

3.4.2 Detector simulation

The four vectors of all the particles in an event are passed from the event generator to the detector simulation program. The OPAL detector is modelled using the GOPAL program [45] which uses the GEANT package [46]. The passage of the particles through the detector is modelled, this includes ionization, scattering, decay, and other interactions. The data that each subdetector would have produced is then simulated. This 'simulated data' is then processed in exactly the same way as the real data. It is ROPEd and DSTs with extra MC cheat information are formed. These DSTs are then analysised in exactly the same way as the real data DSTs.

This detector simulation can be very computer intensive. A faster 'smear' mode of the simulation is available. This uses a simplified detector geometry and less precise models for the track interactions. This fast 'smear' mode of the detector simulation is used in the evaluation of some of the systematic errors.

Chapter 4

The event selection

Before a measurement of the W boson mass can be made the W^+W^- events have to be separated from the other types of events that can occur. This separation can be achieved by insisting that the events have properties passing certain criteria or cuts, this is called a simple cut based selection. In general a more effective separation can be achieved if the information from several properties or variables are combined in some multivariable discrimination scheme. Possible multivariate selections include relative likelihood selections, Fisher discriminate selections and artificial neural network selections. All these selection techniques rely heavily on accurate MC samples to estimate the efficiency for selecting the signal and background and to assess any possible bias introduced to the measured M_{W} .

In this analysis the standard procedure is to use a simple cut based preselection to remove those events which are obviously not signal but still maintain a very high efficiency for the signal events, and then to use a relative likelihood selection to improve the signal/background separation.

4.1 $W^+W^- \rightarrow q\bar{q}q\bar{q}$ event selection

The cross sections for the signal and important background processes are shown in table 4.1. Processes that do not contain quarks in the final state can be effectively rejected by insisting that the events contain 5 or more charged tracks and 7 or more ECAL clusters. The standard OPAL LEP I multi-hadron selection, called the Tokyo multi-hadron event selection (TKMH), is used to do this [31].

For the rest of the $W^+W^- \rightarrow q\bar{q}q\bar{q}$ analysis the general OPAL WW working group track and cluster quality cuts are used, these are shown in appendix B. These cuts should remove any badly measured tracks or clusters.

source	cross section (*pb*)	preselection efficiency %
$W^+W^- \rightarrow q\bar{q}q\bar{q}$	7.2	89.4 $\pm$ 0.1
$W^+W^- \rightarrow q\bar{q}l\nu$	6.9	5.1 $\pm$ 0.1
$Z^0/\gamma \rightarrow q\bar{q}$	107	2.32 $\pm$ 0.02
$ZZ \rightarrow q\bar{q}q\bar{q}$	0.26	70.2 $\pm$ 1.0
$ZZ \rightarrow q\bar{q}l\bar{l}$	0.28	16.9 $\pm$ 0.9

Table 4.1: The estimated cross section for the important processes. The efficiencies are calculated from the MCs listed in table 4.2. Only the statistical errors on the efficiency are shown.

Of all the background events passing the TKMH selection the $e^+e^- \rightarrow Z^0/\gamma \rightarrow q\bar{q}$ events are the most important due to their large cross section. The $Z^0/\gamma \rightarrow q\bar{q}$ process has a cross section approximately 15 times higher than the $W^+W^- \rightarrow q\bar{q}q\bar{q}$ process at $\sqrt{s}$ = 183 GeV. Both processes only have hadronic jets in the final state and so can be difficult to separate, particularly if the Z is produced well off its mass shell and there is significant hard gluon radiation (i.e. there is little Initial State Radiation

(ISR) and the event has multiple jets). The $W^+W^- \rightarrow q\overline{q}q\overline{q}$ selection procedure is primarily designed to remove $Z^0/\gamma \rightarrow q\overline{q}$ events.

The $ZZ \rightarrow q\overline{q}q\overline{q}$ background is difficult to separate from the signal but luckily the cross section at 183 GeV is small. Since the Z mass is 10 GeV larger than the W mass, and the resolution on the W mass per event is better than 10 GeV, the ZZ events should not cause a problem for the mass measurement.

The selection consists of two parts [1]: a cut based preselection to separate those events which are obviously not signal, and a relative likelihood selection using the PTC technique for those events passing the preselection [52]. The output of this relative likelihood can be interpreted as an estimate of the probability that each event is a signal event rather than a background event, this probability is used in the mass reconstruction.

4.1.1 Preselection

The tracks and clusters are grouped into 4 jets using the Durham reconstruction algorithm [37], as discussed in section 3.3. A cut is put on the minimum track multiplicity of the jets, each jet must have at least one track ($N_{min} \geq 1$).

In a large fraction of the $Z^0/\gamma \rightarrow q\overline{q}$ events a high energy photon is radiated by the electron or positron so that the Z may be produced on mass shell. This Initial State Radiation (ISR) photon is predominantly produced with momentum close to the e^+e^-direction. The detector cannot extend all the way down to e^+e^-beam and so the ISR photon is often not detected. This means that the visible energy of

[1]The $W^+W^- \rightarrow q\overline{q}q\overline{q}$ selection used in this analysis is very similar to the selection used by the OPAL collaboration at $\sqrt{s}$=172 GeV [48]. The author was heavily involved in the development and implementation of this selection [49]. The improved $\sqrt{s}$=183 GeV selection was actually finalised by E. Torrence and D. Karlen and uses a technique called Projection-Transformation-Correlation (PTC) proposed by D. Karlen and described in [52]

source	Monte Carlo sample	generated $\sqrt{s}$	generated M_{W}
$\mathrm{W^+W^-} \rightarrow$ all	KORALW run 7323	183 GeV	80.33 GeV
$\mathrm{W^+W^-} \rightarrow$ all	KORALW run 7324	182 GeV	80.33 GeV
$\mathrm{W^+W^-} \rightarrow$ all	KORALW run 7325	184 GeV	80.33 GeV
$\mathrm{W^+W^-} \rightarrow$ all	KORALW run 7326	183 GeV	79.33 GeV
$\mathrm{W^+W^-} \rightarrow$ all	KORALW run 7327	183 GeV	79.83 GeV
$\mathrm{W^+W^-} \rightarrow$ all	KORALW run 7328	183 GeV	80.83 GeV
$\mathrm{W^+W^-} \rightarrow$ all	KORALW run 7329	183 GeV	81.33 GeV
$\mathrm{Z^0}/\gamma \rightarrow \mathrm{q\overline{q}}$	PYTHIA run 5050	183 GeV	n/a
$\mathrm{ZZ} \rightarrow$ all	PYTHIA run 7338	183 GeV	n/a
Four Fermion	grc4f runs 6850, 6851, 5795	183 GeV	80.33 GeV

Table 4.2: The default Monte Carlo samples used.

$Z^0/\gamma \rightarrow q\overline{q}$ events is often less than the centre of mass energy ($\sqrt{s}$). The visible energy in the signal events should be close to $\sqrt{s}$, so a cut is placed on the ratio of the visible energy over $\sqrt{s}$ ($R_{vis} > 0.7$).

If the ISR photon in radiative $Z^0/\gamma \rightarrow q\overline{q}$ events is produced at a large enough angle from the beam it will be seen in the end cap ECAL. In the signal events there should be no high energy photon or lepton, so a cut is put on the ratio of the highest energy ECAL cluster in an event over $\sqrt{s}$ ($R_{max} < 0.3$).

The effective centre of mass energy $\sqrt{s'}$ is calculated by a kinematic fit which imposes energy and momentum conservation. The kinematic fit looks for possible ISR photons and then reconstructs the jets using a fixed y_{cut} of 0.02, this allows the number of jets to vary. One unseen ISR photon is allowed in the fit. If the kinematic fit fails, the $\sqrt{s'}$ is calculated from the acollinearity. The signal events should have $\sqrt{s'}$ close to $\sqrt{s}$. A large fraction of the $Z^0/\gamma \rightarrow q\overline{q}$ events will have $\sqrt{s'}$ close to the Z mass (91 GeV). A cut is put on the ratio of $\sqrt{s'}$ over $\sqrt{s}$ ($R_{sprime} > 0.75$).

The matrix element for the process $Z^0 \rightarrow q\overline{q}gg$, where there are two hard gluons radiated, is calculated and the probability that the four measured jet momenta were produced by this process is found. A cut is placed on this QCD matrix element probability which is labelled QCD_{420} ($\log(QCD_{420}) < 0$) [50].

A combination of jet energies and angles called $jang$ is used where

$$jang = \frac{E_4}{\sqrt{s}}(1 - cos\theta_{12}cos\theta_{13}cos\theta_{23}) \tag{4.1}$$

Here the jets are ordered in energy, with 1 being the highest energy jet. E_4 is the energy of the lowest energy jet, θ_{12} is the angle between the two highest energy jets and so on. In $Z^0/\gamma \rightarrow q\overline{q}$ events the lowest energy jet is likely to have a lower energy than the lowest energy jet in a $W^+W^- \rightarrow q\overline{q}q\overline{q}$ event. Also, in $Z^0/\gamma \rightarrow q\overline{q}$ events the jets are more likely to be collinear so the product of the cosines of these angles will be closer to 1 than for $W^+W^- \rightarrow q\overline{q}q\overline{q}$ events. A cut is placed at $jang > 0.05$. These

variables are shown in figure 4.1 for the signal and background MC and for the data. The cuts are shown in figure 4.1 and summarised in table 4.3

After preselection the estimated efficiency for selecting $W^+W^- \rightarrow q\bar{q}q\bar{q}$ events is 89 % and for $Z^0/\gamma \rightarrow q\bar{q}$ events it is 2.3 %. The purity after preselection including all sources of background is estimated to be 68 %. These percentages are calculated using the MC samples listed in 4.2.

Cut value
$R_{sprime} > 0.75$
$R_{max} < 0.3$
$jang > 0.05$
$R_{vis} > 0.7$
$\log(QCD_{420}) < 0.0$
$N_{min} \geq 1$

Table 4.3: The $W^+W^- \rightarrow q\bar{q}q\bar{q}$ preselection cut values.

4.1.2 Relative likelihood selection

All the events which pass the preselection are used in this analysis. To further improve the signal/background separation a relative likelihood selection is used to find an estimate of the probability that each event is a signal event. The next section contains a brief discussion of how a relative likelihood selection works.

How a relative likelihood selection works

Consider a variable x that has some discriminating power (i.e. the variable has a different distribution for the signal and the background). Probability density

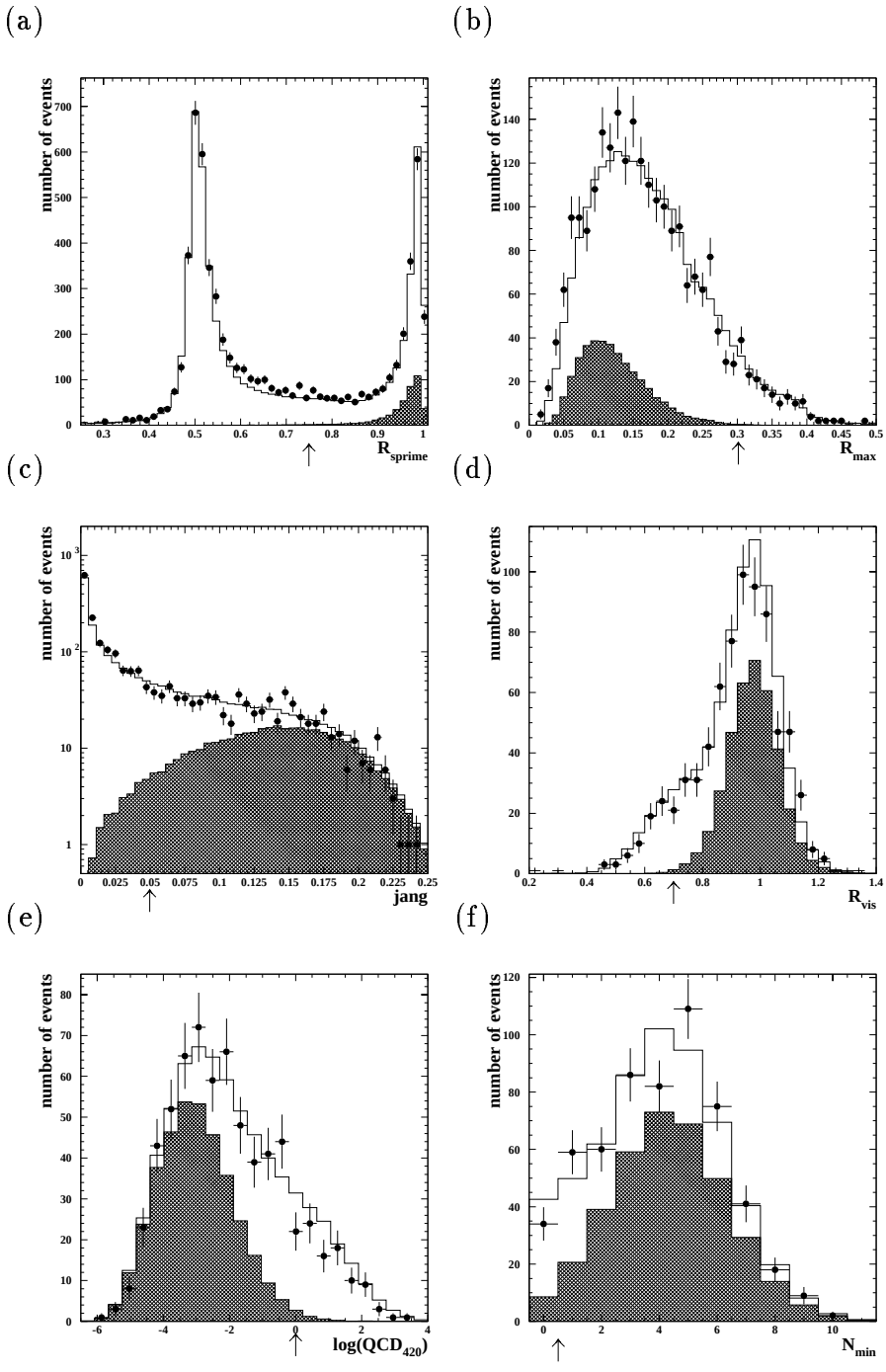

Figure 4.1: The $W^+W^- \to q\bar{q}q\bar{q}$ preselection variables. The arrow marks the value of each cut. In the R_{sprime} plot all those events passing the TKMH selection are shown. Each cut is applied successively, so the N_{min} plot has all the other cuts applied. The points are the 183 GeV data. The hatched histogram is the $W^+W^- \to q\bar{q}q\bar{q}$ signal, the open histogram is the sum of the signal and backgrounds from $Z^0/\gamma \to q\bar{q}$, $W^+W^- \to q\bar{q}l\nu$ and $ZZ \to$ all.

functions (pdfs) or reference histograms can be formed for the signal and background from MC samples. Then for each data event an estimate of the probability $P_s(x)$ that it is signal can be constructed from this variable.

$$P_s(x) = \frac{p_s(x)}{p_s(x) + p_b(x)}$$

where $p_s(x)$ and $p_b(x)$ are the values of the signal and background pdfs respectively.

A better estimate can be constructed if more than one variable is used. If these variables are called x_i then the improved probability or relative likelihood value is

$$L(x_i) = \frac{n_s \prod P_s(x_i)}{n_s \prod P_s(x_i) + n_b \prod P_b(x_i)}$$

where $P_b(x_i)$ is the probability that the event is background and is formed in a similar way to $P_s(x_i)$, n_s and n_b are the relative normalisations of the signal and background due to their cross sections and preselection efficiencies.

If the variables x_i were not correlated in any way then this would be the best estimate of the probability that the event is signal. Normally this is not the case and there are some correlations. In order to get a better estimate this selection uses the PTC method described in [52] and [53]. This involves transforming the variables in such a way that they are all Gaussian with zero mean and unit width. The covariance matrix of these transformed variables is then used in the calculation of P_s and P_b and information contained in the correlations used. Care was taken to ensure that the variables used are correlated in a simple way and that the MC simulated the correlations well.

The variables used in the relative likelihood

There are four variables chosen for the relative likelihood selection. The value of y_{cut} (the jet resolution parameter) where the number of jets changes from 4 to 5 is used ($log(y_{45})$). The sphericity, defined as $1.5(E_1 + E_2)$ where E_1 and E_2 are the first two

eigenvalues of the momentum tensor, is used. The QCD matrix element probability $\log(QCD_{420})$ is used here as well as in the preselection. The modulus of the cosine of the modified Nachtmann-Reiter angle is used [51]. This is the angle between the vector formed by the sum of the two highest energy jets and the vector formed by the sum of the two lowest energy jets.

Figure 4.2 shows these four variables for the signal and background MC and for the data. Figure 4.3 shows the value of this relative likelihood, this is used as the probabilty that the event is a signal event in the W mass measurement.

Relative Likelihood variables
$\log(y_{45})$
sphericity
$\log(QCD_{420})$
$\mid cos\theta_{NR} \mid$

Table 4.4: The $W^+W^- \rightarrow q\bar{q}q\bar{q}$ relative likelihood variables.

4.2 The $W^+W^- \rightarrow q\bar{q}l\nu$ event selection

The $Z^0/\gamma \rightarrow q\bar{q}$ background is not such a problem in this channel as there is a high energy lepton with which to distinguish the signal events. Again a relative likelihood selection is used on those events passing a simple cut based preselection. A high purity and efficiency can be achieved by placing a cut on the final relative likelihood value rather than using the PTC technique and using the likelihood as a probability.

The $W^+W^- \rightarrow q\bar{q}l\nu$ selection is in fact three selections, one for $q\bar{q}e\nu$, one for $q\bar{q}\mu\nu$ and one for $q\bar{q}\tau\nu$ events. The electron and muon selections are very similar

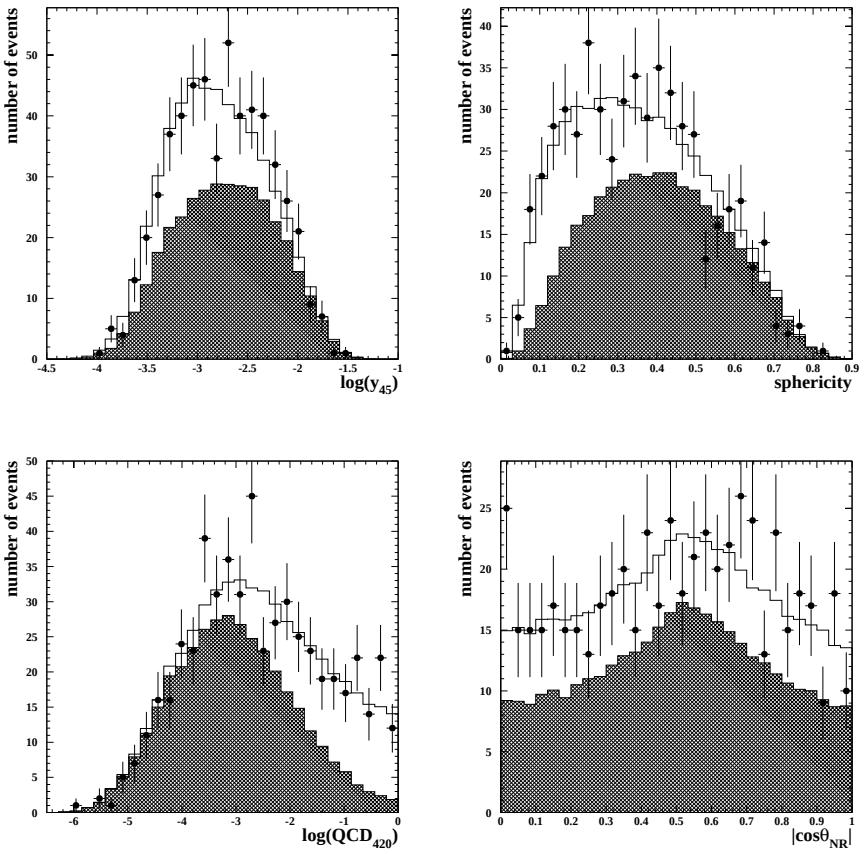

Figure 4.2: The $W^+W^- \to q\bar{q}q\bar{q}$ relative likelihood variables. The points are the 183 GeV data. The hatched histogram is the $W^+W^- \to q\bar{q}q\bar{q}$ signal, the open histogram is the sum of the signal and backgrounds from $Z^0/\gamma \to q\bar{q}$, $W^+W^- \to q\bar{q}l\nu$ and $ZZ \to$ all . In this relative likelihood the correlation between the variables is used to aid the separation.

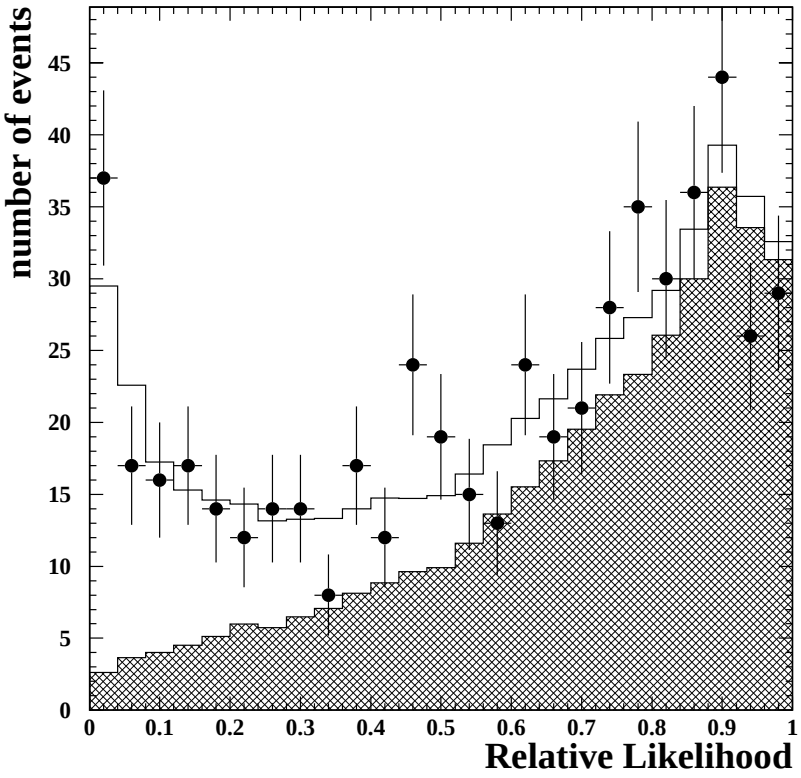

Figure 4.3: The $W^+W^- \to q\bar{q}q\bar{q}$ relative likelihood value. The points are the 183 GeV data. The hatched histogram is the $W^+W^- \to q\bar{q}q\bar{q}$ signal, the open histogram is the sum of the signal and backgrounds from $Z^0/\gamma \to q\bar{q}$, $W^+W^- \to q\bar{q}l\nu$ and $ZZ \to$ all.

and will be discussed first. [2]

4.2.1 The $W^+W^- \rightarrow q\bar{q}e\nu$ and $W^+W^- \rightarrow q\bar{q}\mu\nu$ selections

These selections are divided into four stages; charged lepton identification, preselection, relative likelihood selection, and reclassification.

Charged lepton identification

To maintain high efficiency no explicit lepton identification is required. Instead each track in an event is assigned a probability of being the charged lepton from the W decay. There are two parts to estimating this probability; finding which tracks are leptons, and deciding whether these leptons are directly from a W decay. The variables used for lepton identification are: the energy loss in the central tracking chamber (dE/dx), the energy deposited in the ECAL, the number of hits in the hadron calorimeter, and the number of hits in the muon chambers. The lepton energy and isolation are used to decide if it is from a W decay. A relative likelihood is used to combine the information from all these variables. In each event the track with the highest likelihood value is used as the candidate charged lepton.

Preselection

The preselections are designed to remove most of the $Z^0/\gamma \rightarrow q\bar{q}$ background. Both the $q\bar{q}e\nu$ and $q\bar{q}\mu\nu$ selections share most of the same cuts. Events are required to have 7 or more ECAL clusters and 5 or more charged tracks. The energy of the charged lepton (E_{lept}) must be greater than 10 GeV. A cut is placed on the ratio of the visible energy over the centre of mass energy ($0.3 < R_{vis} < 1.2$). The total energy in the forward luminosity monitors must be less than 40 GeV. The cosine

[2] The $W^+W^- \rightarrow q\bar{q}l\nu$ selections were designed and implemented by Mark Thomson.

of the angle between the charged lepton and the missing momentum ($\cos\theta_{lpmiss}$) must be smaller than 0.9. The energy of the highest isolated photon candidate must be lower than (E_{ISR} - 10) GeV, where E_{ISR} is the expected energy of an initial state photon for radiative $Z^0/\gamma \rightarrow q\bar{q}$ events ($E_{ISR} \approx 69$ GeV at $\sqrt{s} = 183$ GeV). An isolated photon candidate is an isolated ECAL cluster which does not have an associated charged track. Here isolated means that it has less than 2.5 GeV in a 200 mrad cone around it.

In the electron channel there are additional cuts on the cosine of the missing momentum, the estimated $\sqrt{s'}$, the probability from the $\sqrt{s'}$ kinematic fit, and loose cuts on the lepton probabilities. The $\sqrt{s'}$ for the $q\bar{q}l\nu$ selection is calculated in a similar way as for the $q\bar{q}q\bar{q}$ selection. The kinematic fit looks for possible ISR candidates and allows successively zero, one, or two ISR photons travelling undetected down the beam pipe to be included. If all the jets in the event are very forward or the kinematic fit fails, just the jet angles are used to calculate $\sqrt{s'}$. There are also cuts designed to reduce the number of electrons from photon conversions and ISR photons mis-identified as W decay electrons.

Some of the $q\bar{q}e\nu$ preselection variables are shown in figure 4.4. The $q\bar{q}\mu\nu$ preselection variables are very similar. The preselection is over 90 % efficient for $W^+W^- \rightarrow q\bar{q}e\nu$ and $W^+W^- \rightarrow q\bar{q}\mu\nu$ events and less than 10 % efficient for $Z^0/\gamma \rightarrow q\bar{q}$ events.

Relative likelihood selection

The relative likelihood selections are performed in the same way as for the $W^+W^- \rightarrow q\bar{q}q\bar{q}$ channel except that the correlations between variables are ignored and the PTC technique is not used. The variables used in the $q\bar{q}e\nu$ selection are: the energy of the electron candidate (E_{lept}), the energy in a 200 mrad cone around the electron candidate (E_{200}), the probability from the electron identification stage

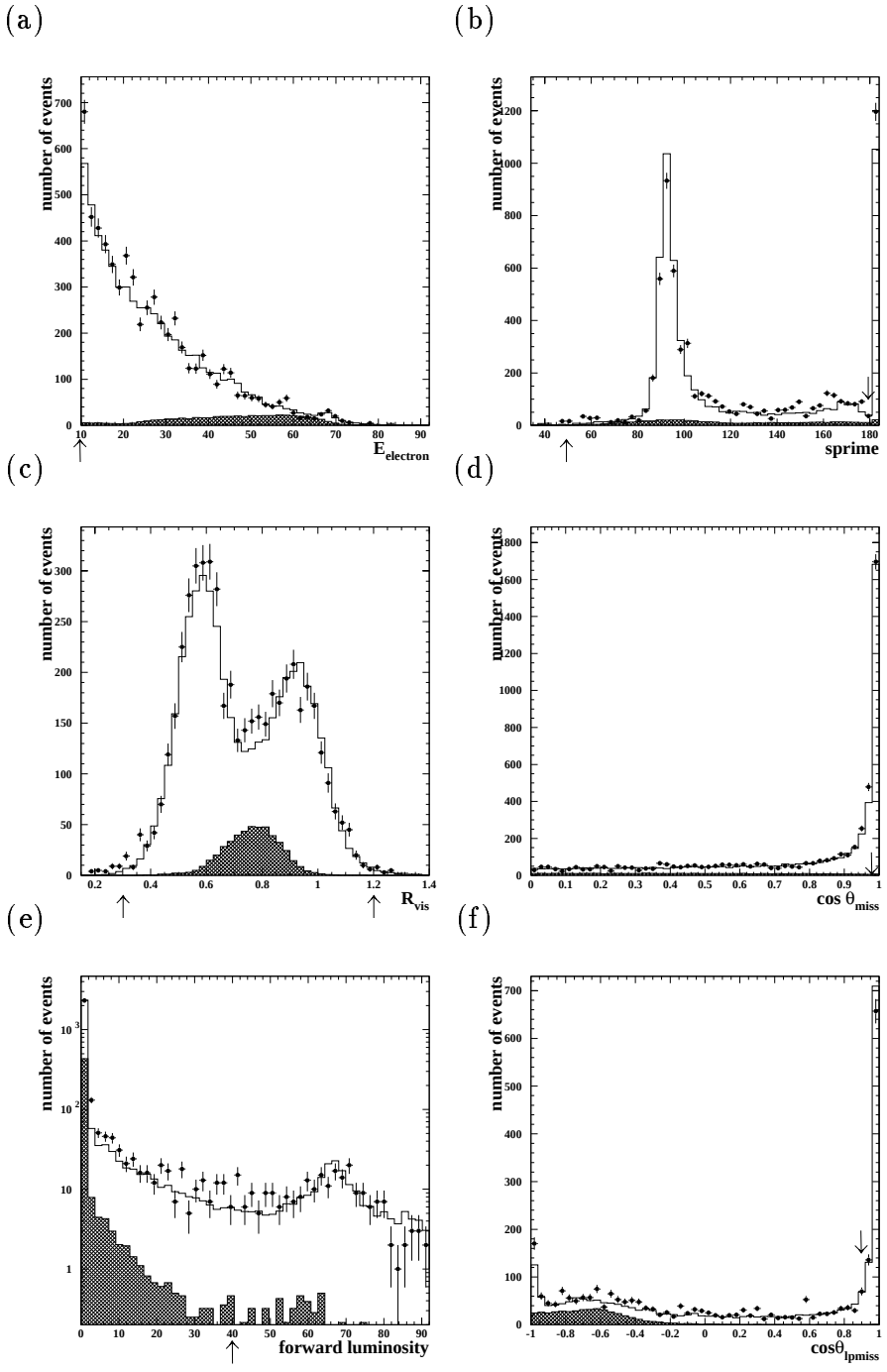

Figure 4.4: Some of the $W^+W^- \rightarrow q\bar{q}e\nu$ preselection variables. The arrow marks the value of each cut. The cuts are applied successively. The points are the 183 GeV data. The hatched histogram is the $W^+W^- \rightarrow q\bar{q}e\nu$ signal (this is shown 4 times larger than it should be to make it easier to see), the open histogram is the sum of the signal and backgrounds from $Z^0/\gamma \rightarrow q\bar{q}$ and four fermion processes.

($P(e)$), the y_{cut} value where the event changes from 2 to 3 jets (y_{23}), the ratio of the visible energy over the centre of mass energy (R_{vis}), the modulus of the cosine of the polar angle of the missing momentum ($|cos\theta_{mis}|$), the sum of the transverse momentum ($\sum p_T$), the cosine of the angle between the electron and the missing momentum ($cos\theta_{lpmis}$), the probability from the fit to estimate the effective centre of mass energy ($P(s')$), and the angle between the electron and the nearest jet (θ_{jet}).

The $q\bar{q}\mu\nu$ selection uses the same variables corresponding to the muon candidate except that θ_{jet} is found not to be helpful and is left out. Figure 4.5 shows some of the likelihood variables used in the $W^+W^- \rightarrow q\bar{q}e\nu$ and $W^+W^- \rightarrow q\bar{q}\mu\nu$ selection. Figure 4.6 shows the value of the relative likelihood. Events with likelihood values above 0.5 are selected as $W^+W^- \rightarrow q\bar{q}l\nu$ candidates.

Event reclassification

The preselections and relative likelihood selections described so far are approximately 90 % efficient for $W^+W^- \rightarrow q\bar{q}e\nu$ and $W^+W^- \rightarrow q\bar{q}\mu\nu$ events and reject approximately 99.95 % of $Z^0/\gamma \rightarrow q\bar{q}$ events. However these selections also select about 25 % of the $W^+W^- \rightarrow q\bar{q}\tau\nu$ events. Two more relative likelihood selections are performed on events which pass the $W^+W^- \rightarrow q\bar{q}e\nu$ and $W^+W^- \rightarrow q\bar{q}\mu\nu$ selections to try to separate the misidentified $W^+W^- \rightarrow q\bar{q}\tau\nu$ events. These use the same variables in the likelihood as above, but the background pdfs are now made from the $q\bar{q}e\nu$ and $q\bar{q}\mu\nu$ events. One likelihood tries to identify those events where the tau decays to an electron or muon and the other tries to identify events where the tau decays to hadrons. If either relative likelihood has a value greater than 0.5 the event is re-categorised as a $W^+W^- \rightarrow q\bar{q}\tau\nu$ event. Table 4.5 has the final efficiencies from each selection.

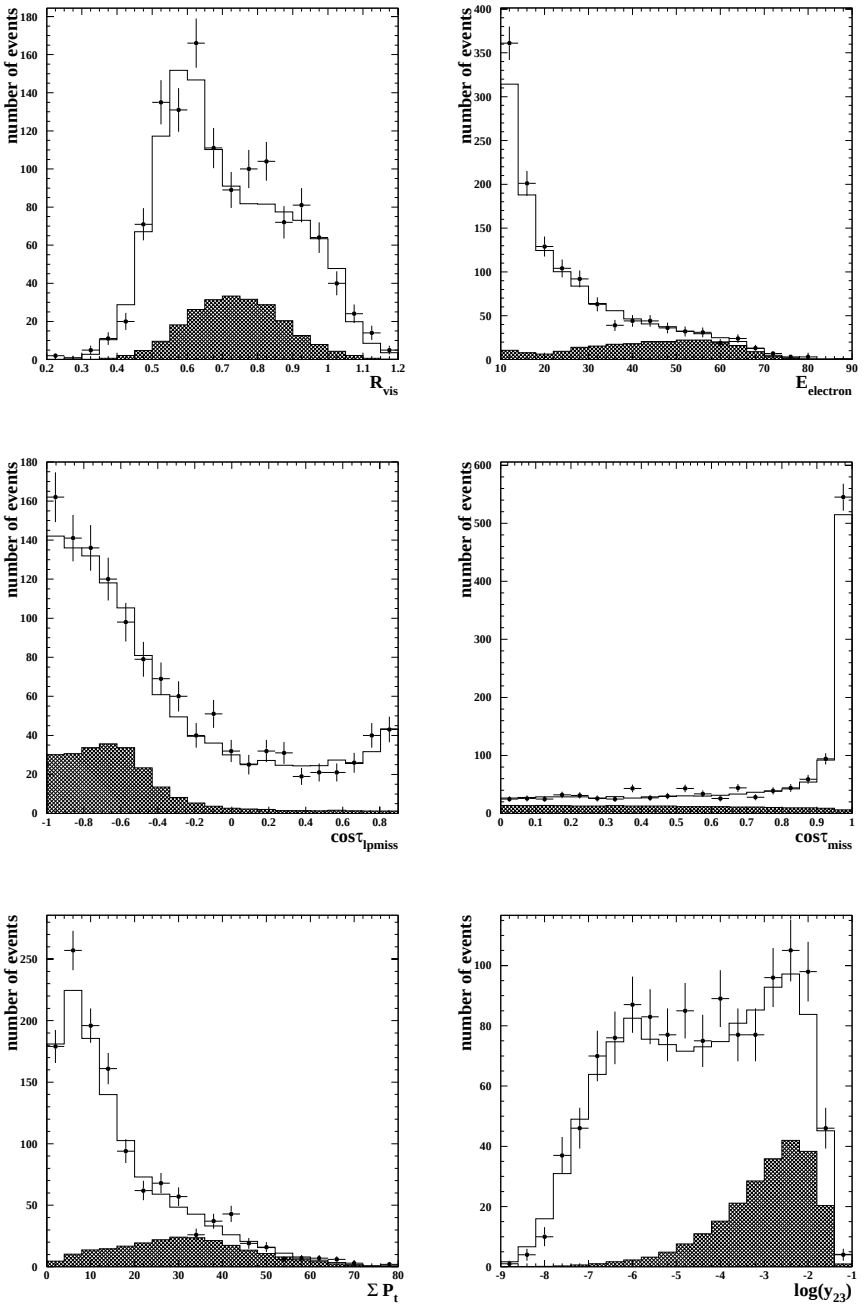

Figure 4.5: Some of the $W^+W^- \to q\bar{q}e\nu$ and $W^+W^- \to q\bar{q}\mu\nu$ relative likelihood variables for those events passing the $W^+W^- \to q\bar{q}e\nu$ or $W^+W^- \to q\bar{q}\mu\nu$ preselections. The points are the 183 GeV data. The hatched histogram is the $W^+W^- \to q\bar{q}e\nu$ or $W^+W^- \to q\bar{q}\mu\nu$ signal, the open histogram is the signal plus the $Z^0/\gamma \to q\bar{q}$ background and the background four fermion processes including the other W^+W^-events.

source	selection efficiency (%)			
	$W^+W^- \to q\bar{q}q\bar{q}$	$W^+W^- \to q\bar{q}e\nu$	$W^+W^- \to q\bar{q}\mu\nu$	$W^+W^- \to q\bar{q}\tau\nu$
$W^+W^- \to q\bar{q}q\bar{q}$	80.4±0.1	0.08±0.01	1.6±0.2	6.3±1.4
$W^+W^- \to q\bar{q}e\nu$	3.6±0.2	85.4±0.3	0.08±0.02	4.2±0.2
$W^+W^- \to q\bar{q}\mu\nu$	6.1±0.2	0.13±0.01	87.5±0.3	4.4±0.2
$W^+W^- \to q\bar{q}\tau\nu$	5.9±0.2	5.8±0.2	4.6±0.2	66.0±0.4
$W^+W^- \to l\nu\ l\nu$	0	0.03±0.02	0.01±0.01	0.03±0.02
$Z^0/\gamma \to q\bar{q}$	2.32±0.02	0.050±0.003	0.019±0.002	0.147±0.005
$ZZ \to$ all	38.0±0.9	1.6±0.2	1.8±0.2	5.6±0.3

Table 4.5: The efficiency of the four selections for various types of event. The efficiencies are for the $W^+W^- \to q\bar{q}q\bar{q}$ preselection only.

4.2.2 The $W^+W^- \to q\bar{q}\tau\nu$ selection

Events may be selected as $W^+W^- \to q\bar{q}\tau\nu$ events in two ways: by passing the $W^+W^- \to q\bar{q}e\nu$ or $W^+W^- \to q\bar{q}\mu\nu$ selections and then being reclassified as discussed in section 4.2.1, or by passing the separate $W^+W^- \to q\bar{q}\tau\nu$ selection. Events which fail the $W^+W^- \to q\bar{q}e\nu$ and $W^+W^- \to q\bar{q}\mu\nu$ selections are considered for the $W^+W^- \to q\bar{q}\tau\nu$ selection. This selection is similar to that used for the electron and muon channels but there are several differences. The lepton identification stage is replaced by a stage which tries to identify the track or tracks from the tau decay, and there is no final reclassification stage. The whole selection is divided up in to four parts corresponding to the four major decay classes for the tau: electron, muon, one prong hadronic, and three prong hadronic. So there are four preselections and four relative likelihood selections. The variables used are similar to those used in the $q\bar{q}e\nu$ and $q\bar{q}\mu\nu$ selections but include more information about the track or tracks

identified as the tau decay products.

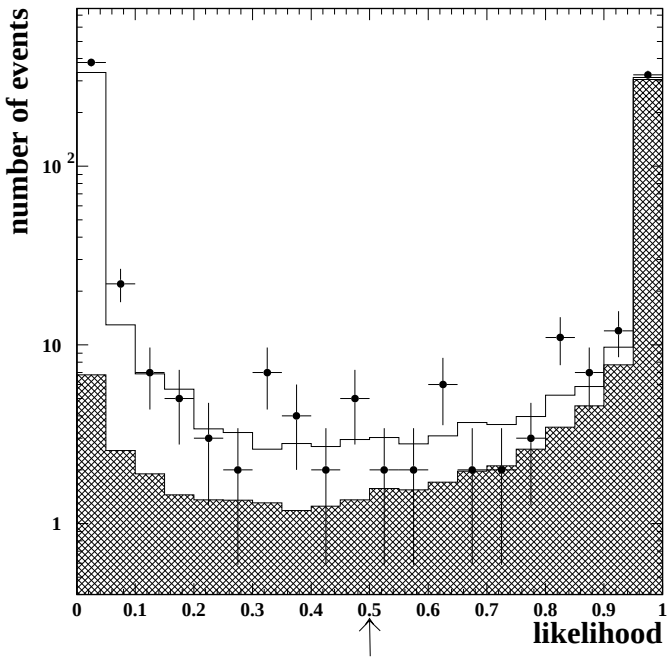

Figure 4.6: The $W^+W^- \rightarrow q\bar{q}l\nu$ relative likelihood for those events passing the $W^+W^- \rightarrow q\bar{q}e\nu$, $W^+W^- \rightarrow q\bar{q}\mu\nu$ or $W^+W^- \rightarrow q\bar{q}\tau\nu$ preselections. The points are the 183 GeV data. The hatched histogram is the $W^+W^- \rightarrow q\bar{q}l\nu$ signal, the open histogram is the sum of the signal and backgrounds from $Z^0/\gamma \rightarrow q\bar{q}$ and four fermion processes.

Chapter 5

Measuring the W boson mass

Once a sample of events has been selected some method must be devised to extract an estimate of the W boson mass from those events. There are various ways that this can be done. In order to discuss some of the ideas and problems involved a simple method will be discussed first. A more optimal solution to these problems will then be tackled in the next chapter. The $W^+W^- \rightarrow q\bar{q}q\bar{q}$ channel will be analysed with this simple method as this channel has some unique problems.

The kinematic fit used to improve the mass resolution and some practical methods of measuring the W boson mass will be discussed in sections 5.2 and 5.3.

5.1 A simple measurement of M_{W}

As part of the $W^+W^- \rightarrow q\bar{q}q\bar{q}$ event selection each event is forced into four jets by the Durham [37] jet reconstruction algorithm, as discussed in section 3.3. The measured 4-momentum of each jet is an estimate of the initial quark 4-momentum. If it was known which pair of jets came from the decay of each W boson then the invariant mass of each pair of jets would give an estimate of the W boson mass. There is no easy and accurate way of telling which jets should be combined however.

5.1.1 Jet combinations

There are three possible ways to combine the four jets into two pairs of jets, this gives three pairs of possible W boson masses. These three combinations can be labelled according to the jet energies. The highest energy jet (or quark) is labelled 1 and the lowest 4. The combination which pairs jets 1 and 2 together and jets 3 and 4 together is labelled the 1234 jet combination. The other two possibilities are labelled the 1324 and 1423 jet combinations.

If the effects of the finite width of the W bosons and ISR are assumed to be negligible the two Ws should be produced back to back and with equal momentum. This means that the highest and lowest energy quark should have been produced by the decay of one W and the two intermediate energy quarks should have been produced by the other W. However under these assumptions at threshold the difference in energy between quarks will be zero since the W bosons will be produced at rest and all the quarks should have half the beam energy. This analysis is concerned with data above threshold but the difference in energy between the quarks may still be small. The W boson width and ISR will effect the energy ordering of the quarks.

If the quark energies from the MC [1] at $\sqrt{s} = 183$ GeV are used the 1423 quark combination is the correct one 63 % of the time, the 1324 quark combination is the correct one 36 % of the time, and the 1234 quark combination is the correct one only 1 % of the time. The imperfect detector resolution and the imperfect jet reconstruction will smear out this energy ordering in the jets. When the measured jet energies are used the 1423 jet combination is the correct combination 41 % of the time, the 1324 jet combination is the correct one 36 % of the time, and the 1234 jet combination is the correct combination 23 % of the time.

Which combination of jets is the correct one is decided by a routine called WW-

[1] The fully GOPALised KORALW MC run 7323 is used as the default signal MC.

COMB [47]. This uses the MC cheat information to see how much of each jet's momentum came from each W boson. As some tracks will have been mis-assigned, jets may contain momentum from both Ws. So there is not one 'totally' correct jet combination, only the 'most' correct jet combination.

5.1.2 Invariant mass of the jet pairs

In this simple method the two W boson masses for each jet combination are calculated from the invariant mass of each jet pair's measured 4-momenta. The two masses per combination are anti-correlated. Tracks mis-assigned from one jet pair to the other jet pair will raise one mass and lower the other. For this reason the average of the two masses for each combination is used. The three average mass spectra produced are shown in figure 5.1.

The resolution on the mass can be improved by imposing energy conservation in a simple manner. Ignoring ISR the total visible energy in a $W^+W^- \rightarrow q\overline{q}q\overline{q}$ event should be equal to the $\sqrt{s}$. This could be used to scale the measured energy of all the jets and so counter-act the loss of any undetected particles and help calibrate the calorimeters. In practice it is easier to multiply the measured average mass by the ratio of $\sqrt{s}$ over the visible energy. The three scaled mass spectra are also shown in figure 5.1. One can see that the 1423 combination has the most information and that the 1234 combination has the least information. The masses from the 1234 combination where this is the wrong jet combination tend to peak around 80 GeV, unfortunately close to where the correct mass peak should be. Because $Z^0/\gamma \rightarrow q\overline{q}$ background also peaks under the signal in the 1234 jet combination mass spectrum it is difficult to reliably extract the W boson mass. So only the 1423 and 1324 jet combinations are used in this simple method.

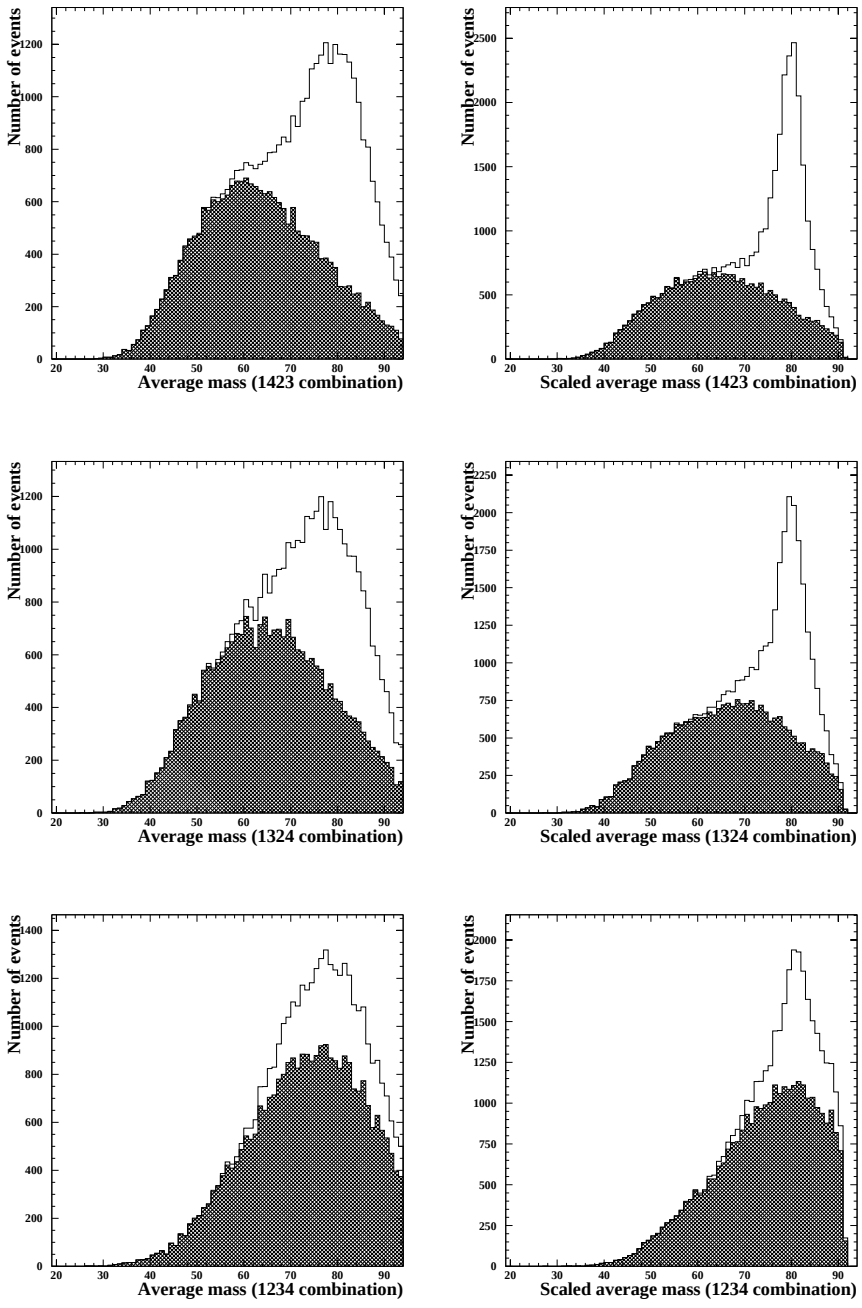

Figure 5.1: The average jet pair mass and the scaled average jet pair mass for the three jet pair combinations. KORALW $W^+W^- \rightarrow q\bar{q}q\bar{q}$ events with $M_W = 80.33$ GeV and $\sqrt{s}$=183 GeV are shown. The hatched histogram is the mass from the wrong jet pair combinations.

5.1.3 Breit Wigner fit

These mass spectra can be fitted with a function to extract the W boson mass. In this simple method MINUIT [62] is used to perform a binned negative log(likelihood) fit to each mass histogram.

The MC used in figure 5.1 has a luminosity of 6369 pb^{-1}. The data taken in 1997 at $\sqrt{s} \approx 183$ GeV has a luminosity of 57 pb^{-1}, 112 times smaller. Figure 5.2 shows a data-sized MC subsample which includes all the expected backgrounds fitted with a Breit Wigner plus a quadratic background. The shape of the background was determined from larger MC samples and only the overall normalisation of the background is allowed to vary. Both the 1423 and the 1324 mass spectra are fitted simultaneously. The seven parameters allowed to vary in the fit are: the two background normalisations, the two Breit Wigner normalisations, the two Breit Wigner widths, and the common mean of the Breit Wigners.

For each data-size MC subsample a value for the W boson mass and the error on the mass are extracted. This is the mean of the Breit Wigner and the error on this mean. This mass will be biased as no account has been taken for effects such as: phase space, ISR, detector effects, and reconstruction effects. The correction of this bias is a very important part of the mass measurement.

5.1.4 Bias correction

The fully GOPALised MC is used to calibrate the mass measurement and correct any bias. How this is done in the main analysis is discussed in detail in section 6.3. The MC samples hopefully treat all the sources of bias properly and faithfully simulate the data. This assumption is discussed in much more detail in section 6.5. The value of M_{W} used to generate the MC samples is known so the difference between this and the value of M_{W} measured from many data-sized subsamples of MC can be used to

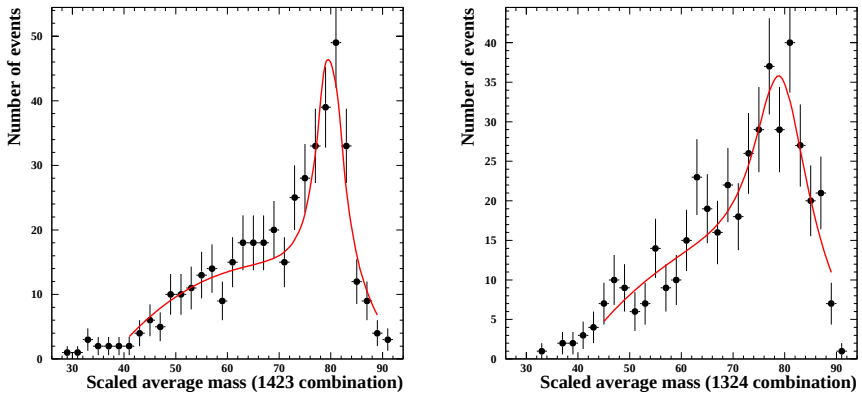

Figure 5.2: The scaled average jet pair mass for a data-sized MC subsample. The subsample contains W^+W^-events from KORALW MC with M_W = 80.33 GeV, PYTHIA $Z^0/\gamma \rightarrow q\bar{q}$ events and PYTHIA $ZZ \rightarrow q\bar{q}q\bar{q}$ events. The mean of the fitted Breit Wigner for this subsample is 79.79±0.43 GeV.

(a) (b)

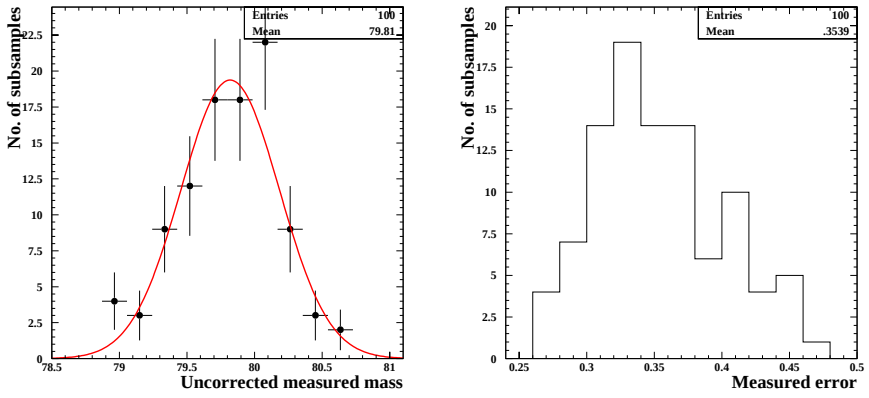

Figure 5.3: a) The means of the Breit Wigners fitted to the scaled average masses for 100 subsamples generated with M_W =80.33 GeV. b) The error on the mean of the fitted Breit Wigner for each subsample.

Source	Expected number of events passing the $W^+W^- \to q\bar{q}q\bar{q}$ likelihood selection
$W^+W^- \to q\bar{q}q\bar{q}$	344.6 ± 1.9
$W^+W^- \to q\bar{q}l\nu$	8.7 ± 0.3
$Z^0/\gamma \to q\bar{q}$	78.6 ± 1.1
$ZZ \to q\bar{q}q\bar{q}$	11.4 ± 0.2
Total expected	443.3 ± 2.2
183 GeV data	448

Table 5.1: The expected number of events in the data sample with the $W^+W^- \to q\bar{q}q\bar{q}$ relative likelihood greater than 0.18. Only the statistical errors are shown.

estimate the bias.

These subsamples contain all the sources of background and are analysed in the same way as the data. Table 5.1 shows the estimated number of events of each kind in the data sample. The standard event selection discussed in section 4.1 is used. In this simple method events are selected if the value of the $W^+W^- \to q\bar{q}q\bar{q}$ relative likelihood is greater than 0.18.

Figure 5.3 shows the measured mass and error for 100 subsamples generated with $M_W = 80.33$ GeV and $\sqrt{s} = 183$ GeV. The difference between the mean of these 100 masses and 80.33 GeV is taken as the mean bias. It is important to also check the dependence of the bias on M_W and E_{beam}, this is discussed in section 6.3.

5.1.5 The statistical error

One can check that the error on the measured W boson mass is a good estimate by looking at the pull distribution. The pull distribution is the (measured mass - true mass) divided by the measured error. If the measured mass and error are accurate the pull distribution should be a Gaussian with mean zero and width one. Figure 5.4 shows the pull distribution using this simple method for 400 MC subsamples formed from the seven KORALW MC samples. The bias correction has been applied to these subsamples so the mean of the pull distribution is automatically zero. The width of the pull distribution is consistent with one.

The expected statistical error on M_W using this simple method for the $q\bar{q}q\bar{q}$ channel is 448±22 MeV. We shall see in the next chapter that this statistical error can be much improved.

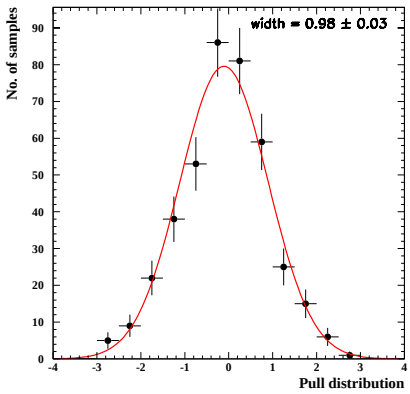

Figure 5.4: The pull distribution for 400 MC subsamples after the bias correction has been made. The pull width, which is calculated from the unbinned rms, is consistent with one.

5.2 Kinematic fitting

In the last section we saw that imposing energy conservation in a simple way on each event improved the mass resolution. An even better mass resolution can be achieved by using a kinematic fit.

A kinematic fit involves making an estimate of the uncertainty on the measured jet/lepton 4-momenta and then imposing some kinematic constraints. Here the total energy of the event is constrained to be $\sqrt{s}$ and the total momentum in an event is constrained to be zero. Additionally the two W boson masses can be constrain to be equal. The jet/lepton momenta are allowed to vary according to their estimated uncertainties so that these constraints are satisfied. The momenta are repeatedly adjusted until the χ^2 for the fit is minimised. The resolution on the mass is substantially improved by using a kinematic fit, this can be seen in figure 5.5.

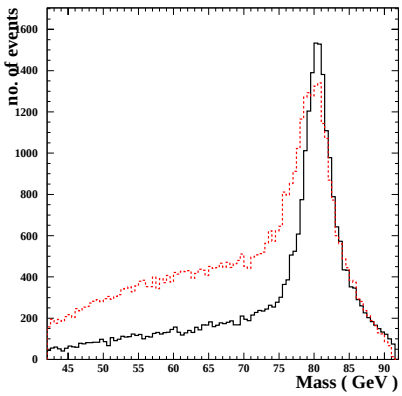

Figure 5.5: The average mass for the 1423 jet combination in $W^+W^- \rightarrow q\bar{q}q\bar{q}$ events. The solid line is the average mass from the 5C kinematic fits with a fit probability greater than 0.1 %. The dashed line is the average invariant mass scaled by the visible energy.

5.2.1 Estimating the errors

The errors on the jet and lepton four momenta are examined in the MC and then parameterised.

The covariance matrix for the jet 4-momentum is filled by the routine WWJECP [47]. The errors assigned to the energy and direction of the jet are roughly the same as described in appendix A of [54]. These errors are

$$\sigma(E) = 0.5E^{0.7} \tag{5.1}$$

$$\sigma(\cot\theta) = \frac{1.35\sin\theta}{E}(1+\cot^2\theta)^{1.5} \tag{5.2}$$

$$\sigma(\phi) = \frac{1.25\sin\theta}{E} \tag{5.3}$$

where E is in GeV. The off-diagonal elements of the covariance matrix are set to zero. The errors on E and $\cot\theta$ are increased by 18 % if the jet goes outside the jet chamber (i.e. $\cos\theta$ >0.92). The error on E is also increased by 5 % if the jet hits the endcap ECAL (i.e. $\cos\theta$ >0.7)

The covariance matrices for the electron and muon 4-momenta are filled by WWLPAR [47]. This uses the errors assigned to the track and/or cluster of the lepton candidate in the DSTs. The magnetic field in the central tracking chamber is parallel to the beam axis so the fractional uncertainty on charged track momentum is approximately proportional to its momentum component transverse to the beam (P_T). For the 1997 data the uncertainties on well measured charged tracks are [59]

$$\sigma(P_T) \approx P_T\sqrt{(0.020)^2+(0.0015P_T)^2} \tag{5.4}$$

$$\sigma(\theta) \sim 1\ mrad \tag{5.5}$$

$$\sigma(\phi) \sim 0.3\ mrad \tag{5.6}$$

The uncertainty on the energy of a ECAL cluster is

$$\sigma(E) \approx 0.25\sqrt{E} \tag{5.7}$$

The energy of the ECAL cluster and the direction of the charged track are used for the electron candidates. The direction and the momentum of the charged track are used for the muon candidates since only a fraction of the muon's energy is lost in the ECAL.

The covariance matrix for the 4-momentum of the tau jet is filled by WWJEYI [55]. Only the tau jet direction not its energy is used. The tau decay neutrino will have carried away a significant fraction of the taus energy but not much transverse momentum due to the relatively small mass of the tau.

Data taken at $\sqrt{s}=M_{\mathrm{Z}}$ are compared with MC at $\sqrt{s}=M_{\mathrm{Z}}$ to check that these parameterisations of the errors are accurate [69] [56] [57]. One can use two and three jet events to assess the jet errors. In two jet events the sum of the two jet energies $E_1 + E_2$ should be equal to the Z mass, $\cos\theta_1 + \cos\theta_2$ should be zero, and $\phi_1 - \phi_2$ should equal to π. The resolution of these quantities can be used to find the errors on the jet 4-momenta. In three jet events the energies of the jets can be calculated from their angles. These calculated energies can be compared with measured energies. The lepton 4-momentum errors can be assessed by looking at $\mathrm{Z} \to \mathrm{e}^+\mathrm{e}^-$, $\mathrm{Z} \to \mu^+\mu^-$, and $\mathrm{Z} \to \tau^+\tau^-$ events. The same method is used as in the two jet case. The parameterisation of the errors is found to be a good estimate of the true errors. Any differences between the errors in the MC and the data are found and a systematic error due to this mis-modelling is assigned.

5.2.2 Performing the fit

Consider the $q\bar{q}e\nu$ case first. Here the four momenta of the two jets and the electron are measured and the four momentum of the neutrino is unmeasured. The mass of the neutrino is assumed to be zero so this leaves three unmeasured quantities. If the two W boson masses are constrained to be equal there are five constraint equations: energy conservation, 3 $\times$ momentum conservation, and the equal mass constraint. The number of constraint equations minus the number of unmeasured quantities gives the number of degrees of freedom and this is used to label the fits. In this case it gives a two constraint (2C) fit.

The observables are labelled [2] $\underline{\eta}$. There are twelve of them: the 4-momenta of the two jets and the electron. The measured values of these observables are labelled $\underline{y}$ with their errors in the covariance matrix $V(\underline{y})$. The unmeasured quantities are labelled $\underline{\xi}$. The constraint equations are labelled $\underline{f}(\underline{\eta},\underline{\xi})$. Each constraint equation should be equal to zero, so the energy constraint equation would be

$$f_1 = E_{jet1} + E_{jet2} + E_e + \mid \underline{P_\nu} \mid -\sqrt{s} \tag{5.8}$$

The 'improved' measurements of the observables are given when the following equations are satisfied.

$$\chi^2(\eta) = (\underline{y} - \underline{\eta})^T V^{-1} (\underline{y} - \underline{\eta}) = minimum \tag{5.9}$$

$$\underline{f}(\underline{\eta},\underline{\xi}) = \underline{0} \tag{5.10}$$

This could be achieved by eliminating five unknowns from the constraint equations 5.10, substituting in 5.9 and then minimising this in the normal way. If the constraint equations are non-linear a better method is to use Lagrange multipliers. Rather than eliminating the unknowns, five additional unknowns ($\underline{\lambda}$) are introduced and the

[2] This section is based on reference [58].

problem rephrased as

$$\chi^2(\eta, \underline{\xi}, \underline{\lambda}) = (\underline{y} - \underline{\eta})^T V^{-1} (\underline{y} - \underline{\eta}) + 2\underline{\lambda} \underline{f}(\underline{\eta}, \underline{\xi}) = minimum \tag{5.11}$$

This is minimised iteratively. The exact details of how this is done can be found in [58]. The new improved estimates for the observed and unobserved quantities are used to calculate the average W boson mass in each event.

The $W^+W^- \rightarrow q\bar{q}\tau\nu$ channel has the added complication that the tau is not observed, only its decay products. One of these decay products will be another neutrino. The direction of the tau is approximated by the sum of the momenta from the visible decay products and the magnitude of this momentum is assumed to be unknown. So the fit used for the $q\bar{q}\tau\nu$ candidates is a 1C fit.

In the $W^+W^- \rightarrow q\bar{q}q\bar{q}$ channel there is no missing neutrino so this gives a 5C fit. A 4C fit without the equal mass constraint is also used in this channel to help decide which is the right jet pair combination.

5.2.3 The equal mass constraint

Consider the case where the resolution of the detector is perfect. The reconstructed mass spectra for the two Ws in an event would be Breit Wigners with width Γ_W. If these two masses were averaged the mass spectrum would still be a Breit Wigner with width Γ_W. The uncertainty on the mean of a Breit Wigner varies as $\Gamma/\sqrt{n}$ where Γ is the width and n is the number of entries. Since averaging the two W masses per event halves the number of entries and keeps the width constant the uncertainty on the mean would be increased by $\sqrt{2}$.

Now consider the case where the resolution of the detector is very bad and the reconstructed mass spectra for each W is a Gaussian with width σ_R. If the two W masses per event were averaged the mass spectrum would be a Gaussian with width $\sigma_R/\sqrt{2}$. The uncertainty on the mean of the Gaussian again varies as $\sigma/\sqrt{n}$ where

σ is the width and n is the number of entries. Since averaging the two W masses reduced the width by $\sqrt{2}$ the uncertainty on the mean would stay the same.

In reality the mass spectra for the two measured Ws are somewhere between a Gaussian and a Breit Wigner. So one might expect the uncertainty on the mean value to increase slightly if the average mass was used. As mentioned in section 5.1.2 the two reconstructed W masses in an event are anti-correlated. This reduces the width of the average mass spectrum which means that in practise the 5C fit mass is much better than the two 4C fit masses separately and a little bit better than the average 4C fit mass. Figure 5.6 shows the 4C and 5C mass distributions .

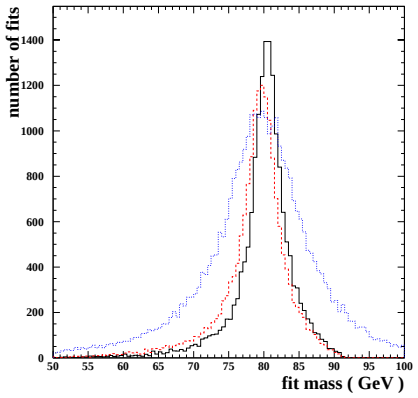

Figure 5.6: The fitted mass for the 1423 jet combination where this is the correct jet combination in KORALW $q\bar{q}q\bar{q}$ events. The solid line is the 5C fit mass. The dotted line is the 4C fit masses separately. The dashed line is the average 4C fit mass.

Also the two Ws in an event should have similar masses, but the wrong jet combinations and the background events may produce two masses which are quite different. Applying the equal mass constraint means that the kinematic fit is more likely to fail or have a high χ^2 for the wrong combinations and the background events.

5.2.4 Problems with the kinematic fit

Mass overestimate due to ISR

If one or more ISR photons have been emitted the total energy of the two Ws will be less than $\sqrt{s}$ and their total momentum will not be zero (unless two or more photons are emitted which exactly balance the momentum). If the ISR photon(s) escape detection down the beam pipe the energy conservation constraint will make the kinematic fit over estimate the energy of the jets and leptons. This will mean that the reconstructed W boson mass for those events with significant ISR will be overestimated and the fits for these event will have larger χ^2 values.

Error underestimate due to kinematic limit

Energy conservation means that is impossible to have a reconstructed average W boson mass greater than the beam energy. This has an unwanted effect on the error from the kinematic fit on this average mass. If the average mass is close to the beam energy, say 91 GeV and the beam energy is 91.5 GeV the mass can not have an upper error bound bigger than 0.5 GeV as masses bigger than the beam energy are not allowed. The lower error bound should be bigger than this but the fit returns symmetric errors. So the error on the average mass is underestimated for those fits with an average mass close to the beam energy. Figure 5.7 shows the error versus the average mass for $q\bar{q}e\nu$ events; one can see that the error tends to zero as the average mass tends to the beam energy. Figure 5.8 shows the pull width versus the average mass for $q\bar{q}e\nu$ events and for $q\bar{q}e\nu$ events with less than 50 MeV of ISR. Most of the events with masses close to the beam energy underestimate the error (i.e. the pull values are large) and most of these events have large amounts of ISR. This effect

could be corrected by dividing the errors by

$$\sqrt{1-(\frac{m}{E_{beam}})^2} \tag{5.12}$$

This is empirically found to correct the errors and the pull width. However since the events with average masses close to the beam energy often have large amounts of ISR, and hence over estimated masses, it seems sensible to throw away these events rather than trying to correct their errors. A minimum cut is put on the fit error, this cut is shown in table 5.2. A larger cut value is used in the $q\bar{q}\tau\nu$ channel due to the worse mass resolution. This only removes those fits with average masses close to the beam energy.

Given the χ^2 and the number of degrees of freedom for a fit one can work out a fit probability. Fits with very large χ^2 have very low fit probabilities. A minimum cut is placed on the fit probablities, the value of the cut is shown in table 5.2. This helps to remove background events, wrong combinations and baddly reconstructed events. A larger cut value is used for the $q\bar{q}q\bar{q}$ 1234 jet combination to further reduce the number of badly reconstructed events.

channel/combination	cut on fit error (GeV)	cut on fit probability
$q\bar{q}q\bar{q}$ 1234	>0.4	>0.01
$q\bar{q}q\bar{q}$ 1324	>0.4	>0.001
$q\bar{q}q\bar{q}$ 1423	>0.4	>0.001
$q\bar{q}e\nu$	>0.5	>0.001
$q\bar{q}\mu\nu$	>0.5	>0.001
$q\bar{q}\tau\nu$	>0.9	>0.001

Table 5.2: The cut values used by the convolution method on the kinematic fits.

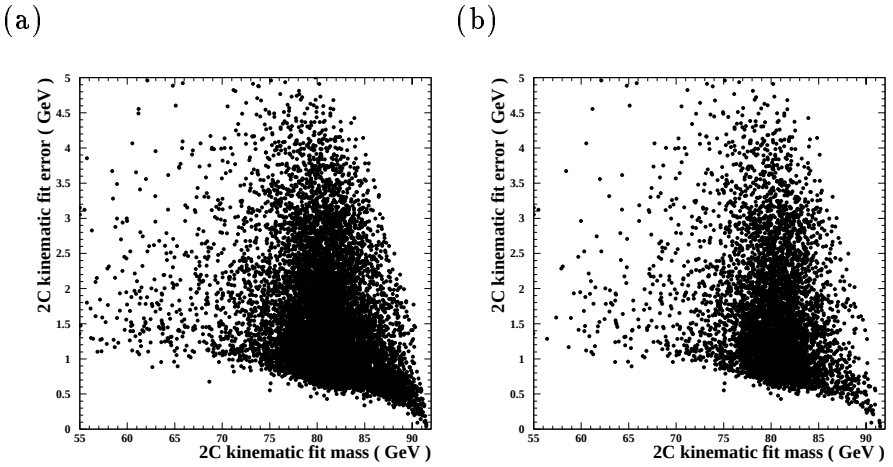

Figure 5.7: a) The 2C kinematic fit error versus the 2C kinematic fit mass for a) all $q\bar{q}e\nu$ KORALW events. b) The $q\bar{q}e\nu$ KORALW events with less than 50 MeV ISR.

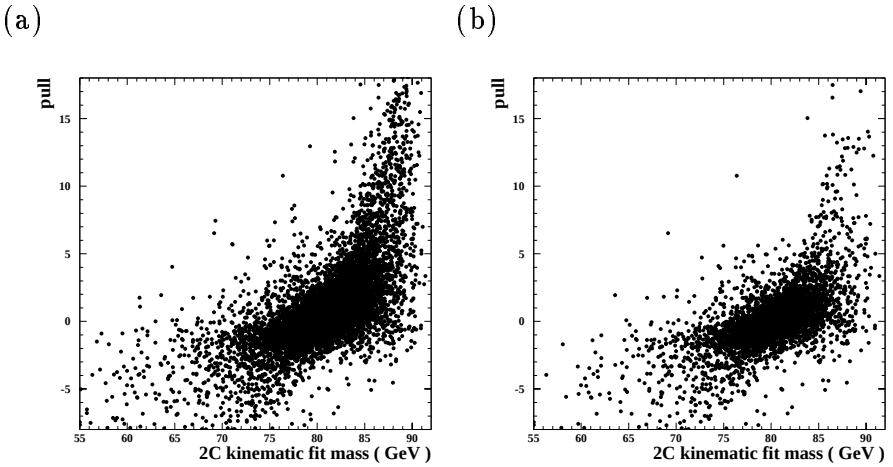

Figure 5.8: The 2C kinematic fit pull versus the mass for $q\bar{q}e\nu$ events. The pull is the (2C mass - MC mass) divided by the 2C error. a) for all $q\bar{q}e\nu$ KORALW events. b) The $q\bar{q}e\nu$ KORALW events with less than 50 MeV ISR.

Non-Gaussian errors

The errors on the jet and lepton four momenta that are used in the kinematic fit are only an estimate. Gaussian errors are assumed but in reality (and in the MC) the resolution (the measured value - the true value) is not Gaussian. Sometimes the jet reconstruction goes wrong or the lepton is assigned to the wrong track or cluster. In these cases the measured value for the jet or lepton 4-momentum will be very different to its true 4-momentum and the fitted mass may be very different to its true value.

Figure 5.9 shows the resolution of the 2C kinematic fit mass for $q\bar{q}e\nu$ KORALW events in slices of the fit errors. The resolution has much longer tails than a Gaussian. A simple Breit Wigner is found to be a better estimate of the fit resolution function. Fits with errors less than 0.5 GeV are thrown away because they are mostly events with significant ISR and over estimated measured masses. Fits with errors between 0.5 and 0.66 GeV are kept but one can see that the resolution for a large fraction of these fits is very poor.

5.3 Other mass measurement methods

Several methods have been proposed and used to measure the W boson mass at LEP. The two other methods used to analyse the data taken at $\sqrt{s}$=172 GeV and $\sqrt{s}$=183 GeV by the OPAL detector are discussed.

5.3.1 Breit Wigner fit method

This is the most obvious practical method [48] [68]. It is very similar to the simple method described above except that it uses the kinematic fit and uses a more complicated function to fit to the mass spectrum.

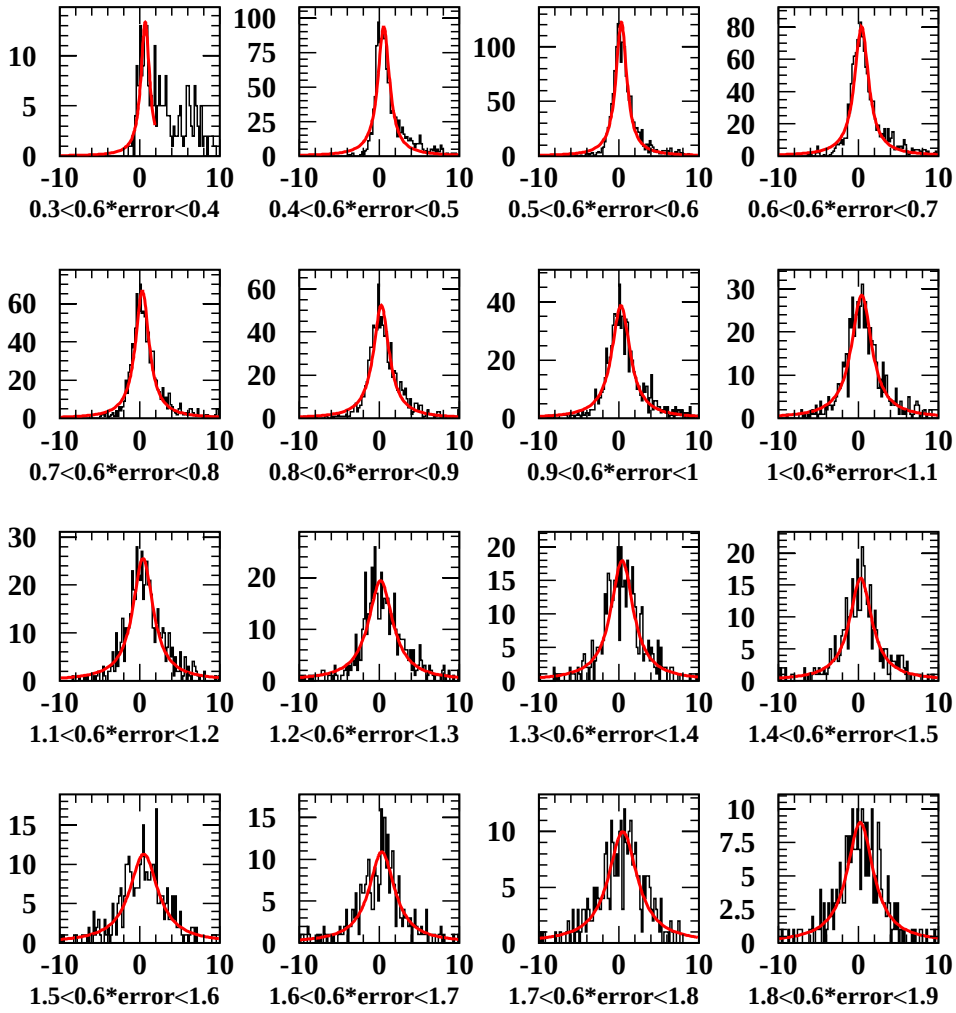

Figure 5.9: The resolution (fitted mass - true mass) of the 2C kinematic fit for $q\bar{q}e\nu$ KORALW events. The reason why the errors are multiplied by 0.6 will be discussed in section 6.2.2. A Breit Wigner is fitted to these distributions.

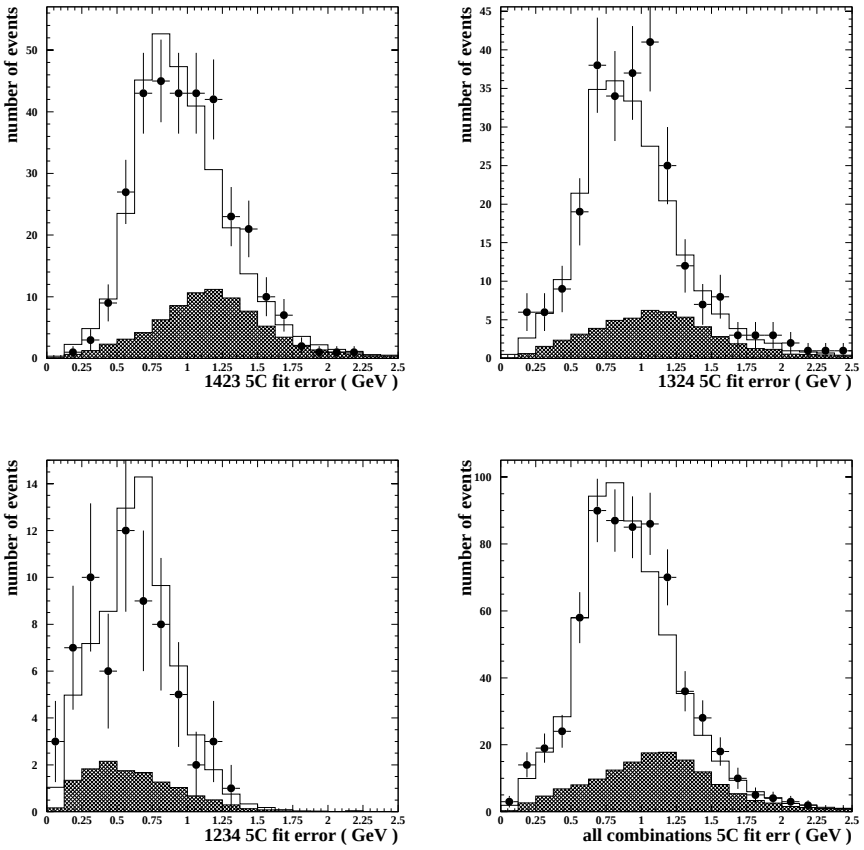

Figure 5.10: The 5C kinematic fit error for each jet combination and for them all together. Only those fits which pass the fit probability cut are shown. The points are the 183 GeV data. The hatched histogram is the $W^+W^- \to q\overline{q}q\overline{q}$ signal, the open histogram is the sum of the signal and backgrounds from $Z^0/\gamma \to q\overline{q}$, $W^+W^- \to q\overline{q}l\nu$ and $ZZ \to$ all.

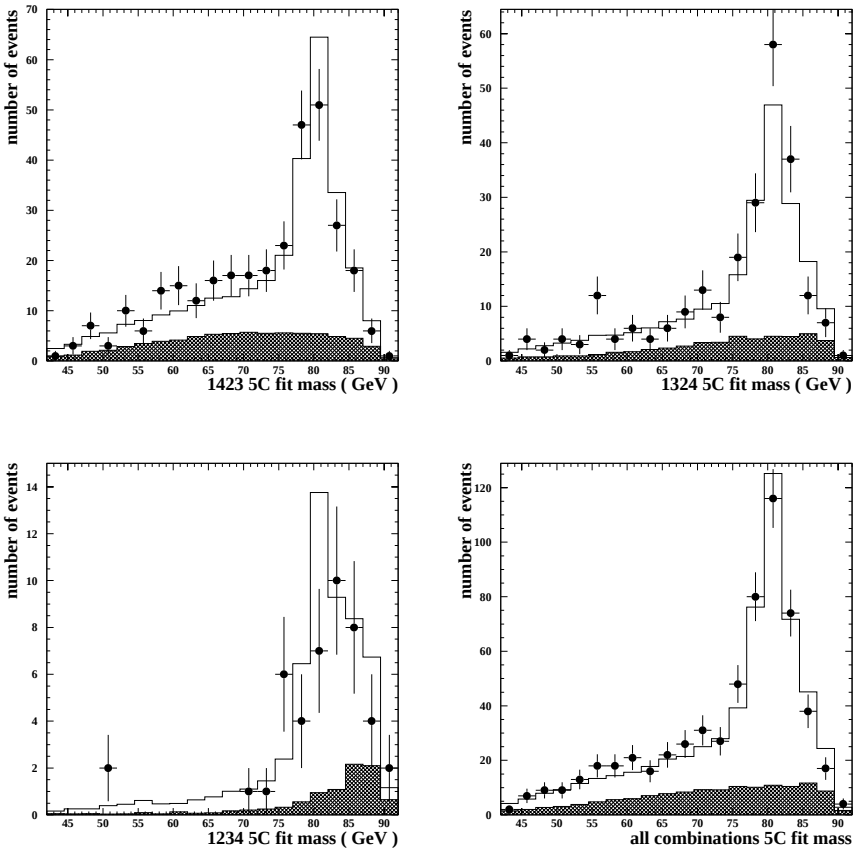

Figure 5.11: The 5C kinematic fit mass for each jet combination and for them all together. Only those fits which pass the fit probability cut and fit error cut are shown. The points are the 183 GeV data. The hatched histogram is the $W^+W^- \rightarrow q\overline{q}q\overline{q}$ signal, the open histogram is the sum of the signal and backgrounds from $Z^0/\gamma \rightarrow q\overline{q}$, $W^+W^- \rightarrow q\overline{q}l\nu$ and $ZZ \rightarrow$ all.

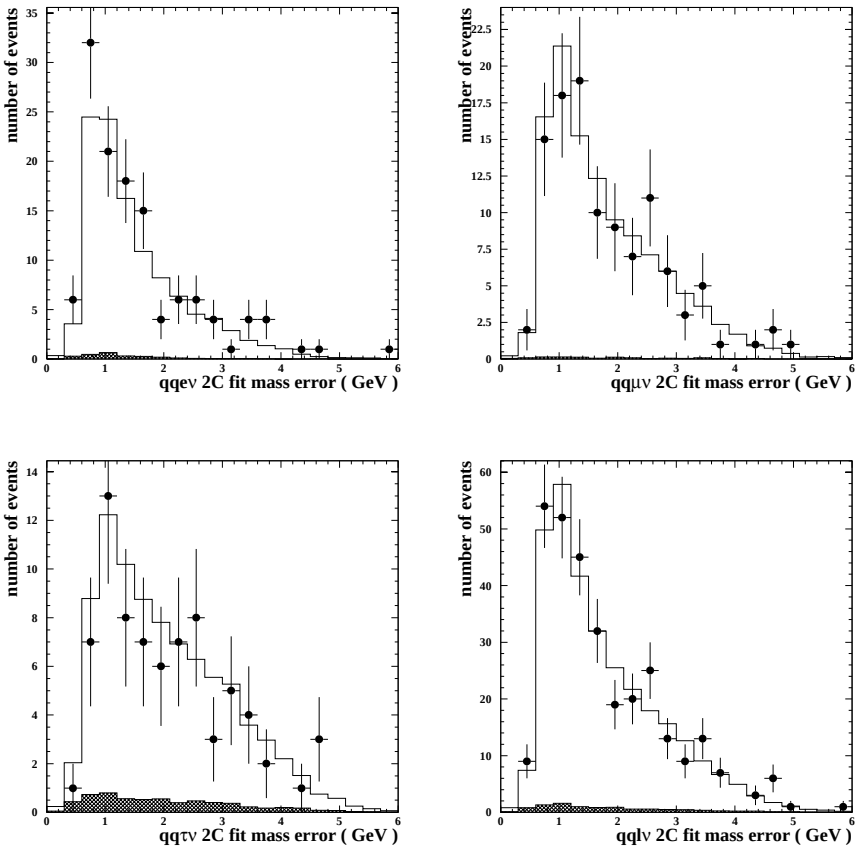

Figure 5.12: The 2C kinematic fit error for the $q\bar{q}l\nu$ channels. Only those fits which pass the fit probability cut are shown. The points are the 183 GeV data. The hatched histogram is the signal, the open histogram is the sum of the signal plus $Z^0/\gamma \rightarrow q\bar{q}$ and four fermion backgrounds.

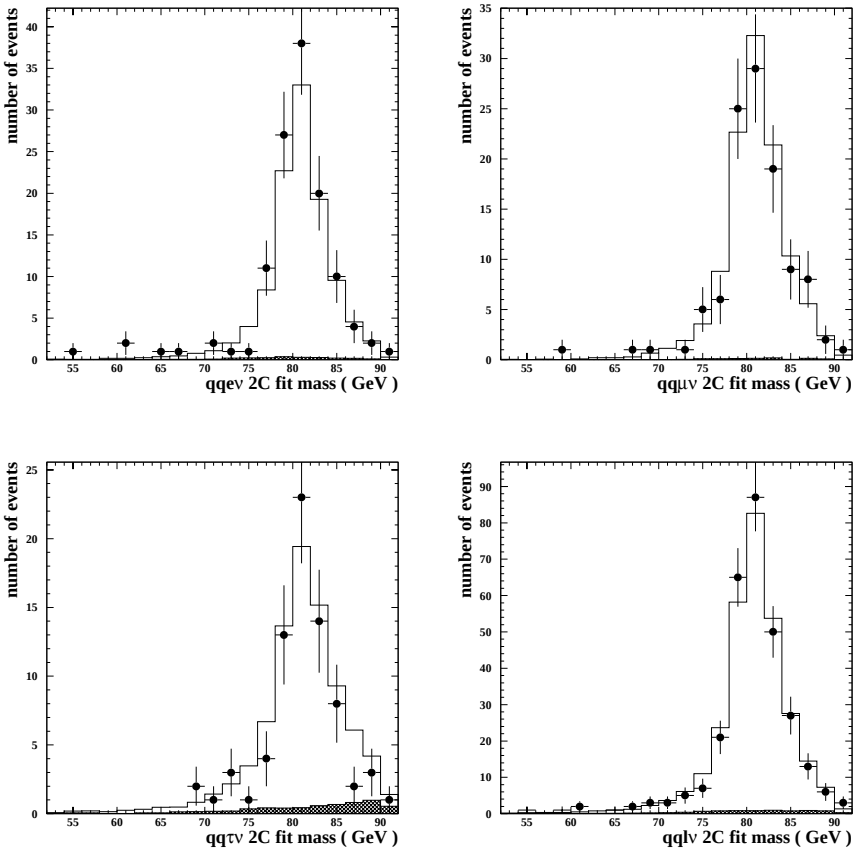

Figure 5.13: The 2C kinematic fit mass for the $q\bar{q}l\nu$ channels. Only those fits which pass the fit probability cut and fit error cut are shown. The points are the 183 GeV data. The hatched histogram is the signal, the open histogram is the sum of the signal plus $Z^0/\gamma \rightarrow q\bar{q}$ and four fermion backgrounds.

In the $q\bar{q}e\nu$ and $q\bar{q}\mu\nu$ channels the 2C kinematic fit mass is used if the fit probability is greater than 0.1 %. These masses are histogrammed and a function fitted to the histogram. The function used is generally a relativistic Breit Wigner times some phase space term plus a polynomial background. A more complex Breit Wigner with different widths above and below the peak value is sometimes used. The value of M_W for the data sample is taken from the mean of the Breit Wigner and then corrected for biases.

In the $q\bar{q}q\bar{q}$ channel the jet pair combination with the highest 5C kinematic fit probability is generally used. Sometimes the combination with the second highest fit probability is also used and histogramed separately. Other more complex ways of deciding which combination is best can be used but they all generally select one or two combinations rather than using each combination with a given weight. A function is fitted to the mass histogram and the value for M_W is extracted and corrected for biases in the same way as for the $q\bar{q}l\nu$ case.

5.3.2 Reweighting method

This is the standard method used in the OPAL analysis [48] [68]. The masses from the kinematic fit are histogramed in the same way as the Breit Wigner method. Instead of fitting a function to the mass histogram it is compared to fully simulated MC mass histograms generated with different values for M_W . The value of M_W is extracted from the MC that best fits the data.

If there were many different large MC samples with different values for M_W , a likelihood curve could be calculated and the value of M_W that makes the data most likely extracted. Generating large fully GOPALised MC samples with many different M_W values would take too much computing time. Instead one large MC sample can have its events reweighted so that it appears to have been generated with a different

value of M_{W} [60]. This reweighting can also be used to simulate MC samples with different W boson widths (Γ_{W}). The reweighting function (f) is the probability that the event was produced with the new M_{W} and Γ_{W} divided by the probability that the event was produced with the actual generated M_{W} and Γ_{W} . This can be well approximated by the ratio of four Breit Wigners.

$$f = \frac{BW(M_{\mathrm{W}}{}^{new}, \Gamma_{\mathrm{W}}{}^{new}, m_1) \times BW(M_{\mathrm{W}}{}^{new}, \Gamma_{\mathrm{W}}{}^{new}, m_2)}{BW(M_{\mathrm{W}}{}^{gen}, \Gamma_{\mathrm{W}}{}^{gen}, m_1) \times BW(M_{\mathrm{W}}{}^{gen}, \Gamma_{\mathrm{W}}{}^{gen}, m_2)} \tag{5.13}$$

where BW is a relativistic Breit Wigner and m_1 and m_2 are the two generator level W masses for the event. This reweighting becomes less effective when the difference between the original generated M_{W} and the new M_{W} becomes large (more than 1 GeV). This is because the reweighting function f becomes large and the effective statistical precision is reduced. To counteract this several large MC sample with values of M_{W} 0.5 GeV apart are generated. New samples at arbitrary values of M_{W} between these samples can be accurately simulated. If the MC samples account for all the physical and detector effects the W boson mass measured by this method will be unbiased and not need explicit bias corrections.

Chapter 6

The convolution method

This chapter contains the main analysis of this thesis. The W boson mass is measured using the convolution method. The main motivation for the convolution method is that it tries to make optimal use of the information in an event.

As some events have a much smaller uncertainty on the measured mass than other events, treating all the events on an equal footing does not use all the information. If the 'well measured' events were given a higher weighting, the statistical uncertainty on the final value for M_{W} could be reduced. None of the methods mentioned previously use the error on the kinematic fit mass to improve the mass measurement.

The convolution method, unlike the Breit Wigner fitting method and the Reweighting method, makes use of all three jet pair combinations in the $\mathrm{q\bar{q}q\bar{q}}$ channel. The other methods try to select the best combination or sometimes the best two combinations and neglect the other(s). The way in which the best combination is decided has an important effect on the uncertainty of the M_{W} measurement in this channel and is discussed in section 6.2.1.

Another important piece of information that can be used is the underlying physical mass distribution, which is theoretically well understood. The convolution method uses all these pieces of information in an elegant and efficient manner.

6.1 The basic idea

6.1.1 The $q\bar{q}l\nu$ channel

Consider the $q\bar{q}l\nu$ channel first as it does not have the complications of more than one jet combination. For each event one knows three pieces of important information: the underlying physical mass spectrum, the kinematic fit average mass, and the resolution of the kinematic fit.

The underlying mass spectrum

The underlying mass spectrum (UMS) is the produced W boson mass spectrum without any detector effects. The underlying mass spectrum is essentially a relativistic Breit Wigner modified by phase space, ISR and interconnection effects. Initially just consider the relativistic Breit Wigner. The probability for producing a W boson with mass m given M_{W} and Γ_{W} would be

$$\rho(m \mid M_{\mathrm{W}}, \Gamma_{\mathrm{W}}) = \frac{\Gamma_{\mathrm{W}}}{\pi M_{\mathrm{W}}} \frac{m^2}{\left(m^2 - {M_{\mathrm{W}}}^2\right)^2 + m^4 (\Gamma_{\mathrm{W}}/M_{\mathrm{W}})^2} \tag{6.1}$$

The probability distribution is the same if m is the average W boson mass per event. Section 5.2.3 discusses why the average mass per event is used rather than the two separate masses.

The effects of phase space and ISR can be simulated by semi-analytical or MC programs. For this analysis it is more sensible to make some approximations and use a simple expression for the UMS. At $\sqrt{s}$=183 GeV phase space is the most important correction to the Breit Wigner shape. The effects of phase space can be approximated by multiplying the Breit Wigner by

$$PS(m \mid \sqrt{s}) = \sqrt{1 - \frac{m^2}{E_{beam}}} \tag{6.2}$$

where again m is the average mass per event and E_{beam} is the beam energy, which is equal to half $\sqrt{s}$.

The effects of ISR and interconnection are ignored in the approximation of the underlying mass spectrum. The MC will be needed to calibrate the measured value of M_{W}, if the MC simulates ISR and interconnection effects accurately the measured value of M_{W} should not be affected by their exclusion from the UMS.

The approximation used to describe the probability of producing an average W boson mass m given M_{W} , Γ_{W} and $\sqrt{s}$ is

$$\rho(m \mid M_{\mathrm{W}}, \Gamma_{\mathrm{W}}, \sqrt{s}) = BW(m \mid M_{\mathrm{W}}, \Gamma_{\mathrm{W}}) \times PS(m \mid \sqrt{s}) \tag{6.3}$$

$$= \frac{1}{\pi} \frac{\Gamma_{\mathrm{W}}/2}{(m - M_{\mathrm{W}})^2 + (\Gamma_{\mathrm{W}}/2)^2} \sqrt{1 - \left(\frac{m}{E_{beam}}\right)^2} \tag{6.4}$$

Here a non-relativistic Breit Wigner (BW) is used instead of a relativistic Breit Wigner, the difference in the actual shape of the function is minimal and a simple Breit Wigner will simplify the convolution discussed in the following event likelihood section. Figure 6.1 shows the average W boson mass in KORALW events fitted with the expression for the ρ in equation 6.4. This expression is a good fit except at low masses where it over estimates the probability slightly, this range of masses is of little interest.

The resolution function

The resolution is the difference between the measured mass and the true mass. If the error on the measured mass was a true Gaussian error the resolution function would be a Gaussian with width given by this error.

The actual resolution function for KORALW $q\overline{q}e\nu$ events is shown in figure 5.9. A simple non-relativistic Breit Wigner with width proportional to the error on the measured mass is found to be a better approximation to the resolution function than

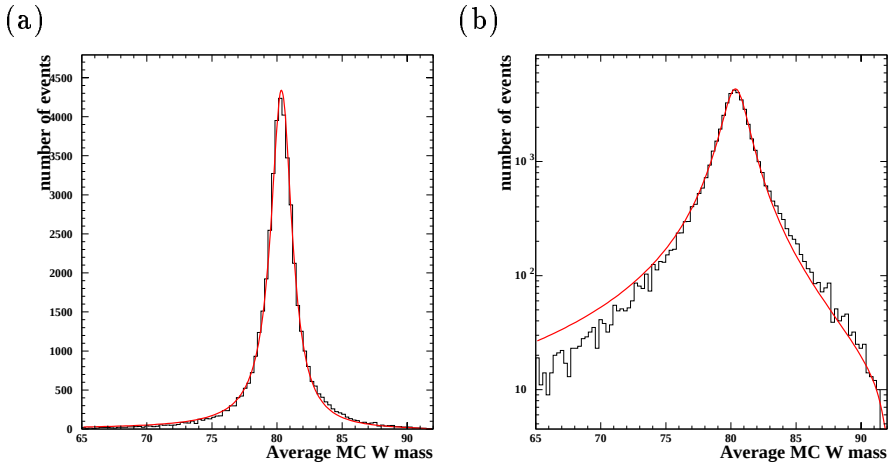

Figure 6.1: The histogram is the average generated W mass per event in KORALW events. The fitted function is the expression for ρ in 6.4. a) uses a linear y axis and b) uses a logarithmic y axis to aid the comparison.

a Gaussian. So the resolution function used is

$$R(m, \sigma_R) = \frac{\sigma_R}{(m - m')^2 + \sigma_R^2} \tag{6.5}$$

where m is the measured average mass and σ_R is proportional to the error on the mass. The exact relation between σ_R and the kinematic fit error is discussed in section 6.2.2.

The event likelihood

How likely each event is as a function of M_{W} can now be constructed from the underlying mass spectrum (UMS), the kinematic fit mass, and the resolution function. In order to construct an event likelihood the UMS should be expressed as a function of m_{W} given the fit results, where m_{W} is the postulated value for the true W boson

mass M_{W} .

$$UMS(m_{\mathrm{W}} \mid m_f) = \frac{1}{\pi}\frac{\Gamma_{\mathrm{W}}/2}{(m_f - m_{\mathrm{W}})^2 + (\Gamma_{\mathrm{W}}/2)^2}\sqrt{1 - (\frac{m_{\mathrm{W}}}{E_{beam}})^2} \tag{6.6}$$

Here m_f is used to represent the kinematic fit results, these include both the mass and the error on the mass.

The probability density function for the signal (f_s) is the convolution of the underlying mass spectrum with the resolution function.

$$f_s(m_{\mathrm{W}} \mid m_f) = UMS(m_{\mathrm{W}} \mid m_f) \otimes R(m_f) \tag{6.7}$$

This convolution can be computed numerically for any UMS and R, luckily the functions chosen here can be convoluted analytically. The phase space function is independent of m_f and so can be removed from the convolution.

$$f_s(m_{\mathrm{W}} \mid m_f) = (BW(m_{\mathrm{W}} \mid m_f) \otimes R(m_f)) \times PS(m_{\mathrm{W}}) \tag{6.8}$$

The convolution of two simple Breit Wigners with widths $\Gamma_{\mathrm{W}}/2$ and σ_R is another simple Breit Wigner with width $\Gamma_{\mathrm{W}}/2 + \sigma_R$. So

$$f_s(m_{\mathrm{W}} \mid m_f) = \frac{1}{\pi}\frac{\Gamma_{\mathrm{W}}/2 + \sigma_R}{(m_f - m_{\mathrm{W}})^2 + (\Gamma_{\mathrm{W}}/2 + \sigma_R)^2}\sqrt{1 - (\frac{m_{\mathrm{W}}}{E_{beam}})^2} \tag{6.9}$$

If the resolution was perfect (i.e. σ_R was equal to zero) f_s would just be the UMS. As the resolution gets worse the width of the f_s peak increases.

If p_s is the probability that the event is a signal event, then the event likelihood is

$$\mathcal{L}(m_{\mathrm{W}} \mid m_f) = p_s f_s(m_{\mathrm{W}} \mid m_f) \quad + \quad (1 - p_s) f_b(m_f) \tag{6.10}$$

where f_b is the probability density function (pdf) for the background, this should not depend on m_{W} . An estimate for f_b can be taken from the MC or otherwise approximated. When m_{W} equals the fit mass (m_f) the event is most likely. How

much less likely the event is at values of m_{W} slightly different from m_f depends on the W boson width plus the resolution width.

Several approximations are made in the actual analysis and so the measured m_{W} will only be an approximation of the true W boson mass, and will need to be corrected for any bias. The statistical error on the measured m_{W} will also only be an approximation and must be calibrated carefully unlike the error from the reweighting and Breit Wigner fit methods.

6.1.2 The $\mathrm{q\bar{q}q\bar{q}}$ channel

The $\mathrm{q\bar{q}q\bar{q}}$ channel is more complicated because there are the 3 possible jet pair combinations. Fortunately the convolution method is well suited to dealing with this type of problem. For each jet pair combination i one can construct a pdf $f_s(m_{\mathrm{W}} \mid m_f^i)$ in the same way as before (i.e. convoluting the underlying mass spectrum with the resolution function for each kinematic fit). If one can then estimate the probability that each combination is the correct one (p_i) as well as the probability that the event is a signal event (p_s) then the event likelihood becomes

$$\mathcal{L}(m_{\mathrm{W}} \mid m_f) = p_s \sum_{i=1}^{i\leq 3} [\ p_i f_s(m_{\mathrm{W}} \mid m_f^i) \prod_{j\neq i}^{j\leq 3} f_w(m_f^j)\ ] \ + \ (1-p_s) \prod_{k=1}^{k\leq 3} f_b(m_f^k) \quad (6.11)$$

where f_w is the pdf for the wrong combinations and f_b is the pdf for the background as before.

This expression for the event likelihood looks quite complicated. It may be helpful to discuss the origin of each term. The term multiplied by p_s is what the likelihood would be if there was no background. The part of this term in the square bracket is the probability that combination i is the correct one times the pdf for this combination assuming it is the correct one times the pdf for the other two combinations assuming they are the wrong ones. The other two permutations of this are added. Note that the p_i should sum to one. The term multiplied by $(1-p_s)$, the probability that

the event is background, is the product of the three pdfs assuming that the event is background.

How f_w, f_b, p_s and p_i are actually estimated is discussed in the next section.

6.2 Practical details

6.2.1 Jet combination probability

There are several variables that can be used to estimate which combination is the correct one. These variables will be discussed and the reasons why they are or are not used in this analysis outlined.

Jet charge

The sum of the charges from all the tracks in the two jets produced by the W^+ should add to plus one, and similarly the sum of charges from the two jets produced by the W^- should add to minus one. So if the jet reconstruction, charge measurement and jet pairing are totally accurate the difference between the sum of charges for the two jet pairs should be 2. That is, if Q_1 is the sum of the charges of jet 1 and the correct combination is 1234 then ΔQ_{1234} will equal 2 where

$$\Delta Q_{1234} = \mid Q_1 + Q_2 - Q_3 - Q_4 \mid \tag{6.12}$$

The wrong combinations charge differences ΔQ_{1324} and ΔQ_{1423} will on average be 2/3 and 0 respectively. Obviously in practise not all the tracks are reconstructed or assigned to the right jets. In particular those tracks with transverse momentum less than 0.15 GeV are not included in the jet reconstruction at all. Luckily the high momentum tracks carry most of the information as they are likely to carry the initial

decay quark. So a normalised momentum weighted sum like

$$Q_i = \frac{\sum_{j=1}^{j=ntot} q_j P_j}{\sum_{k=1}^{k=ntot} P_k} \tag{6.13}$$

is more effective. Here $ntot$ is the total number of tracks in a jet, q_j is the charge of track j, and P_j is the momentum of track j. However the measured jet charge difference is still not very accurate and is not a reliable way of deciding how probable each combination is.

W production angle

Each jet combination would have the W^- boson being produced at some angle θ from the beam axis. In the standard model with zero values for all the anomalous Triple Gauge boson Couplings (TGCs) [61] the W^- production angle is predicted to be peaked in the e^- direction. This information could be used to decide how probable each combination is. One problem is that the jet charge is needed to decide which is the W^+ and W^-. Another problem is that the TGCs may not be zero, which may add a systematic bias to the result.

Mass difference

The two W boson masses in each event should be close to each other since they are produced from a Breit Wigner with the same mean and width Γ_W . So the right jet combination masses should be similar but the wrong jet combination masses can be quite different. This mass difference by itself is a good way to decide how probable each combination is. There are ways to improve on this however.

5C fit probability: The 5C fit constrains both masses to be equal. So 5C fits for combinations where masses are very different will either fail or have very high χ^2 values and very low fit probabilities. Using the 5C fit probability is a very good way of deciding how probable each combination is. It has the bonus that all combinations

with non-zero probabilities have a 5C fit that worked, this is not necessarily the case with other methods.

4C mass difference variable: One can try to use all the information available about the mass difference. One knows the 4C kinematic fit mass difference, the error on this, and the underlying mass difference spectrum (which should be a Breit Wigner with width Γ_W). All this information can be combined in an expression for the combination probability

$$p_i \propto \int_{-\infty}^{+\infty} BW(\Delta \mid 0, \Gamma_W) R(\Delta \mid \Delta_m, \sigma) d\Delta \tag{6.14}$$

where Δ_m is the 4C mass difference, σ is the error on this, BW is a Breit Wigner with mean zero and width Γ_W , and R is the resolution function with mean Δ_m and width σ.

If the resolution were perfect (i.e. R equals a delta function at Δ_m) p_i would just be the value of BW at Δ_m (i.e. p_i would be large when $\Delta_m \sim 0$ and small when $\Delta_m \gg \Gamma_W$) . If some approximations are made this expression can be simplified. The resolution is taken to be a Gaussian and the BW is replaced by a Gaussian with width Γ_W . The product of two Gaussians is just another Gaussian so the integral becomes trivial and the expression for p_i becomes

$$p_i \propto ({\Gamma_W}^2 + \sigma^2)^{-\frac{1}{2}} \exp \frac{-{\Delta_m}^2}{2({\Gamma_W}^2 + \sigma^2)} \tag{6.15}$$

These probabilities should be normalised so that their sum is one. This is a very effective way of deciding how probable each combination is.

Rather than using just one of these variables one could combine all or some of them in a relative likelihood. This was tried but it was found that the combination of variables was no more effective than the 4C difference variable by itself. So the 4C difference variable is the one that is used in this analysis.

6.2.2 The kinematic fit error

Unlike the reweighting and Breit Wigner fit mass measurement methods discussed in section 5.3 the convolution method makes use of the kinematic fit error. It is necessary to check how good this error is at estimating the uncertainty of the fitted mass.

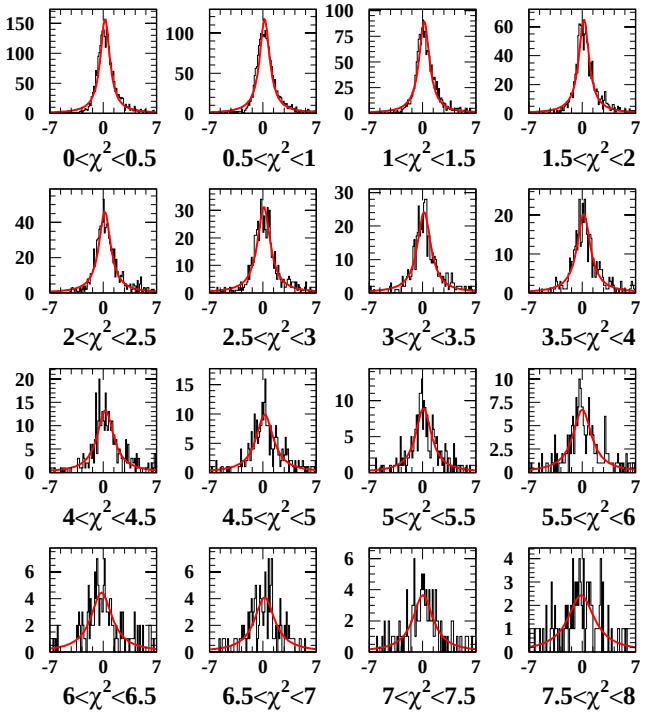

Figure 6.2: KORALW $q\bar{q}e\nu$ event pull distributions for the 2C kinematic fit in slices of the fit χ^2. A simple Breit Wigner is fitted to these distributions.

There are more kinematic fits with large χ^2 values than one would expect, and it is sensible to check if these fits have accurate errors. This can be done by looking at the pull width as a function of the χ^2 of the fit. Figure 6.2 shows the KORALW $q\bar{q}e\nu$ 2C kinematic fit pull distributions in slices of the kinematic fit χ^2. A Breit Wigner is

fitted to each of these pull distribution plots. In figure 6.3a the width of these Breit Wigners is plotted against the χ^2 slice. The width of the pull distributions increases as the χ^2 increases. This means that kinematic fits with large χ^2 are underestimating the error. To correct for this the error is multiplied by $\sqrt{\chi^2/ndf}$ if the $\chi^2 > ndf$ (where ndf is the number of degrees of freedom). Figure 6.3b shows the pull width as a function of χ^2 after this correction, the pull width is now much less dependent on the χ^2.

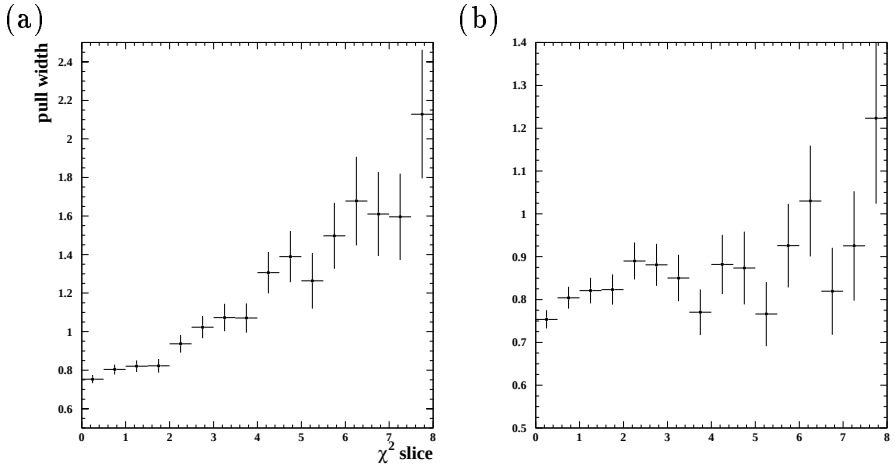

Figure 6.3: a) The width of the Breit Wigners fitted to the pull distributions in figure 6.2 as a function of the χ^2 slice. b) The pull width after the error has been multiplied by $\sqrt{\chi^2/ndf}$ for fits where $\chi^2 > ndf$.

Figure 5.9 shows the resolution of the kinematic fit for KORALW $q\bar{q}e\nu$ events in slices of the kinematic fit errors. In figure 6.4 the width of the Breit Wigners fitted to these resolution functions is plotted against the kinematic fit error slice. The resolution width should be proportional to the kinematic fit error. This is approximately the case and the constant of proportionality is approximately 0.6. The resolution width σ_R is approximately equal to 0.6 times the kinematic fit error for the $q\bar{q}e\nu$ channel.

This approximation is used for $q\bar{q}\mu\nu$ and $q\bar{q}\tau\nu$ channels also. The resolution in the $q\bar{q}q\bar{q}$ channel is well approximated by 1.0 times the kinematic fit error. Figure 6.5 shows the resolution width as a function of the 'adjusted' error for all the channels.

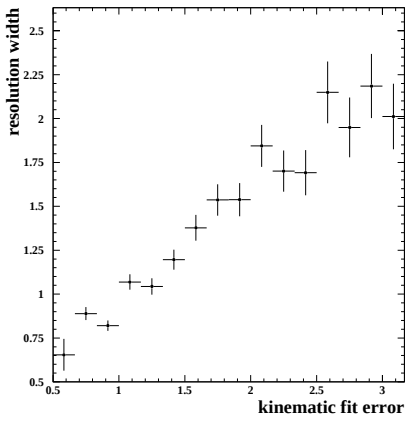

Figure 6.4: The width of the Breit Wigners fitted to the resolution distributions in slices of the kinematic fit error for KORALW $q\bar{q}e\nu$ events. Only part of the resolution function for the fits with errors between 0.5 and 0.66 GeV was fitted, see figure 5.9.

6.2.3 Estimating f_b, f_w and p_s

The output value of the $W^+W^- \rightarrow q\bar{q}q\bar{q}$ relative likelihood selection is used as an estimate of p_s, the probability that the event is a signal event. This selection was designed with this purpose in mind, figure 4.3 shows the relative likelihood value. The value of the $W^+W^- \rightarrow q\bar{q}l\nu$ relative likelihood is shown in figure 4.6. Since a high purity can be achieved in the $q\bar{q}l\nu$ channels by placing a cut on the relative likelihood value the PTC method is not used to form an uncorrelated set of variables. A consequence of this is that the likelihood is strongly peaked at zero and one, and since the correlations between the variables have not been accounted for it is not wise

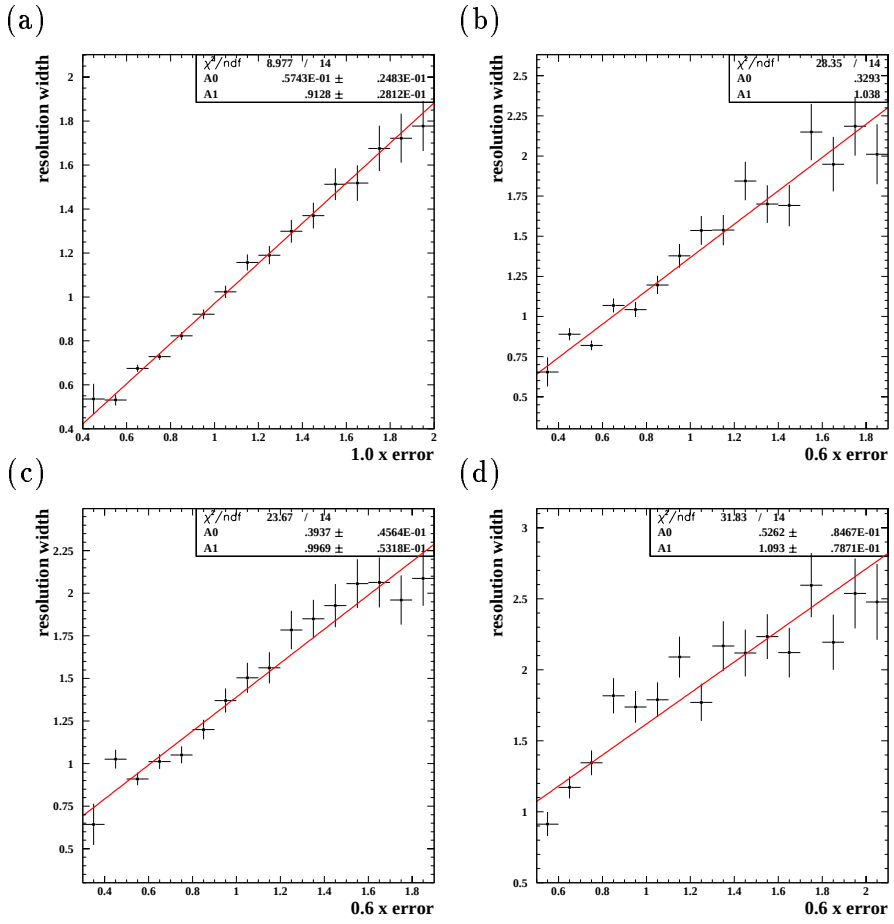

Figure 6.5: The width of the resolution functions in slices of the adjusted fit error. a) The $q\bar{q}q\bar{q}$ channel. b) The $q\bar{q}e\nu$ channel. c) The $q\bar{q}\mu\nu$ channel. d) The $q\bar{q}\tau\nu$ channel.

to interpret the resulting likelihood value as the probability that the event is signal. For all the events that pass the $W^+W^- \rightarrow q\bar{q}l\nu$ selection (i.e. have the a relative likelihood value greater than 0.5) the value of p_s is set to one.

An estimate for the background and wrong jet combination pdfs, f_b and f_w, can be taken from the MC. They should be independent of M_W . These pdfs are not rapidly changing in the region of interest around 80 GeV, and it is found that approximating these pdfs by uniform flat distributions is just as effective as using the pdfs from the MC.

6.2.4 The actual event likelihoods

Once the above approximations are made the event likelihood for $W^+W^- \rightarrow q\bar{q}l\nu$ events becomes

$$\mathcal{L}(m_W \mid m_f) = f_s(m_W \mid m_f) \tag{6.16}$$

and the event likelihood for $W^+W^- \rightarrow q\bar{q}q\bar{q}$ events becomes

$$\mathcal{L}(m_W \mid m_f) = p_s \sum_{i=1}^{i\leq 3} p_i f_s(m_W \mid m_f^i)/E_{beam} + (1-p_s)/E_{beam} \tag{6.17}$$

The beam energy (E_{beam}) is the appropriate normalisation for the uniform pdfs. These are the actual expressions for the event likelihoods that are used in the analysis.

Figure 6.6 shows the event likelihoods for the first $W^+W^- \rightarrow q\bar{q}l\nu$ and $W^+W^- \rightarrow q\bar{q}q\bar{q}$ event candidates found in the data sample, they are fairly typical. The $W^+W^- \rightarrow q\bar{q}l\nu$ event candidate is selected as a $q\bar{q}e\nu$ candidate and the fitted mass is 79.4 $\pm$ 0.8 GeV. The $W^+W^- \rightarrow q\bar{q}q\bar{q}$ candidate has p_s (the probability that it is a signal event) equal to 0.79. The fit for one combination in the $q\bar{q}q\bar{q}$ event has a fit probability much less than 0.1 % and so is thrown away. Another combination has an average mass of 50.5 $\pm$ 1.1 GeV, but the mass difference is 16.9 $\pm$ 3.7 GeV and so the probability of it being the right combination is very small. The contribution of

this combination can only just be seen. The third combination has an average mass of 81.9 $\pm$ 1.0 GeV and a large probability of being the correct combination.

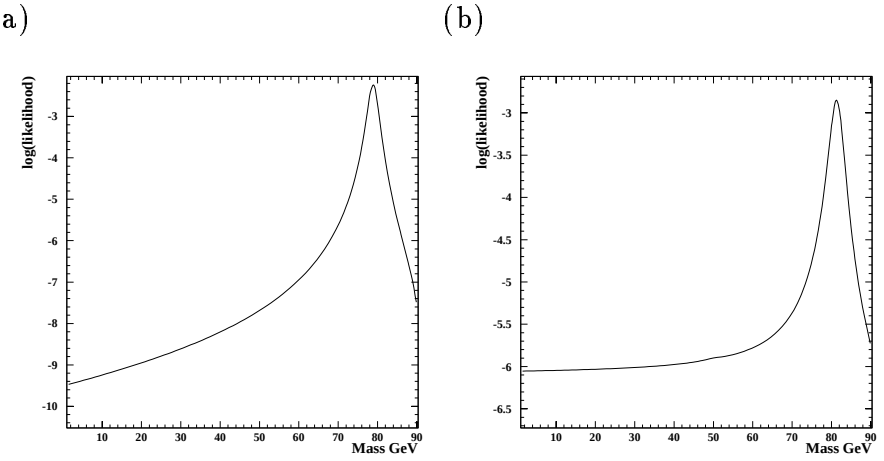

Figure 6.6: The log(likelihood) curve for the first event selected in the data sample as a) a $W^+W^- \rightarrow q\bar{q}l\nu$ candidate and b) a $W^+W^- \rightarrow q\bar{q}q\bar{q}$ candidate.

6.2.5 Combining the event likelihoods

The total likelihood for the data sample is the product of the event likelihoods. The logarithm of this is needed to find the statistical errors.

$$\log \mathcal{L}_{sample} = \log(\prod \mathcal{L}) = \sum \log \mathcal{L} \tag{6.18}$$

MINUIT [62] is used to find the value of m_W that minimises the -log $\mathcal{L}_{sample}$, this is the value of m_W that makes the sample most likely. This will be referred to as $m_W^{\mathcal{L}}$. The value of m_W that minimises the -log $\mathcal{L}_{sample}$ for the $q\bar{q}q\bar{q}$, $q\bar{q}e\nu$, $q\bar{q}\mu\nu$, and $q\bar{q}\tau\nu$ channels will be called $m_W^{\mathcal{L}}(q)$, $m_W^{\mathcal{L}}(e)$, $m_W^{\mathcal{L}}(\mu)$, and $m_W^{\mathcal{L}}(\tau)$ respectively.

The values of m_W where the -log $\mathcal{L}_{sample}$ is 0.5 units above the minimum give the upper and lower one standard deviation limits. The -log $\mathcal{L}_{sample}$ for all the channels

is, to a very good approximation, parabolic around the minimum and the upper and lower error limits are symmetric. The one standard deviation error on $m_W^{\mathcal{L}}$ will be referred to as $\sigma^{\mathcal{L}}$. Figure 6.7 shows the -log $\mathcal{L}_{sample}$ from the data sample for all the channels.

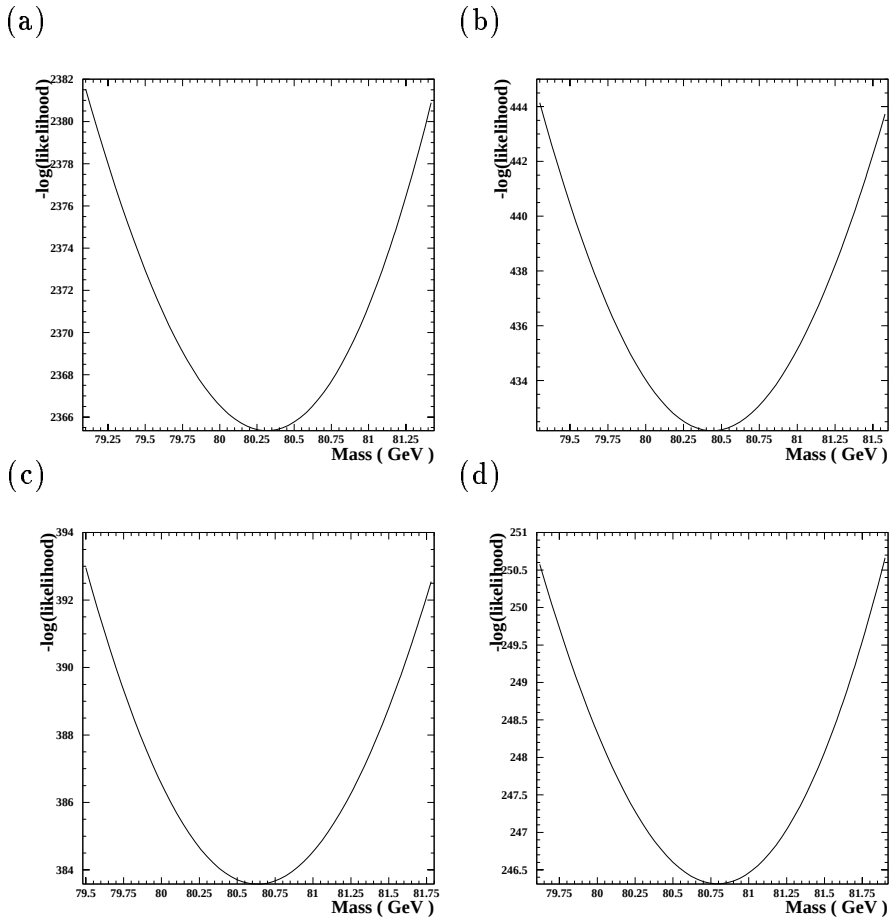

Figure 6.7: The -log $\mathcal{L}_{sample}$ from the data sample for the four channels. a) The $q\bar{q}q\bar{q}$ channel. b) The $q\bar{q}e\nu$ channel. c) The $q\bar{q}\mu\nu$ channel. d) The $q\bar{q}\tau\nu$ channel.

6.3 Bias

The value of $m_W^{\mathcal{L}}$ from the minimum of the -log $\mathcal{L}_{sample}$ will not be an unbiased estimate of M_{W} the true W boson mass. The value of $m_W^{\mathcal{L}}$ in MC subsamples is used to estimate the bias in the data sample. There are several causes of this bias.

6.3.1 Causes of bias

Initial State Radiation

The kinematic fit uses energy and momentum conservation to improve the mass resolution. Unfortunately it does not take into account ISR, this has the effect of increasing the fitted mass and hence the value of $m_W^{\mathcal{L}}$. This is one of the most important causes of bias in $m_W^{\mathcal{L}}$. KORALW should simulate ISR accurately and so can be used to estimate this bias.

Phase space

The W mass production spectrum is distorted from a Breit Wigner by the phase space. This reduces the probability of producing a W boson with mass close to the beam energy. This is approximated by the PS term in the event likelihood which hopefully reduces the bias on $m_W^{\mathcal{L}}$ due to phase space effects.

The kinematic fit errors are also effected by phase space; they are under estimated for those fits with a fitted mass close to the beam energy. The effects of this are minimised by requiring the fit error to be larger than some value, nominally 0.5 GeV. The MCs used should simulate the phase space effects accurately and so the remaining bias due to the phase space can be estimated.

Detector effects

The tracks and jets in an event will not be reconstructed perfectly. The track momenta, the ECAL cluster energies, and the HCAL cluster energies are combined attempting to avoid double counting by assigning tracks to clusters [1]. Even so the jet energy may be biased. The detector simulation program GOPAL has been carefully calibrated using millions of Z events and should reproduce the detector effects well.

Reconstruction method

The exact method used to form $m_W^{\mathcal{L}}$ will affect the bias. Different resolution functions, different functions for the underlying mass spectra and different approximations for f_b, f_w and p_s would all alter the value of $m_W^{\mathcal{L}}$. Some choices are much better than others, the functions used in this analysis are the ones that reduce the error on the measured mass. As the same method is used in the MC and the data the exact details of the method will not cause a problem for the bias estimation.

Interconnection effects

There are several ways that the two Ws in an event can interact before decaying, these are discussed in section 2.5.4. These can affect value of $m_W^{\mathcal{L}}$. The most troublesome of these are the ones that are difficult to predict and model. The two most important are Bose-Einstein correlations and colour reconnection, which only affect the $q\bar{q}q\bar{q}$ channel. These two effects are not included in KORALW the default MC.

Various models have been suggested and incorporated into MC programs. The different models predict different, sometimes large, shifts in $m_W^{\mathcal{L}}$. At present most of the different models can not be ruled out and a large potential systematic error must be assigned to these effects.

[1] The GCE [63] energy calibration scheme is used to do this.

6.3.2 Bias correction

Data sized MC subsamples are used to estimate the bias on $m_W^{\mathcal{L}}$ in the data. These MC subsamples must contain all the different types of event that are expected in the data sample. Tables 6.1 and 6.2 show the expected number of events passing the $W^+W^- \to q\bar{q}q\bar{q}$ preselection and the $W^+W^- \to q\bar{q}l\nu$ selection. The exact number of each type of event in each subsample is a random integer generated from a Poisson distribution whose mean is the expected number.

Each of the subsamples used in the bias correction have totally independent signal events (i.e. each MC signal event is used in only one subsample). The luminosity of the background MC samples is lower than the signal MC luminosity so the background events are used in more than one subsample, but the number of background events in the subsamples is small so the subsamples are treated as being totally independent.

Source	Expected number of events passing the $W^+W^- \to q\bar{q}l\nu$ selection
$W^+W^- \to q\bar{q}l\nu$	333.8 $\pm$ 2.1
$W^+W^- \to q\bar{q}q\bar{q}$	3.9 $\pm$ 0.1
$Z^0/\gamma \to q\bar{q}$	13.0 $\pm$ 0.4
$q\bar{q}l^+l^-$	9.7 $\pm$ 0.2
Total expected	360.4 $\pm$ 2.1
183 GeV data	361

Table 6.1: The expected and actual number of events in the data sample passing the $W^+W^- \to q\bar{q}l\nu$ selection. Sources of background with less than one event expected are ignored. Only the statistical errors are shown.

The MC subsamples are then analysised in exactly the same way as the data

Source	Expected number of events passing the $W^+W^- \to q\bar{q}q\bar{q}$ preselection
$W^+W^- \to q\bar{q}q\bar{q}$	361.9 $\pm$ 2.3
$W^+W^- \to q\bar{q}l\nu$	19.8 $\pm$ 0.4
$Z^0/\gamma \to q\bar{q}$	140.5 $\pm$ 1.3
$ZZ \to q\bar{q}q\bar{q}$	13.2 $\pm$ 0.2
Total expected	535.4 $\pm$ 2.7
183 GeV data	541

Table 6.2: The expected and actual number of events in the data sample passing the $W^+W^- \to q\bar{q}q\bar{q}$ preselection. Sources of background with less than one event expected are ignored. Only the statistical errors are shown.

sample. A value of $m_W^{\mathcal{L}}$ and its associated $\sigma^{\mathcal{L}}$ are extracted from the -log $\mathcal{L}_{sample}$ for each subsample. Since the true value of $M_{\rm W}$ that was used to generate the signal events in the subsamples is known the bias for each subsample can be found.

$$bias = m_W^{\mathcal{L}} - M^{true} \tag{6.19}$$

Figure 6.8 shows $m_W^{\mathcal{L}}(e)$ for 100 MC subsamples generated with $M_{\rm W}$ =80.33 GeV and $\sqrt{s}$=183 GeV. The mean $m_W^{\mathcal{L}}$ in these subsamples is 80.62 $\pm$ 0.03 GeV. So the mean bias in these subsamples is 290 $\pm$ 30 MeV.

The bias may depend on the value of $M_{\rm W}$ (for instance the bias due to ISR should decrease if the value of $M_{\rm W}$ increases). The exact value of $M_{\rm W}$ in the data is unknown so the mean bias in MC subsamples generated with different values of $M_{\rm W}$ is found. Figure 6.9 shows these mean biases for the four channels. The mean bias decreases as the value of $M_{\rm W}$ increases. A straight line is fitted to these mean biases and is used to estimate the bias in the data. If the slope and intercept of this

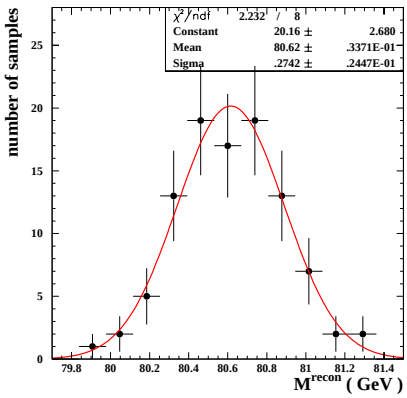

Figure 6.8: $m_W^{\mathcal{L}}$ in the $q\bar{q}e\nu$ channel for 100 KORALW subsamples generated with M_W =80.33 GeV and $\sqrt{s}$=183 GeV.

line are S_{mw} and C then the equation of the line is

$$bias = S_{mw}(M^{true} - 80.33) + C \tag{6.20}$$

$(M^{true} - 80.33)$ GeV is used so that C is the bias estimate for a data sample with M^{true} equal to 80.33 GeV.

The bias may depend on the value of $\sqrt{s}$ as well. Figure 6.10 shows the mean biases in MC subsamples generated with three different $\sqrt{s}$. A straight line is fitted to these mean biases and the slope (S_{eb}) is used to make a small correction to M^{true} due to the fact that the data were recorded at a beam energy 0.15 GeV lower than the different M_W MC samples. The MC samples were generated before the exact LEP beam energy was known. Given the measured $m_W^{\mathcal{L}}$ in the data sample the best estimate of M_W (M^{est}) should be

$$M^{est} = \frac{m_W^{\mathcal{L}} + 80.33 S_{mw} - C}{1 + S_{mw}} + 0.15 S_{eb} \tag{6.21}$$

The fitted values for S_{mw}, C, and S_{eb} are shown in table 6.3.

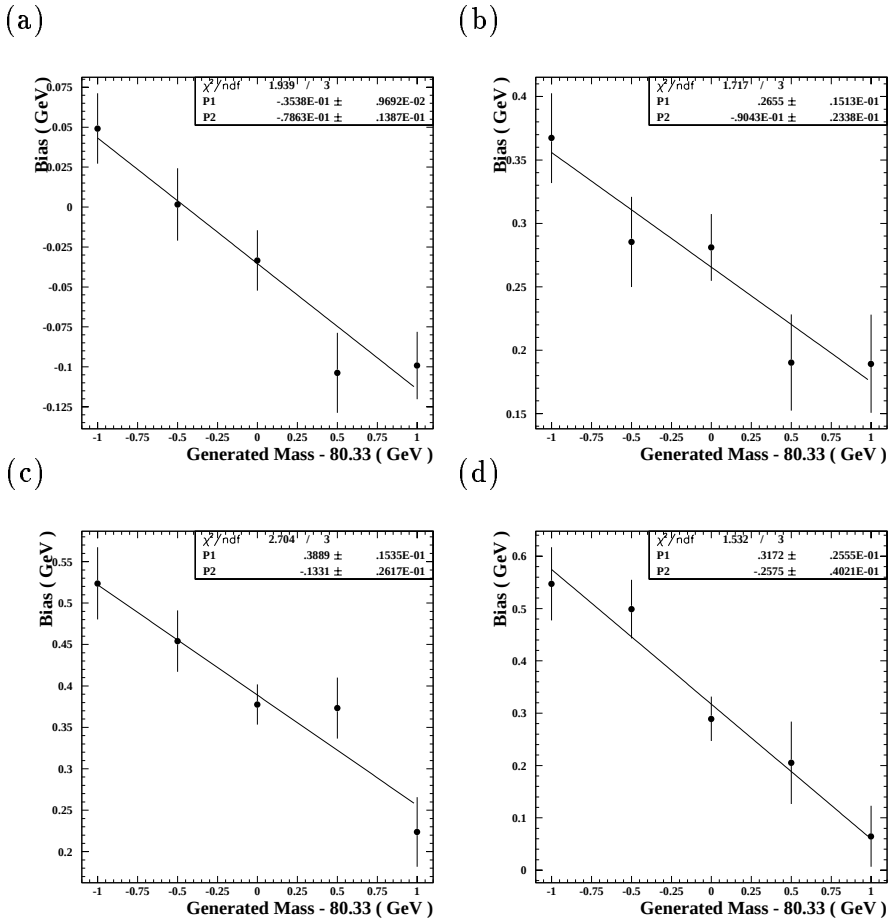

Figure 6.9: The mean bias in subsamples generated with five different M_{W} values. a) The $\mathrm{q\bar{q}q\bar{q}}$ channel. b) The $\mathrm{q\bar{q}}e\nu$ channel. c) The $\mathrm{q\bar{q}}\mu\nu$ channel. d) The $\mathrm{q\bar{q}}\tau\nu$ channel.

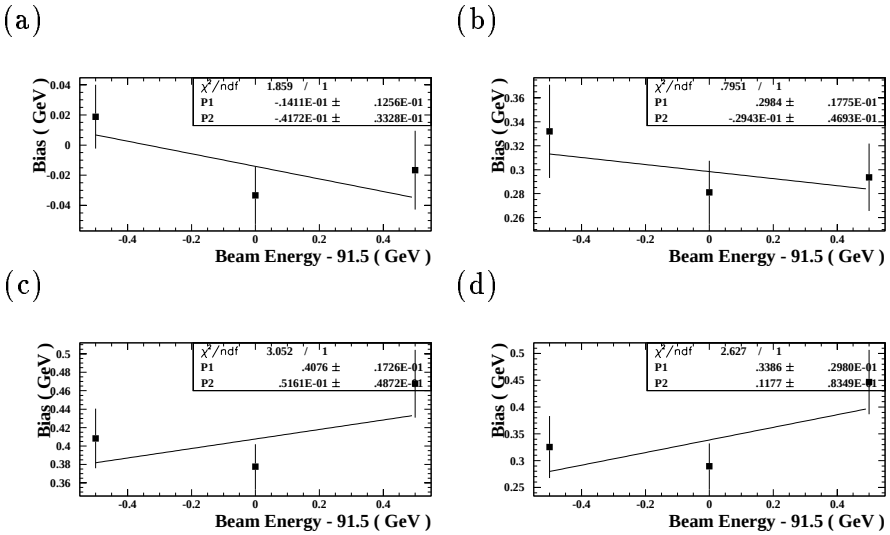

Figure 6.10: The mean bias in subsamples generated with three different E_{beam} values. a) The $q\bar{q}q\bar{q}$ channel. b) The $q\bar{q}e\nu$ channel. c) The $q\bar{q}\mu\nu$ channel. d) The $q\bar{q}\tau\nu$ channel.

channel	S_{mw}	C (GeV)	S_{eb}
$q\bar{q}q\bar{q}$	-0.079±0.014	-0.036±0.010	-0.042±0.033
$q\bar{q}e\nu$	-0.090±0.023	0.265±0.015	-0.029±0.047
$q\bar{q}\mu\nu$	-0.133±0.026	0.389±0.015	0.052±0.049
$q\bar{q}\tau\nu$	-0.258±0.040	0.317±0.026	0.118±0.083
$q\bar{q}l\nu$	-0.121±0.017	0.327±0.010	0.040±0.033

Table 6.3: The fitted bias parameters.

6.4 Statistical error calibration

The relationship between $\sigma^{\mathcal{L}}$ and σ^{est}, the error on M^{est} is given by differentiating equation 6.21.

$$\sigma^{est} = \frac{\sigma^{\mathcal{L}}}{1 + S_{mw}} \tag{6.22}$$

The sensitivity ($1 + S_{mw}$) of the method is less than one so σ^{est} will be larger than $\sigma^{\mathcal{L}}$.

Because the expressions for the event likelihoods (equations 6.16 and 6.17) are only approximations, the error extracted from them ($\sigma^{\mathcal{L}}$) will only be an approximation and so σ^{est} will also only be an approximation of the error on M^{est}. The MC subsamples can be used to check how good this approximation is and to correct it. The pull distribution

$$pull = \frac{M^{est} - M^{true}}{\sigma^{est}} \tag{6.23}$$

is used to do this. The pull distribution should be a Gaussian. Since the bias correction has been applied the mean of this pull distribution should be very close to zero. The width of the pull distribution should be one, but as σ^{est} is only an approximation the width may be slightly above or below one. The width of this pull distribution times σ^{est} will be a better approximation of the error on M^{est} .

The subsamples used for the bias correction are essentially independent of each other. The limited MC statistics mean that only about 100 subsamples can be formed from the KORALW sample with M_{W} =80.33 GeV and E_{beam}=91.5 GeV. The statistical error on the pull distribution width could be reduced if more subsamples were available. There are two ways to get more subsamples: generate more MC, or use the MC more efficiently. Generating lots of fully GOPALised MC is very computer intensive so the second approach is preferred. The bootstrap [64] is a method for doing this. The events for each subsample are selected at random, with replacement,

from the large MC samples. Any number of subsamples can be generated this way. Each event may be used more than once but the chance of having subsamples with all the same events is negligible. So long as the number of subsamples is not excessive the width of pull distribution can be calculated as if the subsamples were totally independent. It is found that using each event three times on average is acceptable. In this way 1200 subsamples were formed from the seven KORALW MC samples with different M_{W} and E_{beam} values. The pull distributions for these subsamples are shown in figure 6.11. The rms pull widths and rms M^{est} width obtained from these samples are listed in table 6.4

channel	rms pull width	rms M^{est} width (MeV)
$q\bar{q}q\bar{q}$	0.99±0.02	192±5
$q\bar{q}e\nu$	1.06±0.02	293±9
$q\bar{q}\mu\nu$	1.06±0.02	326±13
$q\bar{q}\tau\nu$	1.14±0.02	594±34

Table 6.4: The rms width of the pull distribution and the rms width of the M^{est} distribution for 1200 MC subsamples.

6.5 Systematics

Many assumptions and approximations have been made in this analysis. The validity of these assumptions and the effect on the measured M_{W} of the approximations must be checked. Any discrepancies should be assigned a systematic error. The various expected sources of systematic error are outlined below and the values associated to them are shown in table 6.14. The three $q\bar{q}l\nu$ channels are grouped together for these

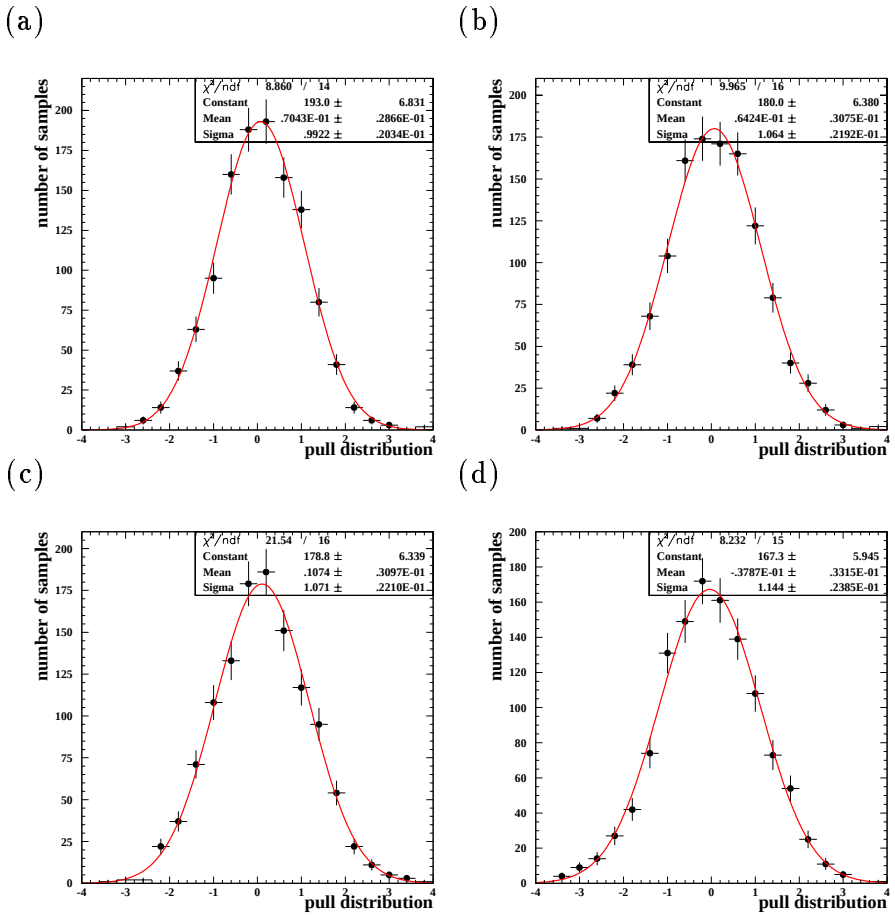

Figure 6.11: The pull distributions for M^{est}. a) The $q\bar{q}q\bar{q}$ channel. b) The $q\bar{q}e\nu$ channel. c) The $q\bar{q}\mu\nu$ channel. d) The $q\bar{q}\tau\nu$ channel.

systematic studies.

6.5.1 The LEP beam energy uncertainty

The LEP beam energy is used as an absolute energy scale by the kinematic fit. The luminosity weighted beam energy has been accurately measured by the LEP Energy Working Group to be 91.350±0.025 GeV [6]. The effect the uncertainty on the beam energy has on the measured M_{W} is found by altering the beam energy used by the kinematic fit and the bias correction by ±25 MeV. The shift in M^{est} from the data sample is used as the systematic error due to the beam energy uncertainty.

6.5.2 Initial State Radiation mis-modelling

Since the effects of ISR are not included in the kinematic fit the fitted mass is over estimated. This is one of the major sources of bias in $m_W^{\mathcal{L}}$. This bias is estimated using MC which has $\mathcal{O}(\alpha^2)$ treatment of ISR. The effect of the exclusion of high order terms, and any other approximations, is estimated as the difference in the mean $m_W^{\mathcal{L}}$ in subsamples generated with $\mathcal{O}(\alpha^2)$ treatment of ISR and the mean $m_W^{\mathcal{L}}$ in subsamples generated with $\mathcal{O}(\alpha)$ treatment of ISR. MC run 7667 which contains 50,000 fully GOPALised KORALW $\mathrm{W^+W^-}$events generated with $\mathcal{O}(\alpha)$ treatment of ISR is used for this comparison.

6.5.3 Hadronisation mis-modelling

The quark hadronisation in all the default MC samples is modelled by JETSET. The non-perturbative phase of the fragmentation in JETSET is governed by various parameters, which were tuned to agree with LEP I data. The finite data statistics mean these parameters have uncertainties associated with them [65]. PYTHIA

$W^+W^- \rightarrow q\bar{q}q\bar{q}$ events were generated with parameters σ_q, b, Λ, and Q_0 [2] varied by one standard deviation about their tuned values. The fast smear mode of the detector simulation was used on these events and then the event selection and kinematic fits were performed as normal. The mean values of $m_W^{\mathcal{L}}$ in the subsamples formed from these events are shown in table 6.5.

As a cross check two MC samples which have the same 4-vectors generated by PYTHIA but which use different models to perform the hadronisation are compared. The two hadronisation models used are JETSET which uses the LUND string model and HERWIG which uses a QCD cluster model. The MC samples used are listed in table 6.6. The shift in $m_W^{\mathcal{L}}$ due to changing models for each subsample is found, for the $q\bar{q}q\bar{q}$ channel the average shift is 45 ± 21 MeV and the average shift for the $q\bar{q}l\nu$ channels is 55 ± 14 MeV. These shifts are larger than the shifts found by changing the fragmentation parameters in PYTHIA $W^+W^- \rightarrow q\bar{q}q\bar{q}$ events, so they are taken as the systematic uncertainty due to mis-modelling of the hadronisation.

6.5.4 Four fermion interference

The bias on $m_W^{\mathcal{L}}$ is estimated using signal MCs which only contain the three W^+W^- production processes (via Z production, γ production and ν exchange) shown in figure 2.4. There are other diagrams which can produce $q\bar{q}q\bar{q}$ and $q\bar{q}l\nu$ final states, these will interfere slightly with the signal diagrams and may alter the bias on $m_W^{\mathcal{L}}$. In order to estimate the size of this effect, the mean $m_W^{\mathcal{L}}$ in subsamples formed from grc4f and EXCALIBUR MC samples listed in table 6.7, which contain the full set of four fermion diagrams, were found. The largest of the differences from the normal

[2] In the software [40] these are called PARJ(21), the width of the transverse momentum distribution for the primary hadrons, PARJ(42), a parameter of the symmetric LUND fragmentation function, PARJ(81), the Λ value in running α_s, and PARJ(82), the invariant mass cut off for parton showers.

parameter values		$m_W^{\mathcal{L}}$ - $m_W^{\mathcal{L}}$ (default) (MeV)
σ_q	PARJ(21)=0.37	27±24
	PARJ(21)=0.43	6±24
b	PARJ(42)=0.48	9±24
	PARJ(42)=0.56	18±26
Λ	PARJ(81)=0.244	9±25
	PARJ(81)=0.256	20±25
Q_0	PARJ(82)=1.4	17±24
	PARJ(82)=2.4	22±25

Table 6.5: The mean value of $m_W^{\mathcal{L}}$ for subsamples formed from smear mode PYTHIA events with different fragmentation parameter values. The parameter values shown are $\pm$ 1σ from the default values.

channel	model	MC run number	$m_W^{\mathcal{L}}$ - M^{true} (MeV)
$q\bar{q}q\bar{q}$	JETSET	6860	-28±18
	HERWIG	6861	17±16
$q\bar{q}e\nu$	JETSET	6862	266±20
	HERWIG	6863	305±21
$q\bar{q}\mu\nu$	JETSET	6865	370±22
	HERWIG	6866	441±23

Table 6.6: The MC sample pairs with the same 4 vectors but different hadronisation models and the bias found in their subsamples.

KORALW value is used as the systematic error due to neglecting four fermion interference.

MC samples	$m_W^{\mathcal{L}}$ - M^{true}	
	$q\bar{q}q\bar{q}$ (MeV)	$q\bar{q}l\nu$ (MeV)
KORALW runs 7323-7329	-36±10	327±10
grc4f runs 7050 and 7051	-1±28	342±25
EXCALIBUR run 7330	32±21	343±25

Table 6.7: The bias in the default KORALW subsamples and subsamples with four fermion interference.

6.5.5 Detector mis-modelling

The simulation of the OPAL detector (GOPAL) has been tuned to match the data taken in at $\sqrt{s}=M_Z$, but there may still be differences between the jet/lepton 4-momenta and their errors in the data and the MC. The 2.1 pb^{-1} of data taken at $\sqrt{s}=M_Z$ at the start of the 1997 run is used to check for any discrepancy [69] [56] [57].

In order to estimate the systematic uncertainty this detector mis-modelling may cause, the jet/lepton 4-momenta in the default MC (run 7323) and their estimated errors are adjusted to correct for the differences or possible differences found, and the kinematic fits repeated. The changes made to the jet/lepton 4-momenta are shown in tables 6.8 and 6.9. The mean shift in $m_W^{\mathcal{L}}$ for each subsample is used as the systematic error due to detector mis-modelling.

It is suspected that the HCAL modelling may not be as accurate as the rest of the detector simulation. So the HCAL information was removed from the jet finding and

angular range	applied correction			
	E	σ_E	σ_θ	σ_ϕ
$0 < \cos\theta \leq 0.4$	0.98	0.98	1.06	1.01
$0.4 < \cos\theta \leq 0.7$	1.00	1.03	1.07	1.01
$0.7 < \cos\theta \leq 0.82$	1.00	1.02	1.09	1.03
$0.82 < \cos\theta \leq 0.92$	1.02	1.18	1.12	1.03
$0.92 < \cos\theta \leq 1.0$	1.05	1.27	1.08	1.05

Table 6.8: The corrections to the jet 4-momenta due to possible detector mis-modelling.

parameter	applied correction
E	± 1 %
$\sigma_E(e)$	± 20 %
$\sigma_E(\mu)$	± 15 %
σ_θ	± 40 %
σ_ϕ	± 30 %

Table 6.9: The corrections to the lepton 4-momenta due to possible detector mis-modelling.

the analysis repeated (i.e. the bias in HCAL-less MC subsamples is found and the $m_W^{\mathcal{L}}$ in the HCAL-less data sample is found). Since removing the HCAL information changes the jet 4-momenta, events which previously passed the selection may fail and events which previously failed may be selected. Also kinematic fits which previously worked may fail. So the events and combinations used in the data sample will be different, so one should not expect the measured mass to be identical.

The difference in the measured value of M_{W} between KORALW $\mathrm{q\overline{q}q\overline{q}}$ ($\mathrm{q\overline{q}}l\nu$) subsamples with and without the HCAL information is found, the mean of this difference is compatible with zero, and the rms width of this difference is 118 (128) MeV. The difference in the measured value of M_{W} in the data sample with and without the HCAL information is 96 (62) MeV. There is no evidence to suggest that there is a systematic effect due to the mis-modelling of the HCAL, and no addition systematic error is included.

6.5.6 Background mis-modelling

The accepted background cross section estimates were varied by amounts based on the uncertainties evaluated in [66]. The $\mathrm{Z}^0/\gamma \rightarrow \mathrm{q\overline{q}}$ background was varied by ± 20 %, and the four fermion backgrounds were varied by ± 50 %. Also HERWIG was used instead of PYTHIA for the $\mathrm{Z}^0/\gamma \rightarrow \mathrm{q\overline{q}}$ background. The shift in $m_W^{\mathcal{L}}$ for each subsample after these changes was found. The quadrature sum of these mean shifts is used as the systematic error due to background mis-modelling. The MCs used for four fermions backgrounds (and signal) are changed in the assessment of the systematic error due to the neglecting four fermion interference.

6.5.7 Monte Carlo statistics

The finite MC statistics mean that the estimated bias will have a statistical error. The bias parameters and their statistical errors are shown in table 6.3, the total statistical error on the estimated bias in the data sample is calculated and included in the list of systematic errors.

6.5.8 Bose-Einstein correlations

Section 2.5.6 discusses the effect Bose-Einstein correlations (BEC) between two hadronically decaying Ws may have on the measured M_{W} in the $\mathrm{W^+W^-} \rightarrow \mathrm{q\overline{q}q\overline{q}}$ channel. PYTHIA $\mathrm{W^+W^-} \rightarrow \mathrm{q\overline{q}q\overline{q}}$ samples have been generated which include BEC between both Ws (MC run 7626). The difference between the mean value of $m_W^{\mathcal{L}}$ from subsamples formed from this MC and the mean value of $m_W^{\mathcal{L}}$ from subsamples formed using PYTHIA without BEC (run 6900) was 18$\pm$32 MeV, this was used as the systematic error due to BEC.

6.5.9 Colour reconnection

Section 2.5.5 discusses the effect colour reconnection may have on the measured M_{W} in the $\mathrm{W^+W^-} \rightarrow \mathrm{q\overline{q}q\overline{q}}$ channel. The MC programs PYTHIA and ARIADNE have been adapted to simulate the effects of colour reconnection; both have various different models available [23]. The difference in the mean $m_W^{\mathcal{L}}$ from subsamples generated using these MCs and from appropriate subsamples without colour reconnection are shown in table 6.10. Comparisons with the data disfavour the ARIADNE model 3 and so this model is excluded [72]. The largest shift for models compatible with the data (61$\pm$23 MeV) is taken as the systematic error due to colour reconnection.

MC generator	model	MC run number	shift in $m_W^{\mathcal{L}}$
PYTHIA	SK I	7851	30±26
	SK II	7852	8±24
	SK II′	7853	8±23
ARIADNE	model 2	8103	61±23
	model 3	8104	142±23

Table 6.10: The shift in $m_W^{\mathcal{L}}$ due to various colour reconnection models.

6.5.10 Fit procedure

In order to assess the systematic error due to the fit procedure, various aspects of the method are changed. If the change in the measured M_{W} is statistically significant it is included as a systematic error. Some of the changes are not expected to produce significant change in the measured M_{W} and are included to check for unexpected systematic errors.

Using reweighted subsamples to estimate the bias

The bias as a function of M_{W} (and the sensitivity) is found by using MC samples generated with five different M_{W} values, this is discussed in section 6.3.2. An alternative approach would be to reweight one MC sample to make it appear as if it was generated with many different M_{W} values and hence find the bias as a function of M_{W} . Section 5.3.2 discusses reweighting. Figure 6.12 shows the bias using this reweighting method. The estimated bias in the data samples using the reweighted subsamples is 5 MeV different from the normal estimate for the $\mathrm{q\bar{q}q\bar{q}}$ channel and 9 MeV different for the $\mathrm{q\bar{q}}l\nu$ channels. These changes in predicted bias are not statistically significant and no additional systematic error is included.

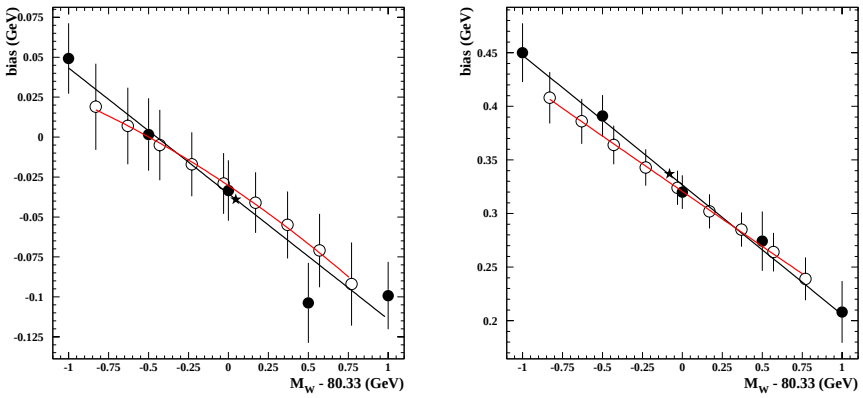

Figure 6.12: The filled circles are the bias in KORALW subsamples generated at various M_{W} values, the straight (black) line fitted to these points is used to estimate the bias in the data sample and the sensitivity. The open circles are the bias in reweighted subsamples formed from the central KORALW sample with M_{W} =80.33 GeV, the errors on these open circles are correlated. The star represents the data sample.

Changing the error scaling and the fit cuts

The resolution width used is the kinematic fit error multiplied by 0.6 and 1.0 for the $q\bar{q}l\nu$ and $q\bar{q}q\bar{q}$ channels respectively, this is discussed in section 6.2.2. The amounts used to scale the errors were found by examining the MC resolution versus error plots. As a systematic check the scale factors were varied by ± 0.1 and the analysis repeated.

Only those kinematic fits with errors greater than the values listed in table 5.2 are used. The value of these cuts were found by examining the MC mass verses error plots, as a systematic check they are varied by ± 0.1 GeV and the analysis repeated.

The largest shift in the measured mass from the data sample after these changes is used as the systematic error due to the choice of these parameters. The largest shifts were 21 MeV and 54 MeV for the $q\bar{q}q\bar{q}$ and $q\bar{q}l\nu$ channels respectively.

Using PYTHIA to estimate the bias

Table 6.11 shows all the fully GOPALised PYTHIA W^+W^-samples with different generated M_W and $\sqrt{s}$ values. These samples were used, instead of the KORALW samples, to estimate the bias in the data sample. Table 6.12 shows the bias parameters from these PYTHIA samples. After taking in to account the fact that the different M_W PYTHIA samples were generated at $\sqrt{s}$=184 GeV, the estimated biases were 7 MeV and 12 MeV different from the KORALW estimate for the $q\bar{q}q\bar{q}$ and $q\bar{q}l\nu$ channels respectively. These are not statistically significant and no additional systematic error is included.

Comparison with simple method

The simple method discussed in section 5.1 does not use the kinematic fit or the event likelihoods used in the convolution method. It is interesting to see if the

event type	Monte Carlo sample	generated $\sqrt{s}$	generated M_{W}
$\mathrm{W^+W^-} \rightarrow$ all	PYTHIA run 7323	184 GeV	80.33 GeV
$\mathrm{W^+W^-} \rightarrow$ all	PYTHIA run 7324	183 GeV	80.33 GeV
$\mathrm{W^+W^-} \rightarrow$ all	PYTHIA run 7325	185 GeV	80.33 GeV
$\mathrm{W^+W^-} \rightarrow$ all	PYTHIA run 7326	184 GeV	79.33 GeV
$\mathrm{W^+W^-} \rightarrow$ all	PYTHIA run 7327	184 GeV	79.83 GeV
$\mathrm{W^+W^-} \rightarrow$ all	PYTHIA run 7328	184 GeV	80.83 GeV
$\mathrm{W^+W^-} \rightarrow$ all	PYTHIA run 7329	184 GeV	81.33 GeV

Table 6.11: The PYTHIA $\mathrm{W^+W^-}$Monte Carlo samples used to estimate the bias as a systematic check.

channel	S_{mw}	C (GeV)	S_{eb}
$\mathrm{q\bar{q}q\bar{q}}$	-0.081$\pm$0.017	0.003$\pm$0.011	0.071$\pm$0.036
$\mathrm{q\bar{q}}l\nu$	-0.103$\pm$0.016	0.373$\pm$0.010	0.067$\pm$0.036

Table 6.12: The bias parameters for the PYTHIA samples.

mass measured by this simple method is compatible with the mass measured by the convolution method. Unfortunately, since the simple method is far from optimal, the measured masses can be legitimately different without implying any systematic effect. If one knows the minimum variance bound (called σ_0 here) one can find how big the differences can legitimately be [67]. Two solutions for the maximum difference (σ_Δ) due to statistical fluctuations are found, if the error from one of the methods is equal to the minimum variance bound (i.e. optimal) the two solutions are equal.

$$\sigma_\Delta = \sqrt{(\sigma_1^2 - \sigma_0^2)} \tag{6.24}$$

Here σ_1 is the error from the non-optimal method.

So taking σ_0 to be equal to the statistical error on M_W in the $q\bar{q}q\bar{q}$ channel for the convolution method, which is 212 MeV, and σ_1 to be the statistical error on M_W in the $q\bar{q}q\bar{q}$ channel for the simple method, which is 452 MeV, gives σ_Δ=399 MeV. The actual difference in the measured value of M_W for the two methods is 341 MeV. Both measurements are compatible and no additional systematic error is included.

A simple form of the Breit Wigner fit mass measurement which uses the kinematic fit, described in section 5.3.1, has been performed for the $q\bar{q}l\nu$ channel. Assuming the convolution method to be optimal the maximum difference due to statistical fluctuations is σ_Δ=109 MeV and the actual difference is 55 MeV. Again both measurements are compatible and no additional systematic error is included.

6.5.11 Checking the statistical error

The statistical error σ^{est} is only an approximation since the event likelihoods are only approximations. This means that the MC must be used to correct it by multiplying by the pull width as discussed in section 6.4. As a cross check one can use the method called the 'bootstrap' to check that the statistical error is accurate [64].

Suppose there are n events in the data sample, many 'bootstrap' samples can be formed by selecting n events at random, with replacement, from the data sample. These bootstrap samples should all have different combinations of the data events in them. The value of M^{est} found for each of these bootstrap samples will be different, and their rms width is an estimate of the statistical error on M^{est} .

The estimates of σ^{est} found using 50 bootstrap samples, and the difference between these and the values of σ^{est} from the $\log \mathcal{L}_{sample}$ corrected by the pull width are shown in table 6.13. The difference for both channels combined is consistent with zero although the difference in the $q\bar{q}q\bar{q}$ channel is just under two sigma away from zero.

channel	bootstrap σ^{est} (MeV)	normal σ^{est} (MeV)	difference (MeV)
$q\bar{q}q\bar{q}$	265±27	212±5	53±27
$q\bar{q}l\nu$	181±18	190±5	9±18
combined	149±11	141±3	8±11

Table 6.13: The statistical error on M^{est} from the data sample estimated using the bootstrap method and the normal MC calibrated method.

6.5.12 Combining the systematic errors

The total systematic error for each channel is the quadrature sum of the individual systematic errors shown in table 6.14. Some of these systematic errors have a large statistical component, which means that some are probably over estimated and some under estimated. These over and under estimates should cancel to some extent in the quadrature sum, so these statistical components are ignored.

Whilst combining the measured value of M_{W} for the $q\bar{q}q\bar{q}$ and $q\bar{q}l\nu$ channels the systematic errors are all assumed to be uncorrelated except for the beam energy

uncertainty which is assumed to be fully correlated.

source	$q\bar{q}q\bar{q}$ channel (MeV)	$q\bar{q}l\nu$ channel (MeV)
beam energy	22	20
ISR	47$\pm$28	23$\pm$26
hadronisation	45$\pm$21	55$\pm$14
four fermion	68$\pm$23	49$\pm$28
detector	6$\pm$2	4$\pm$2
background	17$\pm$10	5$\pm$3
MC statistics	12	14
Bose-Einstein	18$\pm$32	n.a.
colour reconnection	61$\pm$23	n.a.
fit procedure	21	54
total	120	98

Table 6.14: A summary of the systematic errors.

Chapter 7

Results

The data taken by the OPAL detector in 1997 at a beam energy of 91.350±0.025 GeV have been used to measure the W boson mass in the $W^+W^- \rightarrow q\bar{q}q\bar{q}$, $W^+W^- \rightarrow q\bar{q}e\nu$, $W^+W^- \rightarrow q\bar{q}\mu\nu$ and $W^+W^- \rightarrow q\bar{q}\tau\nu$ channels using the convolution method.

The measured mass and error for each channel are shown in table 7.1 and figure 7.1. The measured masses for the $q\bar{q}q\bar{q}$ channel and the combined $q\bar{q}l\nu$ channels are

$$\begin{aligned} M_W\ (q\bar{q}q\bar{q}\ ) &= 80.37 \pm 0.21 \pm 0.10 \pm 0.06(BEC/CR) \pm 0.02(E_{beam})\ \text{GeV} \\ M_W\ (q\bar{q}l\nu\ ) &= 80.25 \pm 0.19 \pm 0.10 \pm 0.02(E_{beam})\ \text{GeV} \end{aligned} \tag{7.1}$$

The systematic uncertainty due to Bose-Einstein correlations and colour reconnection effects and the beam energy uncertainty are shown separately. The $q\bar{q}q\bar{q}$ and $q\bar{q}l\nu$ channels when combined give

$$M_W = 80.30 \pm 0.14 \pm 0.08\ \text{GeV} \tag{7.2}$$

where the errors shown are the statistical and total systematic error.

channel	measured M_W (GeV)
$q\bar{q}q\bar{q}$	$80.37 \pm 0.21 \pm 0.12$
$q\bar{q}e\nu$	$80.19 \pm 0.26 \pm 0.10$
$q\bar{q}\mu\nu$	$80.26 \pm 0.32 \pm 0.10$
$q\bar{q}\tau\nu$	$80.57 \pm 0.58 \pm 0.10$

Table 7.1: The measured mass with its statistical and systematic errors for the four channels.

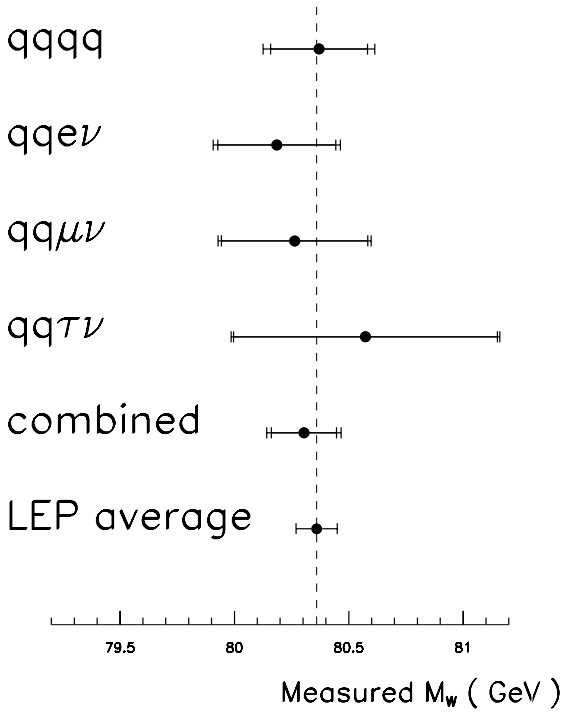

Figure 7.1: The measured mass and errors for the four channels compared to their combination and the LEP average from the 1997 data. The statistical errors are represented by the inner ticks.

Chapter 8

Conclusions

The convolution method has been used to measure the W boson mass using the OPAL detector. The aim of the convolution method was to use as much information as possible from each event (i.e. the kinematic fit errors, all three jet pair combinations and the underlying mass spectrum) and hence reduce the statistical error on the measured M_{W} .

The standard method for measuring M_{W} at OPAL is the reweighting method, this is outlined in section 5.3.2. In the last six months it has been adapted to include some kinematic fit error information [59]. The fits are divided into groups depending on their error and then each group is compared to the reweighted MC spectra. The expected statistical error on M_{W} from the 1997 data using the convolution, reweighting and Breit Wigner fit [69] methods are shown in table 8.1. The expected statistical error for the convolution method is the rms width of the M^{est} distribution for 1200 MC subsamples.

The convolution method has a smaller expected statistical error than the reweighting method for the $\mathrm{q\bar{q}q\bar{q}}$ and $\mathrm{q\bar{q}}e\nu$ channels. The expected error for the $\mathrm{q\bar{q}}\mu\nu$ channel is slightly larger than for the reweighting method. The kinematic fit used for the $\mathrm{q\bar{q}}\tau\nu$ events is different, the convolution method uses a 1C kinematic fit which uses

channel	expected statistical error (MeV)		
	convolution	reweighting	Breit Wigner
$q\bar{q}q\bar{q}$	192±5	200	200
$q\bar{q}e\nu$	293±9	310	300
$q\bar{q}\mu\nu$	327±13	300	330
$q\bar{q}\tau\nu$	594±34	450	560

Table 8.1: The expected error on M_W using the convolution, reweighting and Breit Wigner fit methods. The error on the expected statistical error for the convolution method takes in to account the uncertainty on the sensitivity.

the tau decay products to estimate the direction of the tau, the reweighting method and the Breit Wigner fit method both used this fit as part of the $q\bar{q}\tau\nu$ selection but then used a kinematic fit that ignores the tau decay products to measure the mass. This gives a slightly better resolution but does not explain why the expected statistical error using the convolution method is so much worse than the reweighting method. This is still is not fully understood, but the expected statistical error for the $q\bar{q}\tau\nu$ events using the Breit Wigner fit method is similar to the expected error using the convolution method.

The reweighting method and the convolution method have been compared directly by analysing identical subsamples. The measured mass for each subsample is shown in figure 8.1. In the $q\bar{q}q\bar{q}$ channel the rms width of the measured mass distribution is approximately 10 MeV smaller for the convolution method and in the $q\bar{q}l\nu$ channel the rms width of the measured mass distribution is approximately 10 MeV larger for the convolution method. When all the channels are combined the convolution method and the reweighting method both have approximately the same rms width.

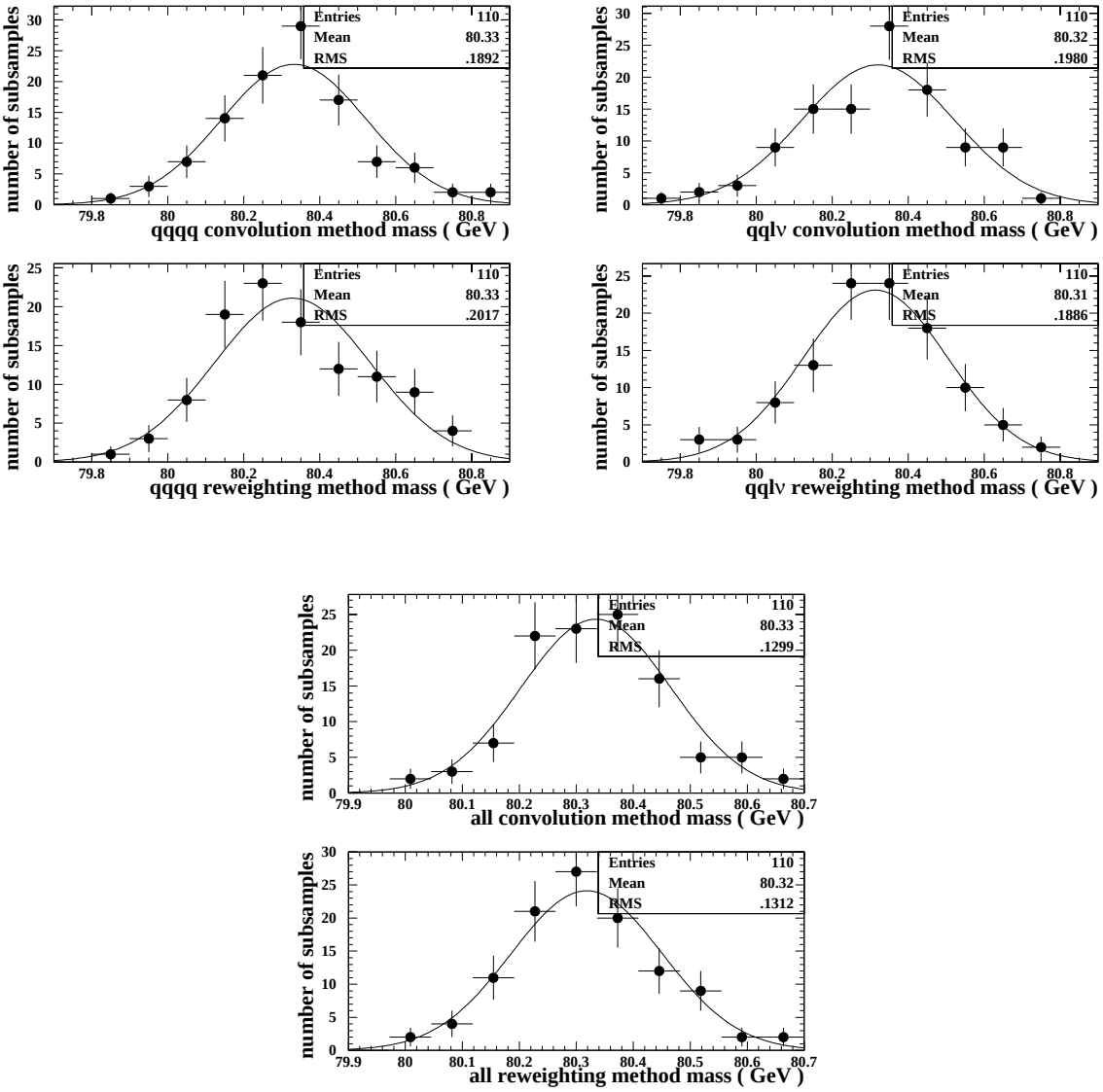

Figure 8.1: The measured mass from the convolution and reweighting methods in the same 110 MC subsamples. The mass for $q\bar{q}q\bar{q}$ channel, the $q\bar{q}l\nu$ channel, and both channels combined are shown.

This convolution analysis has been published as an OPAL technical note [70] and by the OPAL collaboration as a cross check in its $\sqrt{s}$ = 183 GeV W mass paper [59]. The measured value of M_{W} from the convolution method and the reweighting method are compatible. The convolution method has been shown to work effectively and to reduce the statistical error in the $\mathrm{q\bar{q}q\bar{q}}$ channel. This is due to its ability to treat all the jet pair combinations effectively.

The results from the four LEP experiments, and the $p\bar{p}$ collider experiments CDF and D0 have been combined to form the world average for the directly measured value of M_{W} , this is [71]

$$M_{\mathrm{W}} = 80.39 \pm 0.06\mathrm{GeV} \tag{8.1}$$

The top quark mass has been measured at CDF and D0 [4], and together with M_{W} can be used to constrain the allowed mass of the standard model Higgs boson, this is shown figure 8.2.

By the end of 1998, over 150 pb^{-1} of data will have been taken by the OPAL detector at $\sqrt{s}$=189 GeV. Before the end of LEP II it is hoped that approximately 500 pb^{-1} of data will be recorded by each detector. If this is achieved the statistical error on the combined value of M_{W} should be less than 40 MeV for the $\mathrm{q\bar{q}q\bar{q}}$ and $\mathrm{q\bar{q}}l\nu$ channels separately.

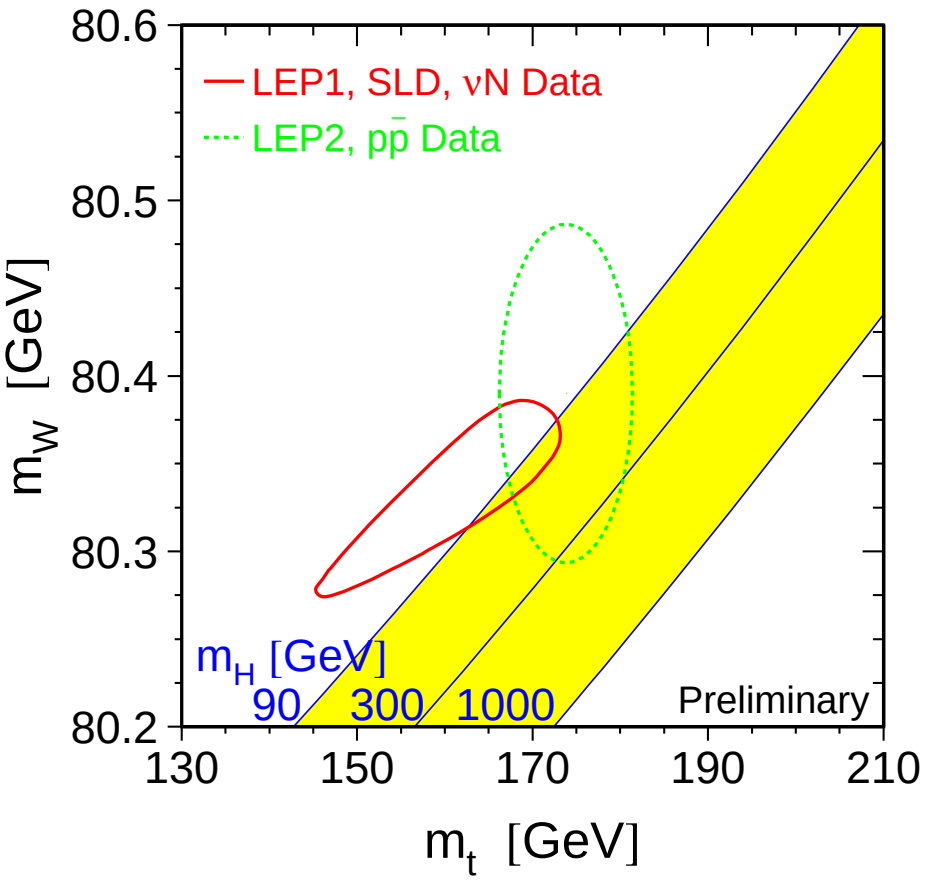

Figure 8.2: The direct measurement of M_{W} and M_{top} are compared to the indirect determinations from LEP I, SLD and Neutrino scattering data. The regions shown correspond to the 68 % confidence limit. The diagonal lines show the Standard Model prediction for various Higgs boson masses. This diagram is taken from [71].

Appendix A

Glossary

A.1 Acronyms

- **1C/2C/4C/5C** The label used for the kinematic fits. It comes from the number of constraint equations minus the number of degrees of freedom. (i.e. the 2C fit used in the $q\overline{q}l\nu$ channel has five constraints and three degrees of freedom).
- **ALEPH** One of the four detectors at LEP.
- **BEC** Bose-Einstein correlations.
- **BW** Breit Wigner function.
- **CDF** A detector at the TEVATRON .
- **CERN** The European laboratory for particle physics.
- **D0** A detector at the TEVATRON .
- **DELPHI** One of the four detectors at LEP.

- **DST** Data Summary Tables
- **ECAL** Electro-magnetic calorimeter in OPAL.
- **EXCALIBUR** A MC event generator.
- **FSR** Final State Radiation.
- **GCE** Energy correction algorithm used to estimate jet energy.
- **GEANT** Detector simulation program.
- **GOPAL** The software used to simulate the OPAL detector.
- **grc4f** A MC event generator, specifically for 4 fermion processes.
- **GROPE** The graphical event display for OPAL events.
- **HCAL** Hadronic calorimeter in OPAL.
- **HERWIG** A MC event generator.
- **JETSET** A MC event generator, generally used by another event generator to do the fragmentation.
- **KORALW** A MC event generator, designed especially for W^+W^-events.
- **L3** One of the four detectors at LEP.
- **LEP** The Large Electron Positron collider at CERN.
- **LEP I** The first stage of LEP, when the beam energy was ~45 GeV and the process $e^+e^- \rightarrow Z^0$ was to measure the properties of the Z boson.
- **LEP II** The second stage of LEP, when the beam energy was increased to over 80 GeV and the process $e^+e^- \rightarrow W^+W^-$became possible.

- **MC** Monte Carlo. A simulation program.
- **MINUIT** A piece of software used to find the minimum of a function.
- **NDF** Number of Degrees of Freedom.
- **OPAL** One of the four detectors at LEP.
- **PDF** Probability Density Function.
- **PS** Proton Synchrotron accelerator at CERN. Also used for the phase space function in the event likelihoods.
- **PTC** Projection-Transformation-Correlation. A technique to transform a set of correlated variables in to an uncorrelated set.
- **PYTHIA** A MC event generator.
- **QCD** Quantum Chromodynamics.
- **QED** Quantum Electrodynamics.
- **R** The resolution function used in the event likelihoods.
- **ROPE** Reconstruction of OPAL Events. The software that combines the sub-detector data to form the DSTs.
- **SLC** The Stanford Linear Collider.
- **SLD** The detector at the SLC.
- $Sp\bar{p}S$ The $p\bar{p}$ collider that was at CERN.
- **SPS** The Super Proton Synchrotron collider at CERN
- **TEVATRON** The $p\bar{p}$ collider at Fermilab.

- **TGC** Triple Gauge Couplings (or Tri-linear Gauge Couplings), the couplings of three gauge bosons.
- **TKMH** Tokyo Multi-hadron selection. A Standard set of cuts used at OPAL to select hadronic events.
- **UA1** One of the two detectors at the $Sp\bar{p}S$.
- **UA2** One of the two detectors at the $Sp\bar{p}S$.
- **UMS** Underlying Mass Spectrum, used in the event likelihoods.
- **WWCOMB** A subroutine in the WW111 software package that assigns the jets to W bosons.
- **WWJECP** A subroutine in the WW111 software package that parameterises the jet 4-momentum errors.
- **WWJEYI** A subroutine in the WW111 software package that parameterises the jet 4-momentum errors, used for the τ jets.
- **WWLPAR** A subroutine in the WW111 software package that parameterises the lepton 4-momentum errors.

A.2 Variables

- C The constant term in the bias parameterisation.
- E_{beam} The beam energy.
- f_b The background pdf.
- f_s The signal pdf.

- f_w The wrong combination pdf.
- Γ_{W} The decay width of the W boson.
- $\mathcal{L}$ The event likelihood.
- $\log \mathcal{L}_{sample}$ The logarithm of the sample likelihood.
- m The mass, usually the average mass per event.
- M^{est} The best estimate of M_{W} from the sample after bias corrections.
- m_f The kinematic fit results, both the mass and the error on the mass.
- $m_W^{\mathcal{L}}$ The mass value that minimises the $\log \mathcal{L}_{sample}$.
- M^{true} The true value of M_{W} in the MC samples.
- m_{W} The postulated value of M_{W} used in the event likelihoods.
- M_{W} The W boson mass.
- p_i The probability that jet pair combination i is the correct one.
- p_s The probability that the event is a signal event.
- S_{eb} The slope of the estimated bias as a function of the beam energy.
- σ^{est} The statistical error on M^{est} .
- $\sigma^{\mathcal{L}}$ The statistical error on $m_W^{\mathcal{L}}$.
- S_{mw} The slope of the estimated bias as a function of M_{W} .
- σ_R The width of the resolution function.

Appendix B

Quality cuts

B.1 Track quality cuts

- $P_T > 0.15$ GeV. Minimum value of momentum transverse to the beam pipe.
- $P < 100$ GeV. Maximum value of momentum.
- Require at least 40 CJ hits or (50 % of the expected number of hits as long as this is greater than 20 hits) which ever is smaller.
- $\mid d_0 \mid < 2.0$ cm. Maximum value of the impact parameter.
- $\mid z_0 \mid < 25.0$ cm. Maximum value of the z coordinate at the point of closest approach.
- $\chi^2_{r\phi} < 100.0$. Maximum value of the χ^2 from the $r\phi$ fit.
- $\chi^2_{sz} < 100.0$. Maximum value of the χ^2 from the sz fit.

B.2 Calorimeter cluster quality cuts

B.2.1 ECAL barrel clusters

- $E_{raw} > 0.1$ GeV. Minimum raw energy of cluster.
- $E_{corr} > 0.0$ GeV. Minimum corrected energy of cluster.
- $N_{block} > 0$. Minimum number of blocks in a cluster.

B.2.2 ECAL endcap clusters

- $E_{raw} > 0.25$ GeV. Minimum raw energy of cluster.
- $E_{corr} > 0.0$ GeV. Minimum corrected energy of cluster.
- $N_{block} > 0$. Minimum number of blocks in a cluster.

B.3 HCAL clusters

- $E_{tower} > 0.6$ GeV. Minimum energy of a tower cluster.

Bibliography

[1] S. L. Glashow, Nucl. Phys. **22** (1961) 579

[2] S. Weinberg, Phys. Rev. Lett. **19** (1967) 1264

[3] A. Salam, in *Prodceedings of the 8th Nobel Symposium*, p. 307, eds. Svartholm, Almqvist, and Wiksell. Stockholm (1968)

[4] S. Abachi *et al.*, The D0 Collaboration, Phys. Rev. Lett. **79** (1997) 1197 f. Abe *et al.*, The CDF Collaboration, Phys. Rev. Lett. **80** (1998) 2767

[5] D. Abbaneo *et al.*. *A Combination of Preliminary Electroweak Measurements and Constraints on the Standard Model.* CERN-PPE-97-154.

[6] LEP ECAL/98-2. *LEP energy calibration above the W pair production threshold.* ICHEP-98/352, July 1998.

[7] LEP Energy Working Group 98/01. *Preliminary LEP energy calibration for 1997 data.* March 1998.

[8] B. R. Martin and G. Shaw. *Particle Physics.* Wiley.

[9] Albajar *et al.*, Z. Phys. **C44** (1989) 15

[10] Ansari *et al.*, Phys. Lett. **B186** (1987) 440

[11] Abachi *et al.*, Phys. Rev. Lett. **77** (1996) 3309

[12] Abe *et al.*Phys. Rev. Lett. **75** (1995) 11

[13] OPAL Conference report. *W physics in* e^+e^- *collisions at* $\sqrt{s}$*=161 and 172 GeV at LEP.* CR349. T. Saeki, September 1997. 12th Int. Workshop HEP and QFT, Samara, Russia.

[14] *Review of particle Physics.* Physical Review D, Particles and Fields, Part 1, July 1996.

[15] *Review of particle Physics.* Eur. Phys. J. **C3** (1998) 1

[16] F. Halzen and A. D. Martin. *Quarks and Leptons: An Introductory Course in Modern Particle Physics.* Wiley.

[17] F. Mandl and G. Shaw. *Quantum Field Theory.* Wiley.

[18] I. J. R. Aitchison and A. J. G. Hey. *Gauge Theories in Particle Physics.* Hilger.

[19] *Physics at LEP II.* Editors: G. Altarelli, T. Sjostrand and F. Zwirner. Vol. 1 pg. 77

[20] D. Bardin, J. Biebel, D. Lehner, A. Leike, A. Olchevski and T. Riemann. *GENTLE, A program for the Semi-Analytic Calculation of Predictions for the Process* $e^+e^- \rightarrow$ *4 fermions.* hep-ph/9612409, December 1996.

[21] S.Bauberger and G. Weiglein, Phys. Lett. **B419** (1998) 333.

[22] V. S. Fadin, V. A. Khoze, A. D. Martin, and A. Chapovsky. *Coulomb effects in* W^+W^-*production.* DTP/94/116. December 1994.

[23] OPAL Physics Note. W^+W^-*Event Properties at roots=183 GeV.* PN365. M. Watson and N. Watson. July 1998.

[24] W. A. Zajc in *Hadronic Multiparticle Production*, (Ed. P. Carruthers), World Scientific, 1998, p. 235

E. A. De Wolf. *Bose-Einstein Correlations*, Proc. XXVII Int. Conf. on High Energy Physics, Glasgow 20-27 July 1994 (Eds. P. J. Bussey and I. G. Knowles), Inst. of Physics Publ., 1995, p. 1281.

[25] OPAL Collab., G. Alexander *et al.*, Z. Phys. **C72** (1996) 389

[26] L. Lonnblad and T. Sjostrand. *Modelling Bose-Einstein Correlations at LEP2.* HEP-PH/9711460 (1997)

[27] K. Fialkowski and R. Wit *Implementation of Bose-Einstein interference effects in Monte Carlo generators.* Eur. Phys. J. **C2** (1998) 691

[28] OPAL Physics note. *Bose-Einstein Correlations in Hadronic Decays of W Pairs produced in* e^+e^- *Reactions at* $\sqrt{s}$ *of 172 and 183 GeV.* PN330, February 1998.

[29] *Bose-Einstein correlations in W-pair decays*, ALEPH 98-065, July 1998.

[30] *The Study of Bose-Einstein Correlations Using Hadronic W Decay at 183 GeV*, L3 Note 2268, June 1998.

[31] S. L. Lloyd. *The OPAL Primer.* version 97b, July 1997. (ftp from /afs/cern.ch/opal/www/manuals/oprimer.ps)

[32] OPAL Collaboration. *The OPAL Detector at LEP.* K.Ahmet *et al.*, Nucl. Instr. and Meth. A 305 (1991) 275.

[33] OPAL Conference report. *The OPAL Silicon Microvertex Detector with Two Coordinate Readout.* Alan Honma, CR131, September 1993.

[34] OPAL Technical Note. *Thin Scintillating Tiles with High Light Yield for the OPAL Endcaps.* TN524, TE Group, November 1997.

[35] C. Hawkes, D. Lellouch, M. Redmond, O. Schaile and M. Schroder. *The ROPE users guide.* ROPE410, February 1996. (ftp from /afs/cern.ch/opal/www/manuals/ro/pro/ro410.ps)

[36] D. Ward and J. Banks *A GRope Primer.* GR202, March 1995. (ftp from /afs/cern.ch/opal/www/manuals/gr/pro/gr202.ps)

[37] S. Catani *et al.*, Phys. Lett. B269 (1991) 423

[38] Program KORALW V1.33, M. Skrzypek *et al.*, Comput. Phys. Commun. **94** (1996) 216;
M. Skrzypek *et al.*, Phys. Lett. **B372** (1996) 289.

[39] T. Sjöstrand, CERN-TH.7112/93

[40] T. Sjöstrand, Comput. Phys. Commun. **82** (1994) 74.

[41] T. Sjöstrand, Nucl. Phys. **B248** (1984) 469

[42] Program GRC4F V2.0 and V2.2, J. Fujimoto *et al.*, Comput. Phys. Commun. **100** (1997) 128.

[43] Program EXCALIBUR, F.A. Berends, R. Pittau and R. Kleiss, Comput. Phys. Commun. **85** (1995) 437.

[44] Program HERWIG, G. Marchesini *et al.*, Comput. Phys. Commun. **67** (1992) 465.

[45] J. Allison *et al.*, Phys. Rev. **A317** (1992) 47

[46] R. Brun *et al.*, *GEANT Users Guide (Version 3)*, CERN EE EE 84/1, (1987). (Available at http://consult.cern.ch/writeup/geant)

[47] OPAL WW111 software manual. Coordinators C.P Ward, D.R. Ward and N. Watson. (ftp from /afs/cern.ch/opal/www/manuals/ww/dev/ww111.ps)

[48] *Measurement of the W Boson Mass and* W^+W^- *Production and Decay Properties in* e^+e^- *Collisions at* $\sqrt{s}$*=172 GeV.* CERN-PPE/97-116, Eur. Phys. J. **C1** (1998) 395

[49] OPAL Technical Note. *Likelihood selections for* $W^+W^- \rightarrow q\overline{q}q\overline{q}$ *Events at 171 GeV.* TN 443, C. Burgard, D. Eatough, C. Hartmann and T. Shears, December 1996.

[50] see file */u/ws/opalmw/car/event2_01.car* on SHIFT6. Author S. Bentvelsen.

[51] O. Nachtmann and A. Reiter, Z. Phys. **C16** (1982) 45;
M. Bengtsson, Z. Phys. **C42** (1989) 75.

[52] OPAL Technical Note. *Approximation of Probability Distributions by their Projections and Correlations.* TN483, D. Karlen, May 1997.

[53] OPAL Technical Note. *An Improved Likelihood Selection Technique for Correlated Variables.* TN459, D. Karlen, February 1997.

[54] OPAL Technical Note. *Measurement of* M_W *in* $W^+W^- \rightarrow q\overline{q}q\overline{q}$ *Events.* TN298, D. Ward, May 1995.

[55] OPAL Technical Note. *A 1-C Kinematic Fit for* $W^+W^- \rightarrow q\overline{q}\tau\nu$ *Events*, TN534, R.L. Coxe and D.A. Glenzinski, February 1998.

[56] D. Ward's OPAL work web page. (http://opalinfo.cern.ch/opal/group /ww/WmassWorkPage/drw/jetsyst183.txt. E-mail DRW1@hep.phy.cam.ac.uk)

[57] D. Glenzinski's OPAL work web page. (http://opalinfo.cern.ch/opal /group/ww/WmassWorkPage/douglasg/scratch.html.
E-mail douglasg@hpopb1.cern.ch)

[58] Frodesen, Skjeggestad, Tofte. *Probability and Statistics in Particle Physics.* Universitetsforlaget.

[59] The OPAL Collaboration. *W mass and width in* e^+e^- *collisions at 183 GeV.* submitted to Eur. Phys. J. **C** (1998) .

Available at http://opalinfo.cern.ch/opal/group/ww/welcome.html. E-mail Mark.Thomson@cern.ch

[60] OPAL Technical Note. *Measurement of the Mass and the Width of the W Boson Using a Reweighting Method.* TN468, C. Burgard, C. Hartmann, March 1997.

[61] *Physics at LEP II.* Editors: G. Altarelli, T. Sjostrand and F. Zwirner. Vol. 1 pg. 525

[62] *MINUIT - a system for function minimization and analysis of the parameter errors and corrections.* CERN-DD-75-20, F. James and M. Roos, Comput. Phys. Commun. (1975) pg 38.

[63] OPAL Technical note. *GCE++ An Algorithm for Event Energy Measurement.* TN306, E. Duchovni, D. Lellouch G. Mikenberg, T. Wlodek, June 95.

[64] P. Hall. *The bootstrap and Edgeworth expansion.* New York, Springer-Verlag, 1992.

[65] Z. Phys. **C69** (1996) 543

[66] OPAL Physics Note. *Measurement of the W-pair production cross section and triple gauge boson couplings at LEP.* PN 354, The W-pair and TGC working groups, July 1998.

[67] Roger Barlow. *Evaluating Systematic Errors.* MAN/HEP/93/9.

[68] OPAL Physics Note. *Measurement of the W Boson Mass and the* W^+W^- *Production Cross Section in* e^+e^- *Collisions at 183 GeV.* PN331, The WW Working Group, March 1998.

[69] OPAL Technical Note. *Measurement of the Mass of the W Boson at 183GeV using an analytic Breit-Wigner fit.* TN564, C.P.Ward and D.R.Ward, September 1998.

[70] OPAL Technical Note. *Measurement of the W boson mass using a convolution method.* TN560, D. Eatough, August 1998.

[71] OPAL Conference report. *Measurement of the W-Boson Mass at LEP.* CR372, M.A. Thomson, July 1998, ICHEP'98, Vancouver.

[72] N. K. Watson. W^+W^- *Hadronic Decay Properties.* to be published in proceedings of ICHEP98